On the Signatures of Magnetopause Shadowing Losses in the Van Allen Radiation Belts of the Earth

by

Leonid Olifer

A thesis submitted in partial fulfillment of the requirements for the degree of

Master of Science

Department of Physics

University of Alberta

Abstract

After the discovery of the Van Allen radiation belts over 60 years ago, the processes responsible for the transport, loss, and energization of the relativistic electrons in the belts have been one of the most actively researched topics in the space physics community. Current understanding is that the trapped electrons can be either lost to the atmosphere because of the interaction with high-frequency plasma waves such as whistler mode chorus, plasmaspheric hiss, or electromagnetic ion cyclotron waves, or they can be transported outward to the magnetopause and lost to the magnetosheath because of their interaction with ultra-low frequency (ULF) waves. However, both of these approaches fail to explain the observations of extremely fast radiation belt losses with timescales of $\sim 0.5 - 2$ hours. This thesis is focused on the analysis of such extremely fast radiation belt extinction events. Specifically, we try to determine if the outer radiation belt response and the magnetosphere dynamics fit within the outward ULF wave radial diffusion paradigm.

Firstly, we analyze Pc4-Pc5 ULF wave dynamics in the electromagnetic field of the Earth during the intense geomagnetic storm on March 17-18, 2015. This storm is a classic example of a radiation belt extinction event, during which the population of ultra-relativistic electrons was lost within 2 hours after the storm commencement. Analysis of measurements of the electromagnetic field from GOES and THEMIS satellites and ground-based magnetometers shows that the main phase storm-specific ULF waves do not correspond to statistical estimates. Notably, the radial diffusion rates produced by the

electric field are reduced, compared to empirical models based on Kp. Meanwhile, the magnetic diffusion rates are increased. Our results show that the main phase magnetic radial diffusion cannot be neglected, contrary to prior results. Therefore, to accurately represent the diffusion rates during such fast loss events, and which we further show are associated with periods characterized by a strong southward component of the interplanetary magnetic field, modifications of the statistical Kp-dependent models for the ULF wave radial diffusion coefficients are required.

Secondly, we use electron flux data from the constellation of Global Positioning System (GPS) satellites to resolve the fast timescale characteristics of the radiation belt response during radiation belt extinction events. We investigate four storms that happened between 2012 and 2015 with different loss and recovery patterns. We compare the dynamics of the outer radiation belt with the last closed drift shell (LCDS), computed using the *Tsyganenko and Sitnov* (2005) magnetic field model, and the results show a very strong correspondence between the two. Significantly, the location of the LCDS closely mirrors the high time resolution losses observed in GPS flux. We conclude that expressing the location of the LCDS in L* space and using the electron flux observations from the GPS satellites are crucial when addressing the rapid relativistic electron flux loss associated with magnetopause shadowing.

Finally, we perform a statistical analysis of the trapped electron radiation during magnetopause shadowing events. We use a superposed epoch analysis of ultra-relativistic electron flux data and additionally compute phase space density from the Van Allen Probes to analyze 64 magnetopause shadowing events from 2012 until 2018. Our analysis confirmed that magnetopause shadowing losses can occur on the timescales of $\leq$6 hours, and can also penetrate deep into the heart of the radiation belt. Moreover, the strong self-similarity of the loss patterns between different storms and across different energies con-

firms that the governing factor controlling the loss is the outward transport of the electrons to the compressed magnetopause. Additionally, we show that in the recovery phase of these storms there is an apparent energy dependence of the replenishment of the belt with lower energies recovering faster.

Overall, we confirm that magnetopause shadowing consistent with outward particle transport due to the ULF wave radial diffusion is most likely the cause of radiation belt depletion during many storm events especially those associated with the inward motion of the magnetopause and the LCDS. Our results show that during the main phase of a magnetic storm the radiation belt displays all the signatures of such losses. However, to accurately reproduce the very fast losses associated with radiation belt extinction events, some changes to the current empirical models for the radial diffusion coefficients, usually expressed in the form of Kp-parametrization, should be made.

Preface

This thesis is an original work by Leonid Olifer. Chapter 3 was submitted to the Journal of Geophysical Research: Space Physics as Olifer, L., I. R. Mann, L. G. Ozeke, I. J. Rae, and S. K. Morley (2018), *On the relative strength of electric and magnetic ULF wave radial diffusion during the March 2015 geomagnetic storm* and is currently under review. Chapter 4 was published as Olifer, L., I. R. Mann, S. K. Morley, L. G. Ozeke, and D. Choi (2018), *On the role of last closed drift shell dynamics in driving fast losses and Van Allen radiation belt extinction*, Journal of Geophysical Research: Space Physics, doi:10.1029/2018JA025190. In both publications, I was responsible for the data analysis and the manuscript composition. I. R. Mann was the supervisor for both of these projects, as well as for the whole research, presented in this thesis. L. G. Ozeke, S. K. Morley, and I. J. Rae contributed as the coauthors by providing constructive feedback on the results of my research and the journal manuscript composition.

Acknowledgements

I want to thank my supervisor, Prof. Ian R. Mann, who gave me a chance to prove myself in the space physics field and provided professional guidance through this research. I am also thankful to my supervisory committee, Richard Sydora, Joseph Maciejko, and Richard Marchand, for their feedback and constructive questions on my research and this thesis.

I would also like to thank Louis G. Ozeke and Steve K. Morley for their help and collaboration during the research which led to the creation of this thesis. Also, many thanks to my friends, family, and loved ones for their support and love which helped me greatly when being far away from home.

Special thanks to V. Choliy, G. Lizunov, A. Parnowski, and other researches at the laboratory for satellite near space exploration in Kyiv Space Research Institute for showing me that the physics research can be fun and bring people together.

Table of Contents

List of Tables

List of Figures

Chapter 1

Introduction

1.1 Sun-Earth Coupling

The interplanetary space from the surface of the Sun to the edge of the heliosphere is filled with the ionised gases that consist of electrons, protons, or ions. In general, such systems of charged particles, which on a large scale is neutral, is called *plasma*. Plasmas are also found in stellar atmospheres, interplanetary and interstellar media, planetary magnetospheres, ionospheres, and nebulas (e.g., *Russell*, 1995; *Cravens*, 2004). Dynamics of these large systems of charged particles inside the solar system and their effects on human activities and other extraterrestrial bodies are usually referred to collectively as *space weather*. A short description and overview of the major space weather phenomena inside the solar system, their effects on the Earth and its magnetosphere are provided in this chapter.

1.1.1 The Sun

The sun is a G-type main-sequence star (G2V) and, as discussed later in this chapter, is the primary source of plasma in the solar system. The interior of the sun consists of the *core* in the center followed by the *radiative* and *convective* zones. The core spreads across ∼0.25 sun radii and is the hottest and the densest region of the sun, sufficient for nuclear fusion to occur. The radiative zone spreads between 0.25 and 0.75 sun radii. It is an opaque environment which traps the radiation, coming from the core of the sun, by making it undergo many deflections. According to the theoretical estimates, it takes almost

10 million years for the radiation to travel from the core to the surface on the sun due to many scattering processes (*Priest*, 1995). The final interior layer, convective zone, spreads from 0.75 to 1 sun radii. In this region, the temperature starts to decrease with radius dramatically. It causes the convection to occur, transferring the heat outward.

The atmosphere of the sun consists of three layers. The inner layer is called the *photosphere*. It is only 500 km thick, has a density of $\sim 10^{23}$ m^{-3}, and emits most of the light. The middle layer is called *chromosphere* with the density of $\sim 10^{17}$ m^{-3}. It spreads for 2.5 Mm ($\sim 3.6 \cdot 10^{-3}$ Sun radii) and is followed by the outer layer of solar *corona* that extends from the surface of the star to the interplanetary space (*Priest*, 1995; *Golub*, 2010). The temperature of the photosphere is 4200 K and is the lowest throughout the sun. However, it slowly increases with altitude to the values of $\sim$5800 K in the chromosphere and suddenly increases to $\sim 10^6$ K in the corona. Moreover, this rapid increase was found to occur over a very short distance of $\lesssim$500 km, called *transition region*. There is a number of processes that are most likely responsible for the coronal heating. The majority of them involve the solar magnetic field and particle interactions with it (*Golub*, 2010).

The magnetic field of the sun is generated by the motion of particles inside the star. In general, the magnetic field lines of the sun extend from one of the hemispheres into the outer space with other field lines returning to another hemisphere of sun. These types of the field lines are usually referred to as *open* field lines because they extend far beyond the planetary system, eventually connecting on the edges of the heliosphere. On the other hand, the *closed* field lines remain entirely attached to the solar corona and form loops and active regions much closer to the surface of the sun. They concentrate at lower latitudes, close to the equatorial plane of the sun (*Priest*, 1995). Some of the open field lines form on the edges of the closed field lines region. They extend to the interplanetary surface along the magnetic equatorial plane of the sun creating the heliospheric current sheet. However, such extension of the field lines is caused by the outflowing plasma from the solar corona, called the *solar wind*, which is described in the next section.

1.1.2 Solar Wind

Parker (1958) proposed the first theoretical model of the solar wind as a rapidly expanding solar corona. At a certain distance from the center of the Sun, particles stop being gravitationally trapped because their kinetic energy of thermal motion overcomes the gravitational potential energy. This creates a constant outflow of the solar plasma and expansion of solar atmosphere into the interplanetary medium. The chemical composition of the solar wind is similar to the upper layers of the Sun. It mainly consists of electrons, protons, and has a small portion of He^{2+} or heavier ions. On the far enough distance from the sun, the solar wind speed, $v(r)$, can be calculated using equation (1.1), derived from the *Parker* (1958) model.

$$v(r) \approx 2 \left(\frac{2kT}{m} \right)^{1/2} \left(\ln \frac{4kTr}{GM_{\odot}m} \right)^{1/2}, \tag{1.1}$$

where r is the distance from the sun, k is the Boltzmann constant, T is the temperature, m is the mass of the particle, G is the universal gravitational constant, and $M_{\odot}$ is the mass of the sun. Depending on the temperature of the solar corona, the solar wind speed in near-Earth space can be on the order of 200-1000 km/sec, according to *Parker* (1958) model.

However, another important thing to note is that the sun has its magnetic field. Moreover, the characteristics of the magnetic field are different on different latitudes, as was described in the previous section. Particles originating in the regions with the open field lines can easily escape the sun's surface, and the plasma that follows the open magnetic field lines is usually referred to as the *fast* solar wind. Its speed is ∼700 km/sec. Meanwhile, the solar wind that can escape the regions of closed magnetic field lines, in the low latitude regions of the sun, is called the *slow* solar wind with its speed of ∼400 km/sec (see e.g., review by *McComas et al.*, 2002). Later observations of the solar wind showed that besides a constant fast and slow plasma outflow massive coronal mass ejections (CMEs) are present in the solar wind (*Russell*, 1995; *Priest*, 1995; *Hundhausen*, 1972).

Another thing to note is that the solar wind carries the magnetic field with

it. Usually, this field is referred to as a *frozen-in* magnetic field, that originated in the sun and then being "transported" and deformed by the plasma outflow. The frozen-in concept comes from the magnetohydrodynamic and, skipping the derivation, shows that the flux of the magnetic field taken across a particular boundary bounded to the plasma, stays constant, i.e., the plasma and the given boundary may move, deform, expand, or shrink, but the magnetic flux across the same boundary will be the same (*Kivelson*, 1995). As the result, that the plasma can "transport" the magnetic field from one point of space to another one. For the sun and the solar system, this type of the magnetic field that is being carried with the solar wind is called the *interplanetary magnetic field* (IMF).

Moreover, because of the resistance of the IMF, the solar wind interacts with both magnetized and unmagnetized bodies in the Solar system, and these interactions are different (e.g., *Walker and Russel*, 1995; *Luhmann*, 1995). Interaction with the former (*e.g.* Earth) is much more complex than with the latter. Interaction with the magnetized bodies creates a bow-shock which separates solar wind and planetary plasma, as well as the magnetopause, separating solar and planetary magnetic fields. On the other hand, only a bow-shock is present for the unmagnetized solar system bodies. The next section presents a more detailed description of the interaction between the solar wind and a magnetized body of the solar system using the example of the Earth.

1.1.3 Earth's Magnetosphere

The Earth has a dipole-like magnetic field with the magnetic dipole being misaligned with the rotational axes of the Earth by $\sim$11.3° (*Russell*, 1995). Currently, the most appropriate description of mechanisms which generate the planetary magnetic field is provided by the *dynamo theory* (*Akasofu and Chapman*, 1973). The model assumes a self-sustaining process through which liquid metal in the planetary core can sustain the magnetic field for a long time. This model was validated by numerical simulations (e.g., *Glatzmaier and Roberts*, 1995; *Kuang and Bloxham*, 1997). The resulting dipole magnetic field of the Earth has the magnetic moment with the magnitude of $8.07 \cdot 10^{22}$ Am^2.

Note that the dipole tilt angle and the magnitude of the magnetic moment slowly change in time and is usually described by numerical models (e.g., *Thébault et al.*, 2015).

However, due to the interaction with the solar wind and IMF, the magnetic field of the Earth changes its structure, resembling dipole only near the Earth surface and being massively distorted by the external field further away. Similarly to regular fluid dynamics, the shock wave forms in front of the Earth at a distance of 10-13 Earth radii, R_E, when supersonic solar wind meets an obstacle. This shock wave is called the *bow-shock* (*Luhmann*, 1995; *Hughes*, 1995). After the bow-shock, the solar wind slows down and compresses, increasing its density, but still carries the IMF with it. Another boundary called *magnetopause* is formed 3-4 R_E after the bow-shock. It separates the planetary magnetic field and the IMF. Due to the interaction between the magnetosphere of the Earth and the IMF through the process of *magnetic field line reconnection*, the dayside of the magnetosphere compresses and the night side elongates (*Hughes*, 1995). It creates a bullet-shaped cavity in the solar wind flow, where Earth with its magnetic field exists.

Figure 1.1 shows a schematic representation of the magnetic field around the Earth and position of the bow-shock and the magnetopause. Curved lines with arrows represent the magnetic field lines which are formed after the interaction of the Earth's dipole field and the IMF. Figure 1.1 also shows the dipole field lines with dotted curves. Comparing the two magnetic field structures, it is obvious that the real magnetic field resembles the dipole close to the surface of the Earth, especially on the dayside. However, starting from $\sim$3 R_E the dipole field is deformed entirely by the solar wind and there are significant differences between the two magnetic field models. Because the solar wind and IMF cause this deformation, the structure of the outer magnetosphere depends on the characteristics of the IMF and the level of the sun-terrestrial coupling.

Dungey (1961) proposed the description of the processes happening in the magnetic field of the Earth when it interacts with the IMF. The particularly interesting case is the dayside interaction of the southward IMF with the north-

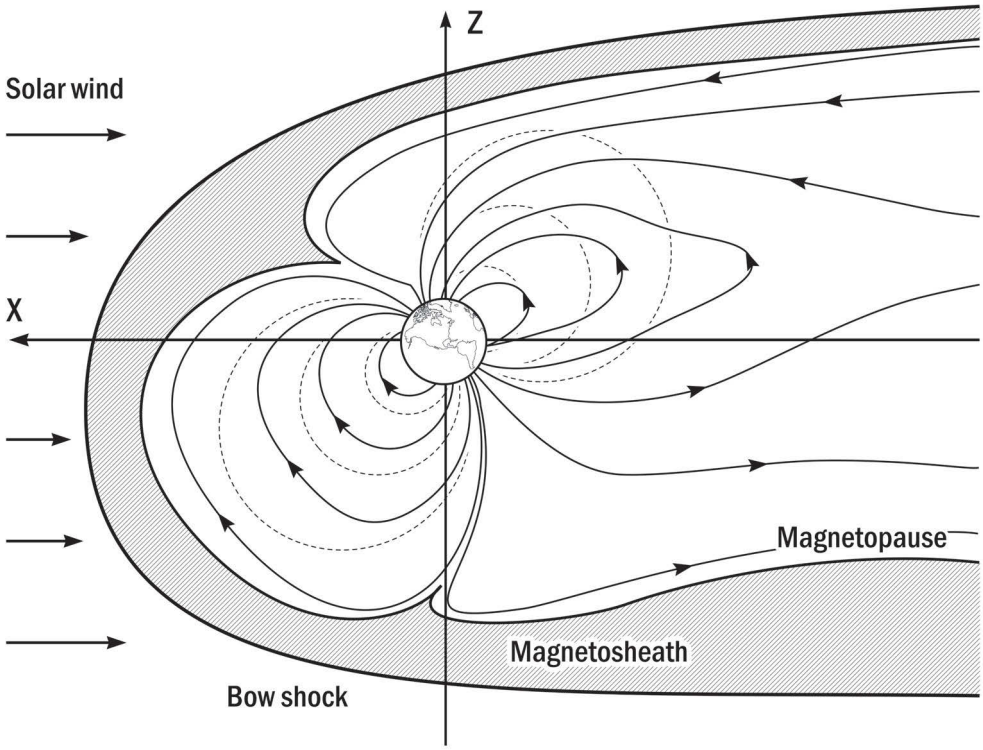

Figure 1.1: Schematical representation of the magnetic field lines of the Earth. Solid curved lines represent the magnetic field lines of the Earth with arrows showing the direction of the magnetic field. Dotted lines around the Earth represent the field lines of the magnetic dipole for comparison with the more realistic representation. The Figure also labels different boundaries. See text for more details. Image credit: Andy Kale

ward magnetic field of the Earth. During these conditions, a process called *dayside reconnection* happens between the magnetic field of the Earth and the one brought by the solar wind. As a result, magnetic field lines on the day side of the magnetosphere reconnect and are no longer closed, but connect to the IMF instead. It creates open field lines of the Earth, which eventually connect and form a loop much further than the Earth scale, possibly even in the sun. Then, these open field lines are transported by the solar wind nightward, according to the frozen-in flux condition, where they enter the magnetotail. Further downstream, the *nightside reconnection* happens between the two open field lines from the southern and northern lobes of the magnetosphere, forming a single closed field line and slowly returning to the day side through the dusk

or dawn side of the Earth. This process was called the *Dungey cycle* and is vital for understanding the temporal dynamics of the magnetosphere.

The magnetosphere of the Earth also contains populations of charged particles, plasma, which are trapped inside the Earth's magnetic field. These particles originate from the sun, brought by the solar wind, and from the ionosphere of the Earth forming different types of trapped particle population. Depending on the origin of plasma, different regions have different ion composition with the vast majority being electrons and protons. However, heavier ions like H^+, He^+, O^+, and so forth, are being present as well. The most populated regions are the *plasmasphere*, the *ring current*, and the *Van Allen radiation belts*. The plasmasphere is a torus-shaped region within 2-3 R_E from the center of the Earth. It contains mostly cold, low energetic ($\lesssim 1$ eV) particles that drift upwards from the ionosphere and corotate with the Earth. This population is mostly stable due to its proximity to the Earth's surface. However, during times of high geomagnetic activity, the outer plasmasphere boundary, the *plasmapause*, gets closer to the Earth. The ring current occupies the region of the magnetosphere from ~ 2 R_E, overlapping with the plasmasphere, to ~ 5 R_E, extending further to the inner portion of the magnetosphere. The majority of particles in the ring current are protons and electrons with energies from tens to hundreds keV. As will be explained in Chapter 2, the electrons and protons drift around the Earth in opposite directions, creating a steady current. The major source of particles in the ring current is the solar wind. The Van Allen radiation belts are formed by the high energetic, MeV, electrons and protons. They typically extend from 2 to 7 R_E and are shaped as two belts surrounding the Earth. The Van Allen radiation belts population is unstable due to its proximity to the outer edges of the magnetosphere, which strongly depends on solar-terrestrial coupling. The focus of this thesis is particularly the dynamics of the outer Van Allen belt during the storm times. The characteristics of the radiation belts are given in the next section of this chapter.

1.1.4 Van Allen Radiation Belts

Discovered in early 1958, the *Van Allen radiation belts* comprise highly energetic charged particles which are trapped in the Earth's magnetosphere (*Van Allen and Frank*, 1959). They form two regions – *inner* and *outer* belts. The inner belt is located around 1.5-2 R_E from the center of the Earth and consists of low energy electrons (<0.05 MeV), protons (with energies ∼1-10 MeV and more), and heavier ions like helium or oxygen (*Walt*, 1994). Due to its proximity to the Earth surface, the magnetic field is mostly dipolar. Therefore, the inner belt population of particles is relatively stable. However, an intense storm can still penetrate to those regions (e.g., *Baker et al.*, 2004).

The outer belt spreads between 3 and 7 R_E and consists mostly of relativistic electrons with energies >0.5 MeV (*Walt*, 1994). The magnetosphere in that region is highly dynamic due to the interaction with the solar wind. Therefore, predicting the dynamics of the outer radiation belt is complicated, especially during geomagnetic storms. Figure 1.2 shows diagrams of the charged particle populations in the inner and outer belts as provided by an empirical, epoch-independent NASA AP8/AE8 model (*Sawyer and Vette*, 1976; *Vette*, 1991). Note that the AP8/AE8 model gives only a baseline representation of the fluxes present in the radiation belts. Meanwhile, this model does not represent storm time disturbances, because it is not dependent on solar wind conditions which can significantly change the populations of trapped particles (e.g., *Spence et al.*, 2016).

1.2 Thesis Motivation and Outline

As described later in this thesis, the existing models of the Van Allen belt dynamics mostly assume that typical times of the radiation belt losses span from days to several weeks. However, current observations of the trapped radiation by the Van Allen Probes mission showed multiple storms with much more rapid losses, happening on time scales of several hours. Two of the most prominent examples of these losses are geomagnetic storms which happened on March 17, 2013, and on March 17, 2015. During these storms, the population

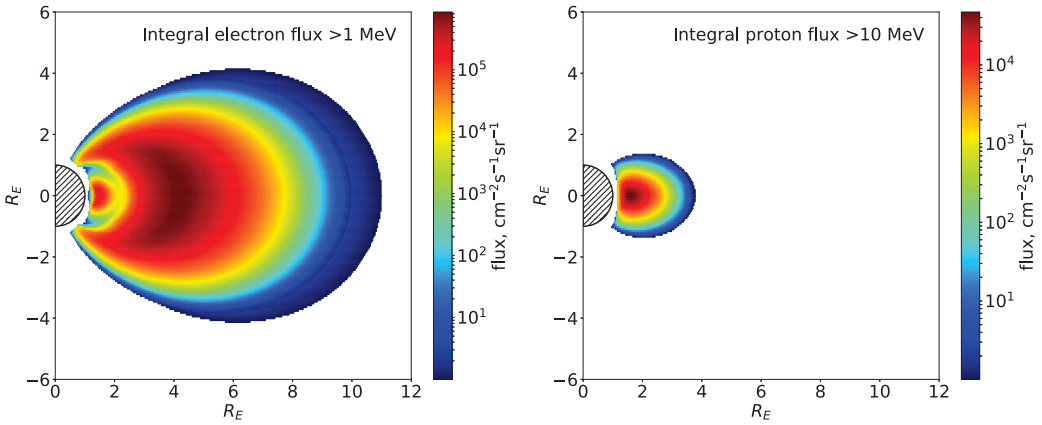

Figure 1.2: Integral, omnidirectional electron (left panel) and proton (right panel) fluxes as provided by NASA AP8/AE8 model (*Sawyer and Vette*, 1976; *Vette*, 1991). Note, that the cavity (slot) between inner and outer belts is present for electron >1 MeV population and this population is larger in the outer belt. Meanwhile, the majority of protons with energies >40 MeV mostly concentrate in the inner belt.

of relativistic MeV electrons was depleted entirely in a matter of hours between two subsequent passes of the Van Allen Probes. Such fast events were named radiation belt extinction events by *Ozeke et al.* (2017). Determining the actual processes that led to these fast losses is still a hot topic in space physics field.

During geomagnetic storms, the state of the magnetosphere changes dramatically and the populations of trapped particles usually suffer dramatic changes as well (e.g., *Spence et al.*, 2016). The response of the radiation belts has been studied for a long time ever since their discovery. Processes of electron acceleration up to MeV energies during geomagnetic storms have been studied in great detail (e.g., *Albert*, 2005; *Horne et al.*, 2005; *Omura et al.*, 2007; *Shprits et al.*, 2008; *Thorne et al.*, 2013, to list a few) but many important questions remain. The processes which can cause Van Allen radiation belt losses are in particular still hotly debated. According to the current theories, trapped particles can be lost downward to the atmosphere of the Earth, or outward across the magnetopause to the magnetosheath through a process called *magnetopause shadowing*. The atmospheric loss usually involves interactions with high frequency waves and scattering into the loss cone. Examples of waves which cause such an atmospheric loss are electromagnetic ion cy-

clotron (EMIC) waves (e.g., *Kersten et al.*, 2014; *Kang et al.*, 2016; *Shprits et al.*, 2016), plasmaspheric hiss (e.g. *Thorne et al.*, 1973; *Lee et al.*, 2013), or chorus waves (e.g., *Shprits et al.*, 2007; *Li et al.*, 2014). Meanwhile, outward losses through the magnetopause can be enhanced by outward diffusion due to interactions with ultralow frequency (ULF) waves (e.g., *Shprits et al.*, 2006; *Loto'aniu et al.*, 2010; *Mann and Ozeke*, 2016; *Mann et al.*, 2016). A self-sustaining balance between loss, restoration, and energization processes exists in the Van Allen belts (*Friedel et al.*, 2002; *Reeves et al.*, 2003).

This thesis focuses on the investigation of such extremely fast events. Chapter 2 provides the mathematical basis for the analysis of processes related to charged particle motion in the radiation belts and their response to solar wind forcing. Chapters 3 focuses on the analysis of the radial diffusion coefficients during the March 2015 geomagnetic storm. We analyze the in-situ measurements from different satellites and ground-based magnetometers to compare the event-specific radial diffusion coefficients to statistical estimates (e.g., *Ozeke et al.*, 2014). In Chapter 4 we analyze the potential impact of the dynamics of the outer boundary on the outward radial diffusion of trapped electron populations. The analysis is performed for three intense March 2013, September 2014, and March 2015 storms as well as for a moderate September 2012 storm. The March 2013 and March 2015 storms show fast extinction and almost immediate recovery. Meanwhile, the September 2014 storm shows fast extinction but no recovery for around two weeks. By contrast, the moderate September 2012 storm which generated a three radiation belt morphology (e.g., *Mann et al.*, 2016) shows a more gradual loss. Investigations, made in Chapter 4, are generalized in Chapter 5, where we perform a superposed epoch analysis of intense magnetopause shadowing events. We show, for the first time, that losses associated with inward magnetopause motion can be seen to progress inwards as expected from outward radial diffusion. Moreover, we show that the magnetopause shadowing events have signatures of energy dependence during the recovery phase of a geomagnetic storm.

Chapter 2

Motion of Charged Particles in the Earth's Magnetosphere

This chapter focuses on a mathematical description of the charged particle dynamics in the Earth's magnetosphere. The first part of the chapter focuses on a *single particle motion* of a charged particle in an electromagnetic field. It provides the necessary background to the dynamics of charged particles in the Van Allen belts. This part also focuses on the derivation of the adiabatic invariants, which are important when assessing storm-time dynamics of the belts. The second part generalizes the single particle motion and provides a simplified model of the radiation belts by describing the dynamics of systems of the particles using diffusion equations. This approach has been used by multiple authors in simulations of the radiation belts and helps to overcome numerical challenges associated with tracing trajectories of very large numbers of particles to determine the resulting state of the radiation belts during storms.

2.1 Single Particle motion

The most general equation of motion of a single charged particle is given by equation 2.1.

$$\frac{d\mathbf{p}}{dt} = q\frac{d\mathbf{r}}{dt} \times \mathbf{B}\left(\mathbf{r}, t\right) + q\mathbf{E}\left(\mathbf{r}, t\right) + m_0\mathbf{g}\left(\mathbf{r}, t\right), \tag{2.1}$$

where $\mathbf{p}$ is the momentum of the particle, $\mathbf{r}$ position of the particle, q charge of the particle, m_0 rest mass of the particle, $\mathbf{B}(\mathbf{r}, t)$ is the magnetic field which generally has spatial and time dependence, $\mathbf{E}(\mathbf{r}, t)$ is the electric field, and $\mathbf{g}(\mathbf{r}, t)$ is the gravitational field. Solving this equation to find the trajectory of a particle can be done, but this can become challenging to study the dynamics of an ensemble of many charged particles. As was mentioned before, this work focuses on the dynamics of charged particles in near-Earth space, when they are trapped inside the magnetic field of the Earth. Therefore, for simplification in this chapter the assumption of a pure dipole magnetic field is used. In this section we also assume $\mathbf{E} = 0$, $\mathbf{g} = 0$, and the magnetic field $\mathbf{B}$ is given by the system of equations (2.2).

$$\begin{aligned} B_x &= 3xzM_z r^{-5}, \\ B_y &= 3yzM_z r^{-5}, \\ B_z &= \left(3z^2 - r^2\right) M_z r^{-5}, \end{aligned} \tag{2.2}$$

where $(x,\ y,\ z)$ are general Cartesian coordinates, $r = \sqrt{x^2 + y^2 + z^2}$ is the radius vector, and M_z is the magnetic moment of the dipole which is aligned with the z-axis. For Earth $M_z = 8.07 \cdot 10^{22}$ Am^2. Equation 2.1 with these assumptions can be easily solved numerically, and the results were reported in multiple studies (e.g., *Northrop*, 1963; *Roederer*, 1970; *Walt*, 1994, to list a few). When in the dipole field a single charged particle experiences three types of periodic motion: *gyration*, *bouncing*, and *drift*. Schematically these types of periodic motion are shown in figure 2.1. Gyration is the rotation of a particle around a field line which is caused by the Lorentz force. Bouncing and drift types of motion appear in inhomogeneous magnetic fields. Particles trapped in the dipole magnetic field and in the absence of other perturbations will stay there forever. These particles form the inner and outer radiation belts around the Earth. The subsections which follow analyze the properties of each type of periodic motion in more detail.

Usually, it is easier to describe the particle dynamics in a magnetic field using a field-aligned coordinate system. In this system, there are two major directions: parallel (denoted with $\parallel$ index) and perpendicular (denoted with $\perp$ index) to the background magnetic field. The perpendicular direction

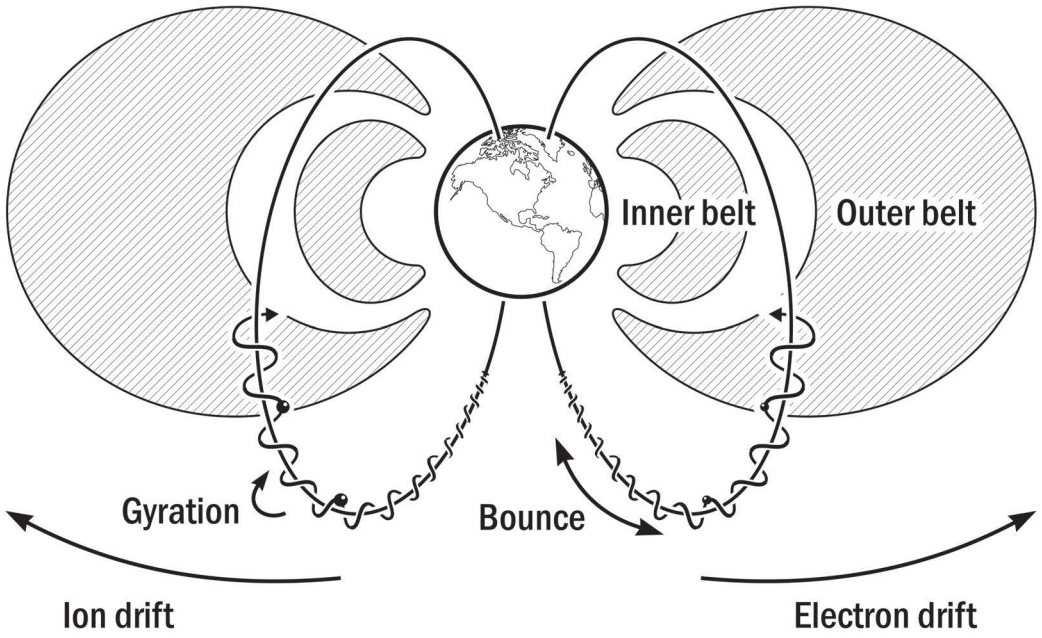

Figure 2.1: Schematical representation of the single charged particle motion in the magnetosphere of the Earth. Electrons and ions complete three types of motion, gyration around the field lines, bouncing along the field lines, and drifting around the Earth (see text for more detail). The direction of gyration and drift is different for positively and negatively charged particles as represented in the schematic. Particles that complete these types of motion are trapped in the magnetic field and construct the Van Allen radiation belts. Image credit: Andy Kale

can also be split into two: quasi-azimuthal and quasi-radial. Quasi-azimuthal (toroidal) direction is defined using a vector perpendicular to the plane containing the background magnetic field and the geocentric radial vector to the particle location. A quasi-radial (poloidal) vector completes the triad. In this coordinate system, the velocity of a particle can be rewritten as $\mathbf{v} = \mathbf{v}_{\parallel} + \mathbf{v}_{\perp}$. Additionally, it is useful to introduce *pitch angle* (α). It is defined as the angle between the velocity of the particle and the direction of the magnetic field line $\alpha = \arctan(v_{\perp}/v_{\parallel})$. This quantity is useful when describing large populations of particles. Another useful parameter for the description of charged particle dynamics in the Earth's magnetosphere is the dipole *L-shell* or simply L (*McIlwain*, 1961). As is shown further below, the centers of gyration of charged particles tend to follow magnetic field lines, even if they are curved. Therefore,

a population of particles following the same magnetic field line, even though they might have different pitch angles, can be labeled by the radial distance along the magnetic equator to the dipole magnetic field line in units of R_E. It provides the ability to describe the population of particles not in (x, y, z) coordinates, but in (E, α, L), where E is the energy of a particle.

2.1.1 Gyro-motion and the First Adiabatic Invariant

Gyration of a charged particle in the presence of a magnetic field is present for a charged particle with a non-zero velocity, in the direction perpendicular to the magnetic field, as a result of the action of the Lorenz force and is and is present even for the uniform field $\mathbf{B}(\mathbf{r}, t) = \mathbf{B}_0 = const$. In this case, the particle has a helical trajectory, completing rotation around the field line with speed $v_\perp$ and moving with the uniform speed $v_\parallel$ along it. The initial conditions define the radius of the gyration and its period. Particularly, if the pitch-angle of a particle is 90° and the velocity of a particle is perpendicular to the field line, then the helix becomes just a circle. Meanwhile, for $\alpha = 0°$ the trajectory is a straight line along the direction of the background field. Figure 2.1 schematically shows the gyration motion of electrons and protons around the field lines. Note that the direction of gyration, clockwise or counterclockwise, is determined by the charge of the particle and is represented on the figure. It can also be convenient to treat the motion of a single particle as a superposition of a circular gyro motion and slower bounce and drift motions. The point around which particle gyrates is called the *guiding center* and it can move, bounce or drift, in the electromagnetic field. This treatment of charged particle motion allows the simplification of the second order differential equation to a set of much simpler first order equations the solution of which is a trajectory of the guiding center.

The Hamilton-Jacobi theory introduces *adiabatic invariants* J_i which are approximately conserved in the system during periodic motion (*Landau and Lifshitz*, 1976). However, a condition on slow variations in the system, with a characteristic timescales of the variations being much larger than the period of the respective motion, should be satisfied. The general equation for an

adiabatic invariant is $J_i = \oint p_i dq_i$, where the integration of the canonical momentum p_i is performed over a single period for generalized coordinate q_i. In case of the particle in a magnetic field, the equation becomes $J_i = \oint_{\Omega_i}(\mathbf{p} + q\mathbf{A})d\mathbf{l}$, where $\mathbf{A}$ is the vector potential of the magnetic field, $d\mathbf{l}$ is a part of the trajectory, and Ω_i denotes different types of periodic motion. For the gyro motion in an arbitrary magnetic field, integration is performed over a single orbit. The adiabatic invariant J_1 associated with gyration becomes $p_\perp^2/2m_0B$, where m_0 is the rest mass of the particle. This quantity is usually called *the first adiabatic invariant* and is denoted as μ:

$$\mu = \frac{mv_\perp^2}{2B} = \frac{mv^2}{2}\frac{\sin^2\alpha}{B}. \tag{2.3}$$

For the relativistic particles, the first adiabatic invariant can be rewritten as $\mu = \frac{p_\perp^2}{2m_0B}$, where $p_\perp$ is the relativistic momentum of the particle in the direction perpendicular to the magnetic field line.

2.1.2 Bounce Motion and the Second Adiabatic Invariant

In the case of inhomogeneity of the magnetic field strength along the field line, a particle with $\alpha \neq 90°$ performs a bounce motion. Figure 2.1 schematically shows the bounce motion of the particle going back and forth along a field line. Due to the conservation of the first adiabatic invariant μ, when the magnitude of the magnetic field B increases it should cause the pitch angle of the particle to increase as well. Upon reaching $\sin^2\alpha = 1$, the particle stops moving along the field line and bounces back in the opposite direction, but still following the magnetic field line. The actual bouncing happens because there is a non-zero gradient of the magnetic field in the parallel ($\|$) direction and the charged particle that performs a circular motion creates a current loop and has the magnetic dipole moment. Therefore, there is a force that acts on the charged particle and points in the direction of lower B. This force is usually referred to as the *mirror force* and is given by the equation $-\mu\partial B/\partial s$, where s is the distance along the field line. The point along the

field line where $\alpha = 90^\circ$ is called *the mirror point* and the magnetic field strength is usually denoted as B_m. Bouncing between two mirror points creates the second type of the periodic motion of the particles in the dipole field. Adiabatic invariant J_2 is associated with this bouncing motion and derived by performing the integration of the particle momenta along the bouncing trajectory. Usually, to remove the dependence on the momentum of a particle from this equation, a related quantity is used for the second adiabatic invariant. It is commonly denoted as $I = J_2/2p = \frac{1}{2}\oint \cos\alpha ds$ (*Walt*, 1994). However, even more common is another related quantity $K = I\sqrt{B_m}$. Using this value as the second adiabatic invariant allows one to account for nonconservative I, B_m, and p when external forces, which are perpendicular to the magnetic field, are present at all times (*Roederer*, 1970). Equation (2.4) shows the final form of the second adiabatic invariant.

$$K = \int_{B'_m}^{B''_m} \sqrt{B_m - B(s)}ds, \tag{2.4}$$

where ds is distance along the field line and B'_m or B''_m are mirror points.

2.1.3 Drift Motion and the Third Adiabatic Invariant

The third and final type of the periodic motion which a charged particle completes in a dipole-like field is the drift motion. Additional forces acting on the guiding center associated with drift motions appear in the direction perpendicular to magnetic field lines due to a number of factors. The full description of different types of drift motion was presented by *Northrop* (1963) where the guiding center motion of a charged particle inside fields with different configurations and with different initial conditions were studied. However, there are two drifts which have a major impact on the movement of a relativistic particle in the outer belt. The first drift is usually called *gradient drift* and appears due to inhomogeneity of $\mathbf{B}$ field i.e., non-zero ∇B. The speed of the guiding center, $\mathbf{V}_G$, due to the gradient drift is given by the equation (2.5) and depends on the particle charge q (*Northrop*, 1963; *Walt*, 1994; *Kivelson*, 1995). In the Earth's magnetosphere, it makes electrons and protons or ions drift around

the Earth in opposite directions as schematically shown in figure 2.1. Because of different drift directionality, the particles create an electrical current, which is usually called the *ring current*.

$$\mathbf{V}_G = \frac{mv_\perp^2}{2qB^3}\left(\mathbf{B}\times\nabla B\right), \tag{2.5}$$

where $v_\perp$ is the speed of a particle in the direction perpendicular to the field line.

Another type of drift motion appears when a particle follows a curved magnetic field line. This drift is commonly referred to as a *curvature drift*. The guiding center speed, $\mathbf{V}_C$, created by the curvature drift is given by equation (2.6). Note that only particles with $v_\parallel \neq 0$ are affected by this motion. Therefore, if the pitch angle of a particle is $\approx 90°$, the impact from the curvature drift is negligibly small. Otherwise, in the dipole or dipole-like field, $\mathbf{V}_C$ has a strong impact and is parallel to $\mathbf{V}_G$ for electrons and ions.

$$\mathbf{V}_C = \frac{mv_\parallel^2}{qR_C}\frac{\mathbf{n}\times\mathbf{B}}{B^2}, \tag{2.6}$$

where R_C is the radius of curvature of a field line, and $\mathbf{n}$ is the unit vector in the direction of the curvature.

Another drift type is called *E cross B* drift and is present for the charged particles that exist in the electromagnetic field with non-parallel $\mathbf{E}$ and $\mathbf{B}$. The speed of this drift is given by equation (2.7).

$$\mathbf{V}_{E\times B} = \frac{\mathbf{E}\times\mathbf{B}}{B^2}. \tag{2.7}$$

Note that E cross B drift is energy independent. Therefore, protons and the low energetic electrons will be greatly subjected to this type of drift. However, for the relativistic electrons, this drift is almost negligible.

The drift motion completes the third and the slowest type of periodic motion of charged particles in the Earth's magnetosphere. Following Hamilton-Jacobi theory, similarly to the gyro and bounce motions, the third adiabatic invariant, J_3, is introduced. $J_3 = \oint(\mathbf{p}+q\mathbf{A})d\mathbf{l}$ where $d\mathbf{l}$ relates to the drift path and can be simplified by assuming that $\mathbf{p}$ is small. After using Stokes' theorem

J_3 becomes $q \oint (\nabla \times \mathbf{A}) \cdot d\mathbf{S} = q \oint \mathbf{B} \cdot d\mathbf{S} = q\Phi$ (*Roederer*, 1970; *Walt*, 1994). The quantity Φ is the magnetic flux enclosed by the drift trajectory and is commonly used instead of J_3. In the dipole field, $\Phi = 2\pi B_0 R_E^3 / R_0$, where R_0 is the distance to the trajectory of a charged particle in the magnetic equatorial plane. However, quite commonly instead of Φ, the value $L^*= -2\pi M_0/\Phi R_E$ is also used. L^* is a dimensionless parameter, which is usually referred to as *generalized L-value*. L^* has properties similar to a regular L-shell and in the realistic magnetic field $L^* \approx L$ close to the Earth. Originally, L^* was defined by *Roederer* (1970) for a non-dipole background magnetic field. From the physical perspective, it is the radial distance from the center of the Earth along the magnetic equator where a charged particle would be if the magnetic field was dipole and the particle had the same Φ. In other words, L^* in a dipole field is the same as L, but for realistic fields, they are different (*Roederer*, 1970).

A combination of three adiabatic invariants (μ, K, and L^*) can be used as independent variables to define the phase space of the trapped particles. Studying the particle distribution in the radiation belt in such a phase space is useful for understanding of the radiation belt dynamics.

2.2 Motion of Systems of Charged Particles

2.2.1 General Theory

Due to the current state of technology, the measurements and thus the analysis of the particles in the Van Allen belts involve many particles at once. Therefore, terms *flux* and *phase space density* (PSD) have been introduced to describe the trapped radiation. Both flux and PSD describe the population, dynamics, and intensity of the radiation belts. Flux is the quantity which is produced by many radiation belt survey missions. It is usually defined in terms of a differential flux per unit energy such that as the number of particles with energies from E to $E + dE$ which cross a unit area perpendicular to the given direction within a unit solid angle. The units of differential flux are $cm^{-2}s^{-1}sr^{-1}MeV^{-1}$. Spacecraft missions typically provide the differential flux as a function of energy E and pitch angle α for a given position in space.

Meanwhile, another way to describe the radiation belt population is using the phase space density (*Walt*, 1994). It is defined as the number of particles in a unit of a six-dimensional phase space. It is constructed on three orthogonal spatial dimensions and three conjugate momenta. In plasma physics, PSD is usually provided as a function of three adiabatic invariants (μ, K, L^*) or (μ, K, Φ) at a certain time and is typically quoted in terms of units of $(c\,cm^{-1}MeV^{-1})^3$. Investigation of the PSD allows one to examine the observed dynamics of the particles more accurately than can be done by using flux data. Especially, the transformation of the flux, j, to PSD, F, is required to take care of adiabatic effects during the main phase of the storm such as the "Dst effect" (*Li et al.*, 1997). Using Liouville's theorem, it can be shown that the relation between flux and PSD is $F(\mathbf{q}, \mathbf{p}) = j(\alpha, E)/p^2$ (see e.g., the proof in *Walt*, 1994). This study presents the analysis of both flux and PSD during different geomagnetic storms with the goal of explaining the dynamics of the outer radiation belt.

If the adiabatic invariants described in the previous section were always conserved, the ensemble of the trapped charged particles, described in terms of the constant adiabatic invariants, would remain unchanged in the radiation belts forever. However, the observations of the trapped populations show significant variability in response to solar wind forcing. The PSD and flux of particles in the outer radiation belt are continuously changing. This happens due to the interaction of charged particles with plasma waves that are created in the Earth's magnetosphere due to changes in the solar wind conditions. If the perturbed electromagnetic fields associated with the plasma waves have the same characteristic timescales as one of the types of periodic motion, gyration, bounce, or drift, the corresponding adiabatic invariant would not be conserved in the system, causing the population of trapped particle radiation to vary. However, instead of investigating the dynamics of individual particles and their interactions with the waves the problem of simulating the global radiation belt population can instead be approached using a diffusive paradigm. The impact of the waves on the particles can be assessed by using an approach which uses empirical parameterizations of the wave characteristics, such as

power as a function of frequency, in terms of geomagnetic indices or solar wind variables. This parametrization can be used to simulate the behavior of the trapped radiation in the magnetosphere using diffusion equations. Note that the diffusion paradigm assumes that the changes in the trapped particle radiation happen slowly, i.e., the effects of multiple wave-particle interactions are required for changes to have a reasonable effect on the population.

The general equation which describes the motion of the particles in terms of the phase space density F is the Fokker-Planck equation in the diffusion form (see the derivation in *Walt*, 1994):

$$\frac{\partial F(\mu, K, \Phi)}{\partial t} = \frac{\partial}{\partial x_i}\left(\frac{\langle \Delta x_i \Delta x_j \rangle}{2}\frac{\partial}{\partial x_j}F(\mu, K, \Phi)\right), \tag{2.8}$$

where x is one of the adiabatic invariants (μ, K, Φ) and $\frac{1}{2}\langle \Delta x_i \Delta x_j \rangle = D_{ij}$ is the diffusion tensor. It, alongside with gradients in PSD, controls how fast the particles are transported in phase space. Additionally, there are many different coordinate systems which are suitable to investigate different processes. For example, when considering the diffusion due to the violation of the third adiabatic invariant Φ, a representation of PSD in (μ, K, Φ) or (μ, K, L^*) are reasonable choices. Meanwhile, for pitch angle diffusion, the system (E, α, L) is the most convenient (*Walt*, 1994; *Schulz and Lanzerotti*, 1974).

Different perturbations can create different kinds of diffusion in the magnetic field of the Earth. As was described previously in section 1.2, according to the current theories, trapped particles can be lost downward to the atmosphere of the Earth, or outward across the magnetopause to the magnetosheath through the magnetopause shadowing. The atmospheric loss usually involves interactions with high-frequency waves and pitch angle scattering into the loss cone. Violation of the first and the second adiabatic invariants can cause particles to diffuse in pitch angle. Examples of waves which might cause such an atmospheric loss are electromagnetic ion cyclotron (EMIC) waves (e.g., *Kersten et al.*, 2014; *Kang et al.*, 2016; *Shprits et al.*, 2016), plasmaspheric hiss (e.g. *Thorne et al.*, 1973; *Lee et al.*, 2013), or chorus waves (e.g., *Shprits et al.*, 2007; *Li et al.*, 2014). Meanwhile, outward losses as a result of magnetopause

shadowing can be enhanced by outward diffusion due to interactions with ultralow frequency (ULF) waves (e.g., *Shprits et al.*, 2006; *Loto'aniu et al.*, 2010; *Mann and Ozeke*, 2016; *Mann et al.*, 2016). In this case, the third adiabatic invariant is being violated and the first and the second invariants stay constant. This thesis focuses on radial diffusion and the impact of ULF waves on the trapped particle radiation. The next section provides some insight into the radial diffusion problem, the calculation of radial diffusion coefficients, and determination of the boundary conditions.

2.2.2 Radial Diffusion

Electromagnetic perturbations with characteristic times on the order of $\sim$10 min should be present in the magnetosphere for the radial diffusion of electrons to occur. In this case, perturbations have the same time scale as the drift time of relativistic electrons in the outer Van Allen belt. Therefore, changes with such timescales can violate the conservation of the third adiabatic invariant of the relativistic electrons in the system. Note that the third adiabatic invariant Φ can be represented in terms of radial distance using L^* which is a coordinate which is similar to radial distance, as was described previously. The violation of this invariant causes the charged particles to move in the outward direction to be potentially ultimately lost to the magnetosheath, or in the inward direction and be accelerated, depending on the availability of the source population and the radial gradients of PSD. This process is called the *radial diffusion* and has been investigated for a long time (e.g., *Schulz and Lanzerotti*, 1974; *Elkington and Sarris*, 2016, and references therein).

Equation (2.8) provides a general form of diffusion equation in (μ, K, Φ) space. However, the most convenient description of radial diffusion is in (μ, K, L^*) space, since L or L^* are easier to associate with experimental measurements for example on satellites. Therefore, in such an approach a transformation from (μ, K, Φ) coordinates to (μ, K, L^*) is required. This is performed by using Jacobian matrix, determinant of which in this case is equal to L^{-2}. Therefore, a form of equation (2.8) for investigating the diffusion in L is given by equation (2.9), where $x_i = L$, $x_j = L$, and $\frac{\langle \Delta x_i \Delta x_j \rangle}{2} = D_{ij} = D_{LL}$ is

the diffusion coefficient.

$$\frac{\partial F(\mu, K, L)}{\partial t} = \frac{\partial}{\partial L}\left(\frac{D_{LL}}{L^2}\frac{\partial}{\partial L}L^2 F(\mu, K, L)\right). \tag{2.9}$$

Brizard and Chan (2001) (see also *Fei et al.*, 2006) derived relations for the radial diffusion coefficient (D_{LL}) as a function of the ULF wave power, P, of perturbations in electric, P^E, and magnetic fields, P^B. *Fei et al.* (2006) showed that the electric diffusion coefficient D_{LL}^E for electrons with drift frequency ω_d is given by equation (2.10a). The D_{LL}^E coefficient is proportional to the sum of wave powers $P_m^E(m\omega_d)$, where wave frequency ω satisfies the drift resonance condition $\omega = m\omega_d$ and where m is the azimuthal wave number. A similar proportionality to wave power also exists for magnetically induced diffusion, with diffusion coefficient D_{LL}^B (equation 2.10b). Typically the overall diffusion is assumed to be described by the sum of the two coefficients, providing the total diffusion coefficient for the system $D_{LL} = D_{LL}^E + D_{LL}^B$. As shown by *Fei et al.* (2006), these diffusion coefficients can be described in a dipole field by

$$D_{LL}^E = \frac{1}{8B_E^2 R_E^2} L^6 \sum_m P_m^E(m\omega_d), \tag{2.10a}$$

$$D_{LL}^B = \frac{\mu^2}{8q^2\gamma^2 B_E^2 R_E^2} L^4 \sum_m m^2 P_m^B(m\omega_d), \tag{2.10b}$$

where γ is the relativistic gamma factor and B_E is the equatorial magnetic field strength at the surface of the Earth.

In later studies, *Ozeke et al.* (2014) simplified the assumed wave-particle interactions by only considering the first drift resonance mode ($m = 1$). The formulas for D_{LL}^E and D_{LL}^B derived by *Ozeke et al.* (2014) are shown in equations (2.11a) and (2.11b). Here, the angular drift frequency, ω_d, was substituted by the wave frequency f in the above formulas (2.10), according to the drift resonance condition $\omega_d = \omega = 2\pi f$ for the assumed azimuthal wave number $m = 1$.

This study uses these formulas to calculate the radial diffusion coefficients from in-situ field measurements from different satellites. Note that *Ozeke et al.*

(2014) treat D_{LL}^{E} and D_{LL}^{B} as constant values, independent of wave frequency f (or particle energy, which defines ω_d). To derive D_{LL}^{E} and D_{LL}^{B} parametrizations *Ozeke et al.* (2014) used an assumption, based on the statistical analysis of electromagnetic perturbations, that the power spectral density of the compressional component of the magnetic field is proportional to f^{-2} and the wave power of the quasi-azimuthal component is frequency independent. Therefore, substituting such dependencies into the above formulas, the D_{LL}^{E} and D_{LL}^{B} coefficients appear to have no wave frequency dependence. However, this thesis focuses on investigating the characteristics of the frequency dependence of the power spectral density and therefore the impact of the observed frequency dependence on the resulting diffusion coefficients during different phases of the magnetic storm. The notation $D_{LL}^{E}(f)$ and $D_{LL}^{B}(f)$ is used in the text to emphasize the frequency dependence of the radial diffusion coefficients. Also, keeping the notation introduced by *Ozeke et al.* (2014), P^{E} represents the power spectral density of disturbances in the quasi-azimuthal component of the electric field, and P^{B} represents the power spectral density in the compressional component of the magnetic field:

$$D_{LL}^{E}(f) = \frac{L^{6}}{8B_{E}^{2}R_{E}^{2}} P^{E}(f), \tag{2.11a}$$

$$D_{LL}^{B}(f) = \frac{L^{8}4\pi^{2}}{9 \times 8B_{E}^{2}} P^{B}(f) f^{2}. \tag{2.11b}$$

Additionally, *Ozeke et al.* (2014) obtained a Kp-parametrization of D_{LL}^{E} and D_{LL}^{B} given in equations 2.12a and 2.12b, in units of days^{-1}. Note that Kp index is one of the geomagnetic indices used in space physics and is defined as the maximum fluctuations of horizontal magnetic field component measured by ground-based magnetometers during a three-hour interval across different latitudes. The *Ozeke et al.* (2014) formulas are commonly used in time-dependent radial diffusion simulations (e.g., *Mann et al.*, 2016; *Schiller et al.*, 2016; *Ozeke et al.*, 2017). In this Chapter, the Kp-parametrization of D_{LL} coefficients is compared with the results obtained using in-situ observa-

tions of the electric and magnetic fields during the March 17-18, 2015 intense geomagnetic storm.

$$D_{LL}^{E} = 2.1 \cdot 10^{-8} L^{6} 10^{0.217L+0.461Kp}, \tag{2.12a}$$

$$D_{LL}^{B} = 6.62 \cdot 10^{-13} L^{8} 10^{-0.0327L^{2}+0.625L-0.0108Kp^{2}+0.499Kp}. \tag{2.12b}$$

Another thing that should be considered when solving a diffusion equation is the boundary conditions. The magnetopause, by definition, serves as the outer boundary for the Earth's magnetic field. Therefore, when a particle leaves the magnetosphere, crosses the magnetopause, and enters the magnetosheath, it is no longer trapped by the Earth's magnetic field. Instead, it experiences the IMF brought by the solar wind. This particle is in general thought to be lost from the radiation belts. Hence, knowing the location of the magnetopause is crucial when solving the radial diffusion problem. The general approach to calculate the magnetopause location is to use the *Shue et al.* (1998) empirical model of magnetopause standoff distance. This model provides a distance from the Earth to the subsolar part of the magnetopause in units of R_E based on solar wind parameters. Note that due to the non-uniform magnetic field, the gradient-curvature drift trajectories of Van Allen belt electrons are not circular such that electrons from lower radial distances at local times away from noon can still drift outwards to impact the magnetopause. This defines the last closed drift shell which in effect defines the maximum extent of the outer radiation belt. In addition, outwards ULF wave diffusion can also transport particles even further inwards onto drift shells which intersect the magnetopause – resulting in enhanced magnetopause shadowing losses. Chapter 4 of this thesis focuses on examining the impacts of the outer boundary for radiation belt losses during magnetic storms.

Chapter 3

Role of the Radial Diffusion During 17-18 March, 2015 Geomagnetic Storm

In this chapter we analyze ultralow frequency wave dynamics in the magnetosphere during the intense geomagnetic storm on March 17-18, 2015. During this event, the population of ultra-relativistic electrons was depleted within 2 hours after the storm commencement, before strongly recovering to reach fluxes above pre-storm levels. We study Pc4-Pc5 ULF perturbations which, depending upon the availability of source populations, can cause outward radial diffusion and loss to the magnetosheath, or inward transport and acceleration. Analysis of measurements from GOES and THEMIS satellites and ground-based magnetometers shows that the main phase storm-specific radial diffusion coefficients do not correspond to statistical estimates. Specifically, during the main phase, the electric diffusion (D_{LL}^{E}) is reduced, and the magnetic diffusion (D_{LL}^{B}) is increased, compared to empirical models based on Kp. Contrary to prior results, the main phase magnetic radial diffusion cannot be neglected. The largest discrepancies, and periods of dominance of D_{LL}^{B} over D_{LL}^{E}, occur during intervals of strongly southward IMF. However, during storm recovery, both magnetic and electric diffusion rates are consistent with empirical estimates. We further verify observationally, for the first time, an energy coherence for both D_{LL}^{B} and D_{LL}^{E} during both main and recovery phases. Our results show that, at least for this storm, properly characterizing the main

phase radial diffusion, potentially associated with enhanced ULF wave magnetopause shadowing losses, cannot be done with standard empirical models. Modifications, associated especially with southward IMF which enhance the effects of D_{LL}^{B} and introduce larger main phase outward transport losses, are needed.

The contents of this Chapter has been submitted to the Journal of Geophysical Research and is currently under review (*Olifer et al.*, 2018a), where I performed the data analysis and was in charge of composing the manuscript. Meanwhile, I.R. Mann, I.J. Rae, and S.K. Morley were advisors in this project, L.G. Ozeke performed mapping of the equatorial quasi-azimuthal electric field from the magnetic east-west D-component of magnetic field on the ground. Additionally, S.K. Morley helped with obtaining and interpreting electron flux data from the GPS satellite constellation.

3.1 Data and Methodology

In this section, we present an overview of the March 2015 geomagnetic storm and describe the methodology which we used to study the diffusion coefficients. We analyze in-situ fields data from THEMIS (*Angelopoulos*, 2008) and GOES (*Singer et al.*, 1996) satellites, as well as from multiple ground-based magnetometers, to calculate radial diffusion coefficients. The analysis is performed for 17-18 of March 2015 during the main phase and early recovery phase of the storm.

3.1.1 Overview of the March 2015 storm

A summary of the solar wind, resulting geomagnetic indices, and the resulting 2.6 MeV radiation belt flux response for the March 2015 storm are shown in Figure 3.1. Solar wind data was taken from Operating Missions as a Node on the Internet (OMNI) database (*King*, 2005). Energetic particle data was taken from NASA's Van Allen Probes database for the Relativistic Electron-Proton Telescope (REPT) instrument (*Baker et al.*, 2013a). Figure 3.1 shows that the radiation belt loss happened on a timescale which is too short to be fully

resolved along the orbit of the Van Allen Probes mission, the orbital period being too long to provide an explicit picture of what happened.

The interplanetary shock arrives at 03:40 UT on March 17, 2015. However, as discussed by *Olifer et al.* (2018b), the particle flux data does not show any signs of significant loss until 06:00 UT, when the interplanetary magnetic field (IMF) turns southward. This observation was used by *Olifer et al.* (2018b) to argue that magnetopause shadowing dominated as a governing factor of the loss during this event. The LCDS on March 17, 2015 also reaches low L^* down to L^*=4 and stays there for a relatively long period of ∼5 hours. Presumably, this time is enough to deplete the heart of the radiation belt for example through fast outward ULF wave radial diffusion (e.g., *Mann et al.*, 2016; *Turner et al.*, 2012).

3.1.2 THEMIS Data

In this study, we used data from the three THEMIS satellites A, D, and E. In-situ measurements of the magnetic field are taken from the triaxial fluxgate magnetometer experiment (*Auster et al.*, 2008). Measurements of the electric field are taken from the Electric Field Instrument (EFI) (*Bonnell et al.*, 2008). Both data sets are level 2 processed data and have 3 second resolution. ULF wave power spectral density, which is required to calculate the radial diffusion coefficients, can be obtained up to 167 mHz. Because we study ULF wave perturbations, the analysis of the wave power is performed for the frequency range from 1.2 mHz to 20 mHz which corresponds appropriately to Pc4-Pc5 waves. Electric and magnetic field data were provided by the Coordinated Data Analysis Web (CDAWeb) database in geocentric solar magnetospheric (GSM) coordinates. However, the transformation of these datasets from GSM to field aligned coordinates (FAC) is required for our D_{LL} calculation. Field aligned coordinates were defined in the parallel direction by the background field, and in quasi-azimuthal (toroidal) direction using a vector perpendicular to the plane containing the background magnetic field and the geocentric radial vector to the spacecraft location. A quasi-radial (poloidal) vector completes the triad. For this purpose, the position of the THEMIS probes was taken

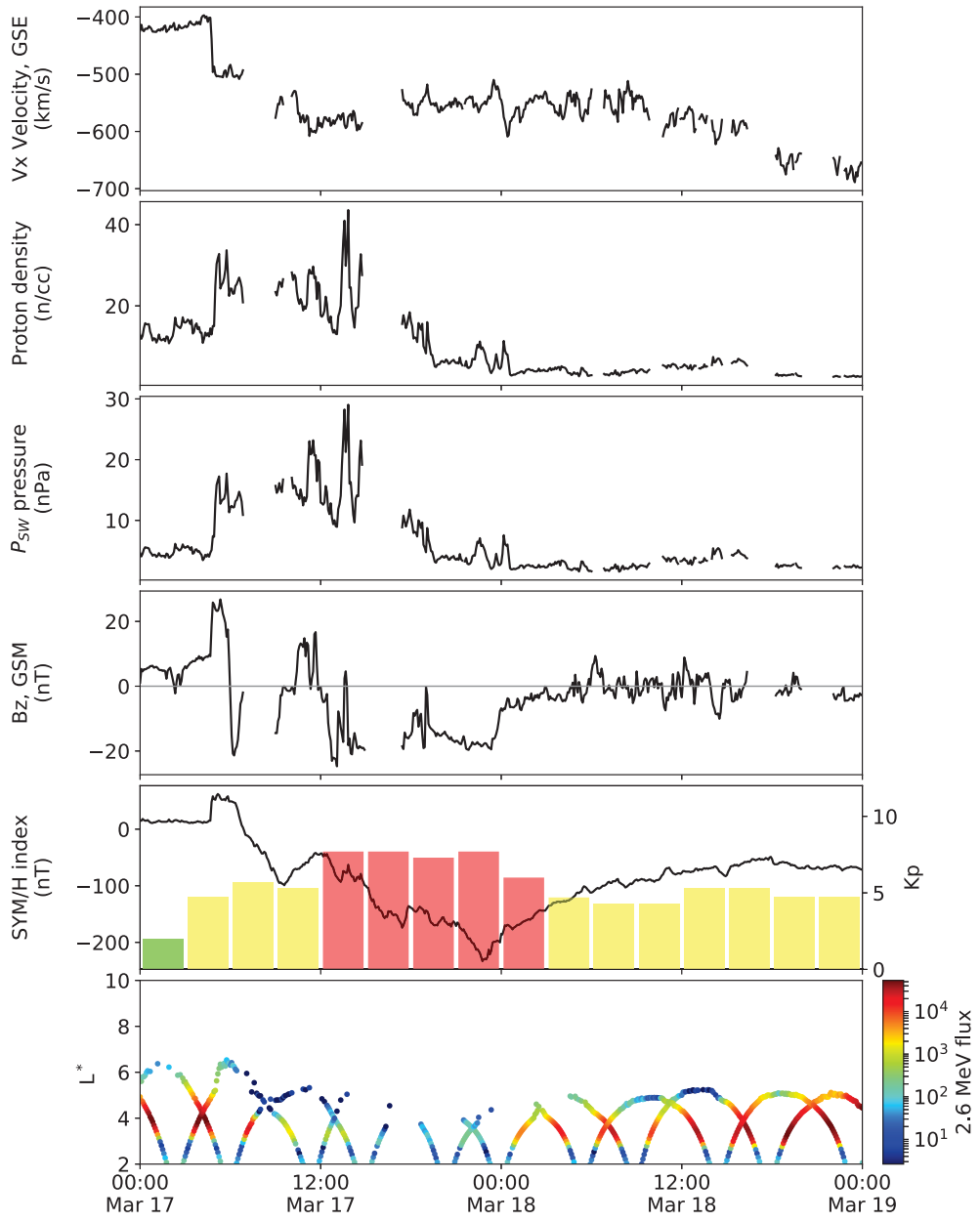

Figure 3.1: Summary of selected solar wind parameters and geomagnetic indices, and 2.6 MeV radiation belt electron response during the 17-18 March 2015 geomagnetic storm. From top to bottom: solar wind velocity x-component in GSE coordinates; solar wind proton number density; solar wind dynamic pressure; z-component of the interplanetary magnetic field in GSM coordinates; geomagnetic SYM-H index as a line plot and Kp index as a bar plot; and 2.6 MeV electron differential flux measured by the Van Allen Probes as a function of L^* and time in $\mathrm{cm}^{-2}\mathrm{s}^{-1}\mathrm{sr}^{-1}\mathrm{MeV}^{-1}$.

from the Space Physics Data Facility (SPDF) Locator database. Meanwhile, the background magnetic field was calculated from in-situ measurements for each of the probes after applying a running average with a 20 minute window. The analysis created a negligibly small parallel component of the electric field, validating the FAC approach.

The power spectral densities are calculated for the compressional component of the magnetic field ($B_{\parallel}$) and the quasi-azimuthal component of the electric field (E_{ϕ}) after applying a Hanning window (*Oppenheim et al.*, 1999) with a total width of 40 minutes. The calculation of D_{LL} is performed only for L-shell range from 4.0 to 7.5, lower L-shell ranges introduce power that is aliased into the ULF band but derives from the rapid variation of the background magnetic field along the THEMIS orbit. Inbound and outbound passes of the THEMIS A, D, and E probes cover time periods from around 11:00 UT until 20:00 UT for each day during March 2015 in the noon and dusk sectors. Note that the radiation belt loss happens between around 07:00 UT and 12:00 UT. Therefore, due to its orbital location, the in-situ THEMIS data does not provide insight during the beginning of the storm. However it still captures ULF wave characteristics at the end of the main phase.

3.1.3 GOES Data

In addition to the THEMIS satellites, we used in-situ measurements of the magnetic field from geosynchronous orbit, provided by the GOES-13 and GOES-15 satellites. The fluxgate magnetometer (*Singer et al.*, 1996) measurements were obtained from the National Centers for Environmental Information National Oceanic and Atmospheric Administration database. The magnetometer data is provided with 512 ms resolution in spacecraft coordinates (see *Fraser et al.*, 2013, for more detail). Following the same procedure as for the THEMIS data, the magnetic field measurements are transformed into FAC, and the wave power of Pc4-Pc5 waves in the $B_{\parallel}$ component calculated along the whole orbit of the GOES-13 and GOES-15 satellites.

3.1.4 Ground-based Magnetometer Data

We also use ground-based magnetometer data to estimate electric diffusion in the equatorial plane and compare this to the rates of diffusion estimated from GOES and THEMIS data. We use the mapping technique of *Ozeke et al.* (2009) to obtain equatorial quasi-azimuthal electric field E_ϕ from the magnetic east-west D-component of magnetic field on the ground. We use measurements of the magnetic field obtained by the CARISMA magnetometer array (*Mann et al.*, 2008) and AUTUMN magnetometer array (*Connors et al.*, 2016). In particular, we use the magnetometer data from Fort Smith (L=6.69) to obtain E_ϕ near GOES-13, and the magnetometer data from Inukjuak (L=6.91) to obtain E_ϕ near GOES-15. Fort Smith magnetometer data is taken from the CARISMA website with 1 second resolution. Inukjuak magnetometer data is taken from the AUTUMN Virtual Magnetic Observatory website with 0.5 second resolution. Note that the assured dipolar field line mapping (*Ozeke et al.*, 2009) is most accurate on the day side of the magnetosphere and therefore E_ϕ is obtained for magnetic local time (MLT) between 06:00 and 18:00. This also removes the effects of nightside bags and other nightside or substorm processes with signatures in the Pc4-Pc5 ULF band for the ULF wave analysis. The footprints of the GOES satellites, as well as ground station locations, are shown in the Figure 3.2 as calculated using Tsyganenko 2005 (TS04D) magnetic field model. The height of the ionosphere is assumed constant and equal to 100 km.

3.2 Analysis of the Radial Transport

In this section, we calculate observationally constrained event-specific radial diffusion coefficients for the March 17-18, 2015, geomagnetic storm using in-situ data from the GOES and THEMIS satellites. Note that the orbit of the Van Allen Probes lies in the magnetotail during this storm. Therefore, we do not present D_{LL} coefficients derived from the fields measured by the Van Allen Probes since they are located in stretched fields on the night side. The locations of the GOES and THEMIS satellites in the GSE X-Y plane

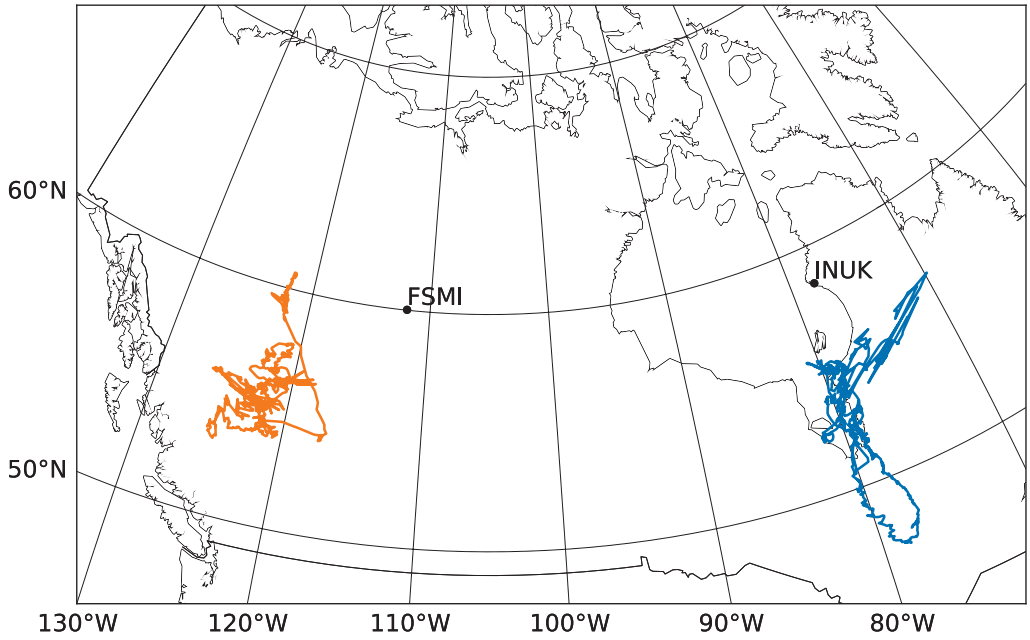

Figure 3.2: Magnetic field line traced footprints of the GOES-13 (blue line) and GOES-15 (orange line) satellites with respect to the ground magnetometers at Fort Smith (FSMI) and Inukjuak (INUK). Field line tracing was performed using Tsyganenko 2005 (TS04D) magnetic field model.

are shown in Figure 3.3. Since the focus of this chapter includes analysis of possible outwards radial transport to the magnetopause during the main phase of the storm, the considered GOES and THEMIS datasets provide appropriate coverage at hight L-shells with which to address this topic.

3.2.1 D_{LL} from THEMIS satellites

Figure 3.4 shows ULF wave field power spectral density as a function of time and frequency for perturbations in the electromagnetic fields measured by the THEMIS-A, -D, and -E satellites. We show inbound, and outbound passes of THEMIS-A, -D, and -E probes on each panel of the plot designating them with different colors. Data from the THEMIS-A satellite is shown in Figure 3.4, and throughout the chapter, with a red background and red-colored labels. Meanwhile, green color represents THEMIS-E, and blue color represents THEMIS-D, respectively the labels on the top of each plot also designate

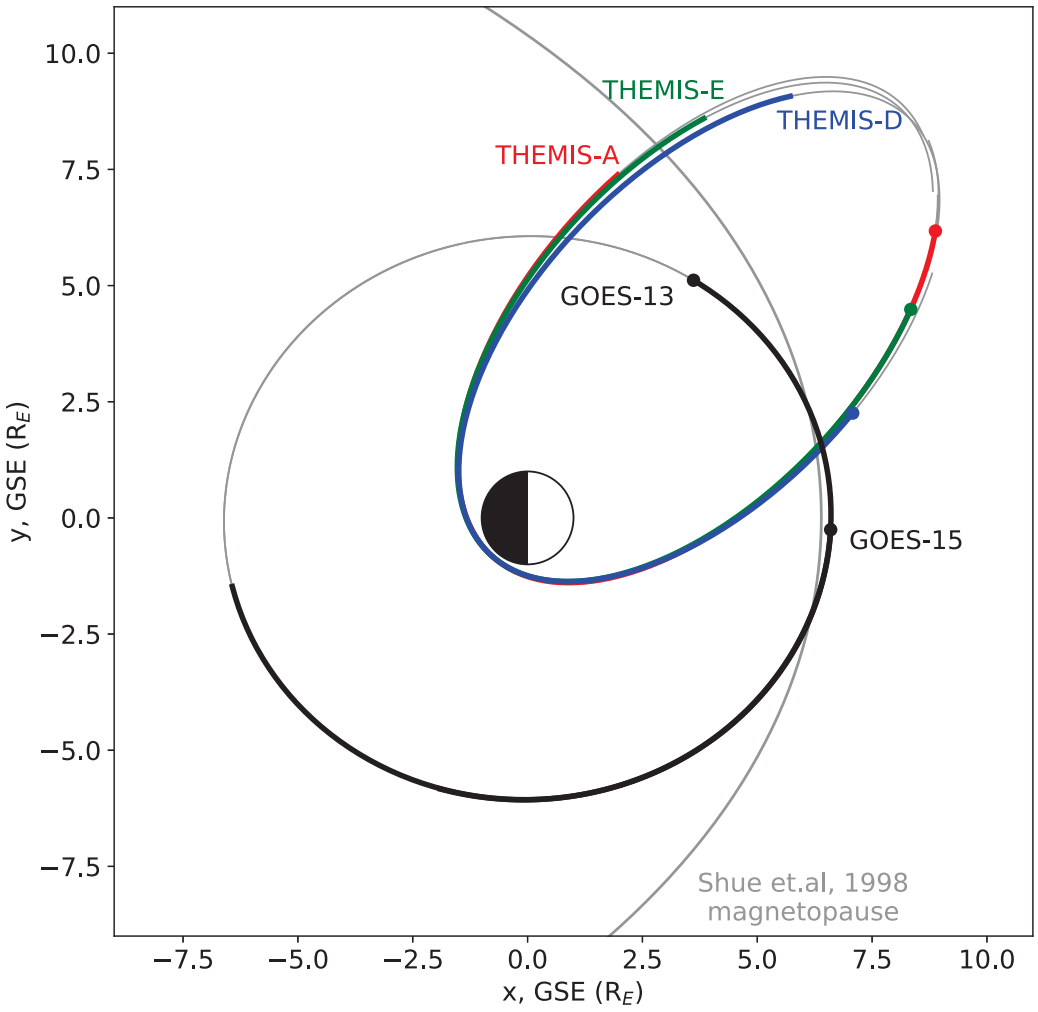

Figure 3.3: Orbits of the GOES and THEMIS satellites in the GSE X-Y plane during 17 March 2015. The orbit of THEMIS-A satellite is shown with red color, of THEMIS-D with blue, of THEMIS-E with green, and both GOES satellites are with black. Parts of the orbit from 10:00 until 21:00 UT shown in color the respective, meanwhile the remaining parts of the orbits are in grey. The round points represent the final position of the satellites at 21:00 UT on 17 March 2015. Additionally, we show the magnetopause locations as calculated by *Shue et al.* (1998) empirical model.

different probe (A, D, or E) and distinguish between their inbound (in) and outbound (out) passes. Note that we show only the time period between 10:30 UT and 21:00 UT for both March 17 and March 18, breaking the x-axis between two periods. THEMIS satellites spend only ∼10 hours per day in the outer radiation belt, and this representation makes the presentation clearer.

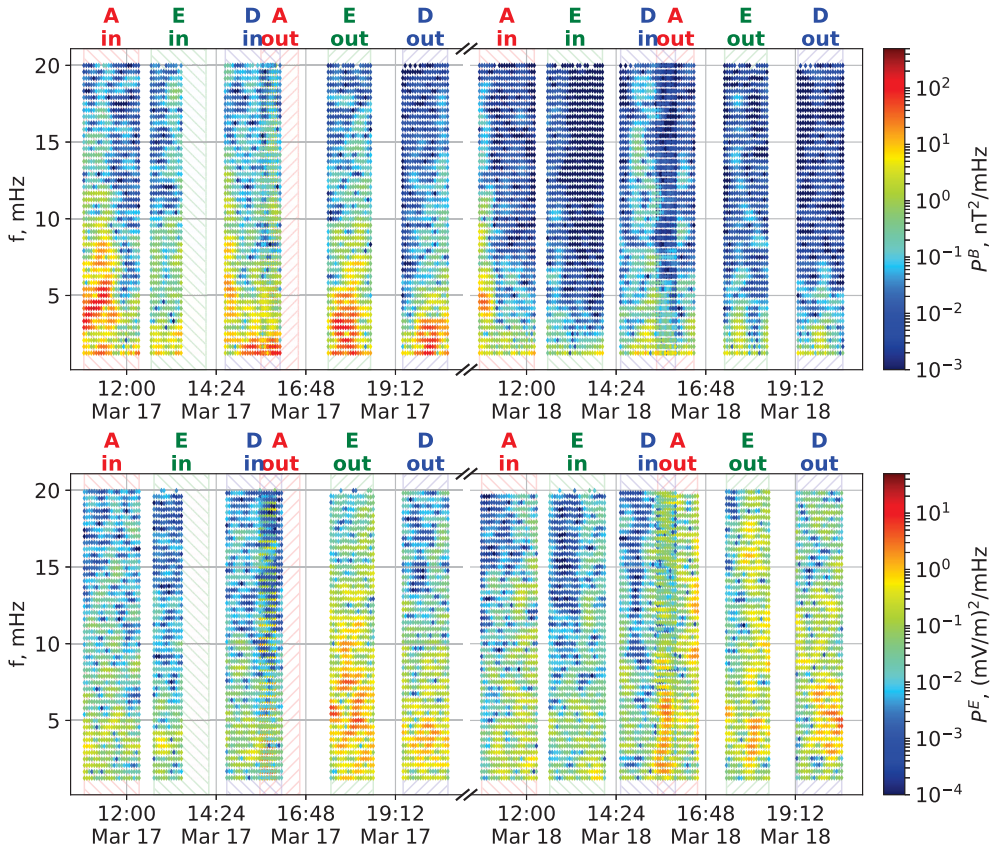

Figure 3.4: Spectrograms of ULF perturbations in the compressional component of the magnetic field $B_{\parallel}$ (top panel) and the quasi-azimuthal component of the electric field E_{ϕ} (bottom panel) measured by the THEMIS satellites from 10:30 till 21:00 UT on both March 17 and 18, 2015. The soft highlighted background in red indicates data obtained from THEMIS-A satellite, the blue color corresponds to THEMIS-E, and the green color corresponds to THEMIS-D. Note that we show inbound and outbound passes of all three satellites on the same plot and label them above each panel "in" or "out", respectively. Also note that the inbound pass of THEMIS-D overlaps with the outbound pass of THEMIS-A at around 15:00 UT. Times when the data is absent for THEMIS-E and when THEMIS-A is in the magnetosheath are not shown on the plot.

The top panel of Figure 3.4 shows a spectrogram of ULF wave power spectral density in the compressional component of the magnetic field (P^B). A relatively large power spectral density $\gtrsim$1 nT^2/mHz is present for frequencies $\leq$ 5 mHz during the main phase of the storm on March 17. Figure 3.4 shows that during the progression of the UT day on March 17, the substantial compressional power is bounded by a frequency which subsides from 10 mHz, as

measured during an inbound pass of THEMIS-A, to 3 mHz towards the end of the main phase at the end of the UT day on the March 17, as measured during an outbound pass of THEMIS-D. The majority of the compressional wave power is confined to low frequencies of <3 mHz during the first day of the recovery phase on March 18. Meanwhile, the bottom panel of Figure 3.4 shows that the wave power in the quasi-azimuthal component of the electric field is spread over a large frequency range. Unlike the power spectral density of the magnetic component, P^E shows a strong magnetic local time (MLT) dependence. Low values of $P^E \leq 0.5\,(\mathrm{mV/m})^2/\mathrm{mHz}$ are, in general, present on the dusk side during the inbound passes of the THEMIS probes. Meanwhile, relatively large values of $P^E \geq 0.5\,(\mathrm{mV/m})^2/\mathrm{mHz}$ are present in the noon sector as measured during the outbound passes of the THEMIS satellites. Additionally, there is no significant change in the power spectral density for the E_ϕ component between the main phase and the recovery phase of the storm in the noon sector (at ∼15-21 UT). During the recovery phase the P^E power spectra show some evidence of the energy independence consistent with the Kp-dependent empirical statistical models (e.g., *Ozeke et al.*, 2014). In the main phase, however, the spectra appear to be dominated by the power below 10 mHz.

There are two time regions missing on Figure 3.4 when the data has no correct physical interpretation from the point of the radial diffusion. The first one, during the outbound pass of THEMIS-A on March 17 (from 16:00 UT until 16:30 UT) in P^B, when THEMIS-A had crossed the magnetopause and was outside the magnetosphere. The second, during the inbound pass of THEMIS-E on March 17 (from 13:30 UT until 14:00 UT) in P^E, during which THEMIS-E has unrealistic electric field measurements. Therefore these two regions are ignored in the subsequential analysis. We do not show data from these times in our resultant plots so as not to distract the reader.

Figure 3.5 shows the D_{LL}^B coefficient calculated using equation (2.11b), where $P^B\,(f)$ is taken using data from the top panel of Figure 3.4. Figure 3.5 shows the value of the D_{LL}^B coefficient as a function of electron energy, W, and time. The energy dependence is obtained by using the previous assumption

that $m = 1$ and therefore that the wave angular frequency $\omega = 2\pi f$ is the same as the drift frequency ω_d of an electron. Because ω_d is a function of the relativistic energy of a particle, we use a transformation between wave frequency, f in Hz, and energy, W in MeV, in the form of equation (3.1), where

$$W = \frac{m_0 c^2}{2}\left(\frac{2}{3}\frac{C_d f}{L} + \sqrt{\frac{4}{9}\frac{C_d^2 f^2}{L^2} + 4}\right), \tag{3.1}$$

and $m_0 c^2 = 0.511$ MeV is the rest mass of an electron in units of energy, and C_d is a numerically obtained coefficient and is equal to $1.557 \cdot 10^4$ sec for electrons (*Walt*, 1994). We further only consider particles with 90° equatorial pitch angle. The same approach is used to analyze the D_{LL}^E coefficients shown in Figure 3.6.

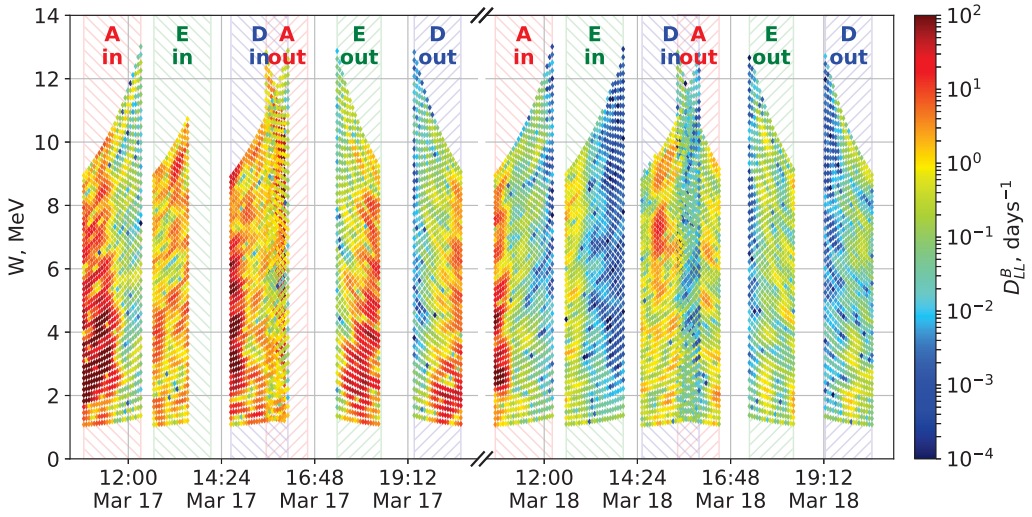

Figure 3.5: D_{LL}^B as a function of time and energy using local measurements of compressional ULF wave power spectral density P^B recorded by THEMIS-A, -D, and -E. Drift (m=1) resonance and a dipole magnetic field are assumed and D_{LL}^B is calculated using the *Fei et al.* (2006) formulas. The color scheme for this plot is the same as in Figure 3.4. The energy dependence was obtained by calculating the drift resonance (m=1) electron energy for the waves in the frequency range from 1.2 to 20 mHz. See text for more detail.

Figures 3.5 and 3.6 show that both the D_{LL}^B and D_{LL}^E coefficients show relatively coherent behavior as a function of energy during this interval, i.e., the magnitudes of the diffusion coefficients as determined using local field mea-

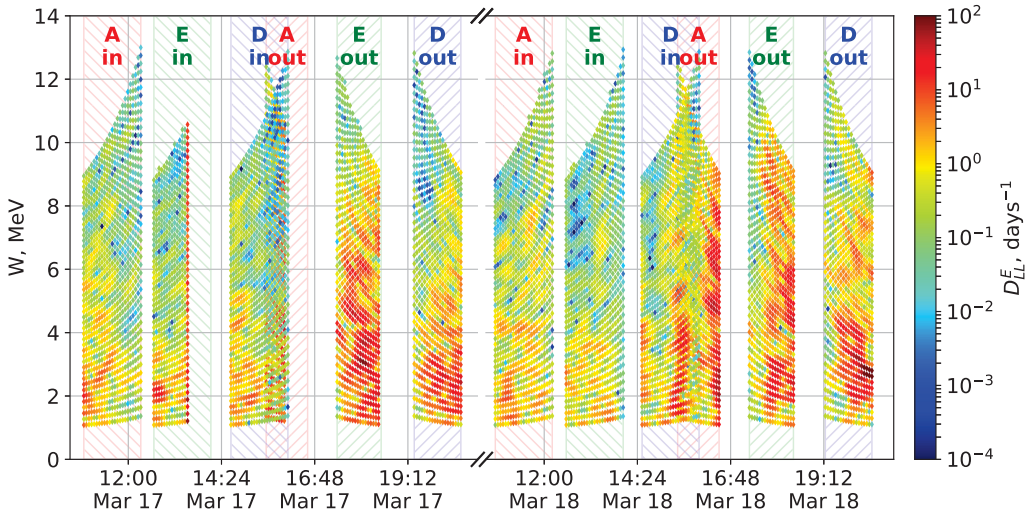

Figure 3.6: D_{LL}^E as a function of time and energy using local measurements of quasi-azimuthal ULF wave power spectral density P^E recorded by THEMIS-A, -D, and -E. The same format as Figure 3.5.

surements from THEMIS indicate a time and position dependence which is mostly independent of energy. Consistent with prior statistical models (e.g., *Ozeke et al.*, 2014), both D_{LL}^B and D_{LL}^E have a strong L-shell dependence with larger magnitudes on the higher L-shells. However, some energy-dependent features associated with the ULF wave packets still exist. For example, in D_{LL}^B during the end of the outbound pass of THEMIS-A on March 18. Additionally, Figure 3.6 shows signs of a weak energy-dependence during the main phase of the storm with higher D_{LL}^E at lower energies. This dependence becomes less apparent during the recovery phase on March 18 where the electric diffusion coefficient shows a much more coherent behavior across different energies. Nonetheless, the energy dependence of D_{LL}^E during the main phase of the storm is in general weaker than the dependence on time or position. The same conclusion can also be made about D_{LL}^B; note however, unlike D_{LL}^E, D_{LL}^B is much larger in the main phase than in the recovery phase.

Overall, this demonstrates that during the March 17-18 storm the observed power spectral densities in the equatorial plane at THEMIS altitudes generate D_{LL}^E and D_{LL}^B coefficients that are largely coherent across different energies. This can be compared to the case of statistical Kp-dependent mod-

els for D_{LL}^{E} and D_{LL}^{B} derived from ULF wave power (e.g. *Ozeke et al.*, 2014) which are energy independent. Our observations show that some variation with energy remains but appears to be less influential than changes is time or position. However, as was mentioned above, the statistical estimates are not the good representation for the rates of radial diffusion, especially during the main phase.

In order to compare the event-specific and statistical rates of diffusion, Figure 3.7 shows the averaged diffusion coefficients $\langle D_{LL}^{B} \rangle$ and $\langle D_{LL}^{E} \rangle$ generated using THEMIS ULF wave fields and calculating the mean D_{LL} from Figures 3.5 and 3.6 for energies from 1 to 13 MeV, which corresponds to power spectral density from 1.2 to 20 mHz at THEMIS altitudes in the equatorial plane. The event-specific D_{LL} coefficients calculated using THEMIS data are shown with colored lines. The color scheme is the same as in Figures 3.5 and 3.6: red for THEMIS-A, green for THEMIS-E, and blue for THEMIS-D. Diffusion coefficients calculated from the *Ozeke et al.* (2014) statistics and which are energy (frequency) independent are shown with black lines. The top panel of Figure 3.7 shows averaged $\langle D_{LL}^{B} \rangle$ coefficients, the middle panel averaged $\langle D_{LL}^{E} \rangle$ coefficients, and the bottom panel shows the ratio of $\langle D_{LL}^{E} \rangle$ over $\langle D_{LL}^{B} \rangle$.

Immediately obvious in the Figure 3.7 is that the event-specific D_{LL}^{B} coefficients (Figure 3.7 top panel) appear to be larger than the *Ozeke et al.* (2014) coefficients by a factor of $\sim$10 during the main phase of the storm on March 17. However, during the recovery phase, towards the end of March 18, the THEMIS-derived magnetic diffusion coefficients D_{LL}^{B} approach those in the *Ozeke et al.* (2014) statistics. Figure 3.1 shows that the IMF is strongly southward during the main phase, meanwhile, it oscillates around zero during the recovery phase. Note that the *Ozeke et al.* (2014) statistics are derived using Kp and all geomagnetic, both storm and non-storm, conditions over a solar cycle. The existence of the strong southward IMF during the main phase of this intense storm may change the Kp-dependence of the ULF wave power, resulting in the failure of *Ozeke et al.* (2014) statistical approach to accurately specify storm-time D_{LL}^{B} coefficients during the main phase of the storm. At the same time, the electric diffusion coefficients (Figure 3.7 middle panel) are

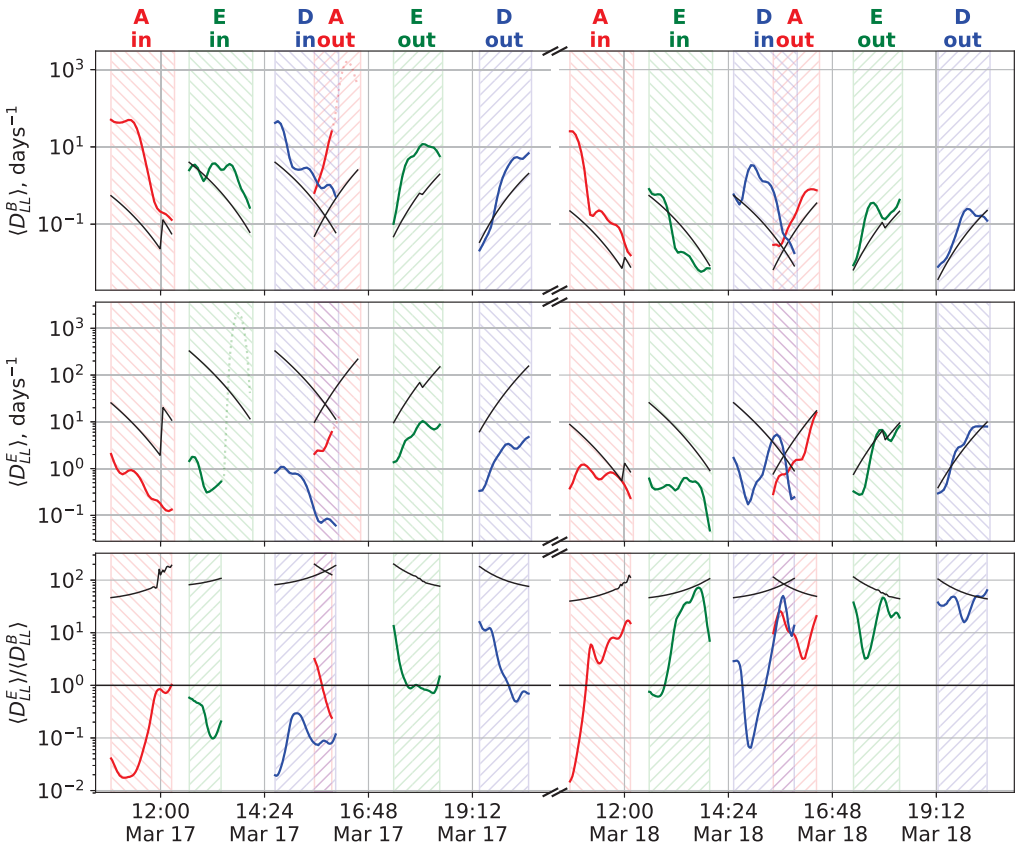

Figure 3.7: Radial diffusion coefficients and their ratio, calculated using local fields data from the THEMIS-A, -D, and -E satellites during the March 17-18, 2015 storm. The color scheme indicating data from each of THEMIS-A, -D, and -E satellites is the same as in Figure 3.4. The top panel shows D_{LL}^B, the middle panel D_{LL}^E, and the bottom panel shows the ratio of D_{LL}^E/D_{LL}^B. In each panel, we additionally show the *Ozeke et al.* (2014) statistical diffusion coefficients expressed as a function of the Kp at the time and L-shells of the THEMIS observations.

smaller than the *Ozeke et al.* (2014) statistics during the main phase of the storm but return to good agreement with the statistical model later during the recovery phase. Moreover, the bottom panel of Figure 3.7 shows that during the main phase of the storm on March 17 the D_{LL}^B coefficients exceed D_{LL}^E by a factor of $\sim$10. Meanwhile, the *Ozeke et al.* (2014) statistics predict the opposite relationship – that the D_{LL}^E coefficients should be larger than the D_{LL}^B coefficients almost by a factor of 100.

In the analysis of storm- and non-storm-time ULF wave power, *Dimitrakoudis et al.* (2015) showed that the effects of storm dynamics can significantly change the relationships of ULF wave power to Kp or compared to average, derived across the solar cycle. Similarly, for the October 2012 storm *Pokhotelov et al.* (2016) showed that main phase ULF wave power, especially as relates to compressional disturbances and D_{LL}^{B}, can be significantly enhanced as compared to non-storm times. The event-specific results presented in this chapter are consistent with these previous studies, and indicate in particular that the rates of radial diffusion during the main phase of the storms may differ significantly from other times. As a result, Kp-dependent empirical specifications of radial diffusion coefficients should be used with care, especially during storm main phase – and radial transport such as to a compressed magnetopause might be incorrectly represented using empirical Kp-dependent model during these times.

3.2.2 D_{LL}^{B} from GOES satellites

Analogous to the analysis of the THEMIS data presented in the previous section, we show spectrograms of ULF perturbations in the compressional component of the magnetic field measured by GOES-13 and GOES-15 satellites in Figure 3.8. Similar to the THEMIS data analysis, we ignore periods when the satellites are inside the magnetosheath and where very large $P^B > 10^2$ nT^2/mHz of the magnetosheath turbulence across the whole frequency range are present in the spectrograms during these times. For GOES-13 (top panel of Figure 3.8) the spacecraft is in the sheath across a large fraction of the orbit on the dayside between 13:00 UT and 18:00 UT on March 17. Meanwhile, for GOES-15 (bottom panel of Figure 3.8) the region when the spacecraft is in the sheath spreads from 15:00 UT until 18:00 UT on March 17. These regions are not shown and marked as "Magnetosheath" in the subsequent GOES plots in this chapter.

The region of relatively broadband waves with large P^B is present across the Pc4-Pc5 frequency range during the main phase of the storm, especially when there is a strong southward IMF. Figure 3.1 shows that there are two

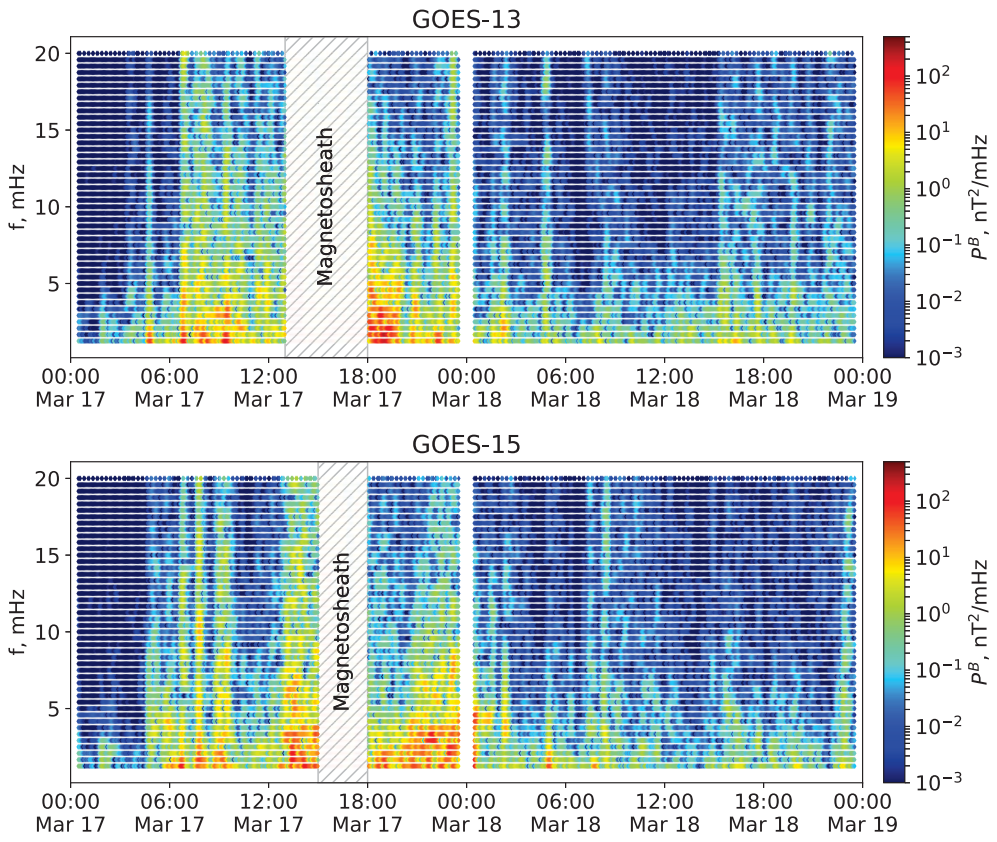

Figure 3.8: Spectrogram of ULF waves in the compressional component of the magnetic field as measured by the GOES-13 (top panel) and GOES-15 (bottom panel) spacecraft at geosynchronous orbit. Shaded regions indicate periods when GOES is in the magnetosheath (see text for details).

time periods when the IMF has a large southward component, in particular from 05:00 UT until 08:45 UT and from 12:00 UT until 24:00 UT on March 17. These times correspond to times of large compressional, broadband wave spectra in P^B when a wave power of $\gtrsim$1 nT^2/mHz is present at GOES-15 for frequencies $>$ 5 mHz. The same characteristics are present for the GOES-13 data but are partially obscured by the magnetopause crossing. Additionally, the power spectral densities at both GOES-13 and -15 subside to lower power levels during the recovery phase on March 18 when the B_z component of the IMF is small and fluctuates around zero.

Figure 3.9 shows D_{LL}^B coefficients as a function of drift (m=1) resonant particle energy and time for GOES-13 (top panel) and GOES-15 (bottom panel) derived from the compressional power spectral densities from 1.2 to 20 mHz

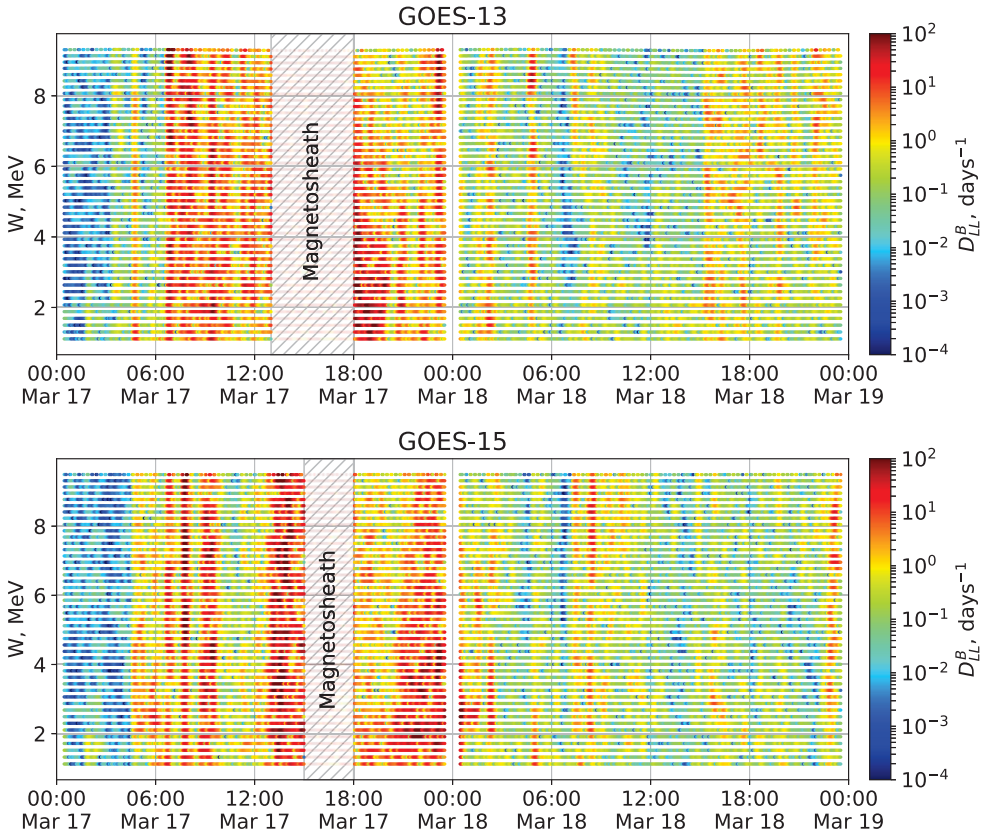

Figure 3.9: Diffusion coefficient D_{LL}^B as a function of time and drift (m=1) resonating electron energy as calculated using the *Fei et al.* (2006) formulas using the observed compressional ULF wave power from Figure 3.8 for the GOES-13 (top panel) and GOES-15 (bottom panel) satellites.

shown in Figure 3.8. Similar to the analysis of the THEMIS data, GOES D_{LL}^B as a function of energy is calculated using the same frequency range as in Figure 3.8. Figure 3.9 shows that the D_{LL}^B coefficients at geostationary orbit again show a strong energy coherence. However, there are some limited time intervals during the recovery phase when D_{LL}^B is more enhanced at particular energies. Overall, the D_{LL}^B coefficients at GOES appear to be even more energy independent than indicated in THEMIS data. Note that the regions when the GOES satellites are in the magnetosheath are again not shown in the plots. Moreover, even when the IMF turns southward and a broad power spectral density is observed for high frequencies (f>5 mHz), the proportionality of $P^B \propto f^{-2}$ stays valid largely delivering an energy independence consistent with the Kp-dependent empirical statistical models. Further anal-

ysis of the average values of the D_{LL}^{B} coefficients is presented in the Discussion and Conclusion section of this chapter, where a comparison to the equatorial D_{LL}^{E} derived from ground-based magnetometer data is presented.

3.2.3 Equatorial D_{LL}^{E} derived from ground-based magnetometer data

We obtain the quasi-azimuthal component of the electric field E_{ϕ} in the equatorial plane by mapping the D-component magnetic field measurements from selected ground-based magnetometers near the magnetic footprint of the GOES satellites. In this study, we use a magnetometer in Inukjuak (INUK) to map to E_{ϕ} near GOES-13. We use the *Tsyganenko and Sitnov* (2005) magnetic field model to determine that the INUK magnetometer from the AUTUMNX chain (*Connors et al.*, 2016) is close to the footprint of the GOES-13 magnetic field line during March 17-18, 2015. Similarly, we used the Fort Smith magnetometer (FSMI) from the CARISMA array (*Mann et al.*, 2008) for the determination of E_{ϕ} near GOES-15. The resulting spectrograms P^{E} as a function of frequency and time for both ground-based magnetometers are shown in the Figure 3.10. Meanwhile, the resulting D_{LL}^{E} as a function of electron energy and time are shown in Figure 3.11, where the top plot corresponds to the Inukjuak station (INUK) and the bottom plot corresponds to Fort Smith station (FSMI). D_{LL}^{E} in Figure 3.11 was derived using magnetometer D-component power spectral density for frequencies between 1.2 and 15 mHz, which correspond to electron energies from 1 to 7 MeV at geostationary orbit assuming drift (m=1) resonance. Even though during the main phase some energy dependence in D_{LL}^{E} was inferred using THEMIS data, an interesting observation is that the D_{LL}^{E} derived from the ground are more energy independent. A slight energy dependence is present for the D_{LL}^{E} from INUK during the recovery phase but this is not present for D_{LL}^{E} derived from FSMI data. Overall, D_{LL}^{E} derived from the ground-based magnetometer data show a relatively coherent behavior at different energies with much larger changes happening as a function of time.

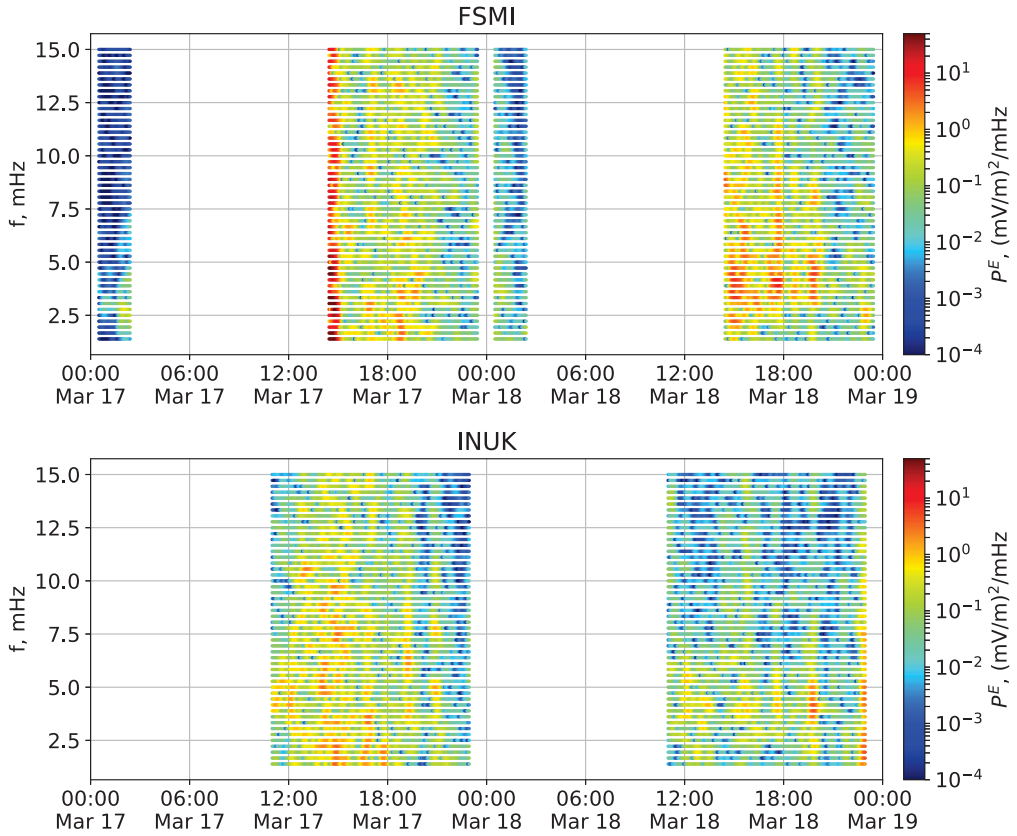

Figure 3.10: Spectrogram of ULF waves in the quasi-azimuthal component of the equatorial electric field as derived from a mapping of the D-component from the ground-based magnetometers at Fort Smith, (FSMI, top panel), and Inukjuak, (INUK, bottom panel).

3.3 Discussion and Conclusions

In the results presented here using in-situ THEMIS electric and magnetic field data, it was clear that during the main phase of the 17-18 March 2015 storm the data-derived D_{LL}^B and D_{LL}^E coefficients had very different behavior than predicted by, for example, the empirical Kp-dependent diffusion coefficient model by *Ozeke et al.* (2014). The *Ozeke et al.* (2014) statistics, using only Kp as a fitting parameter and using data from the entire solar cycle appears, at least for this storm, to significantly overestimate D_{LL}^E and underestimate D_{LL}^B during the main phase. Instead of D_{LL}^E being ∼100 times larger than D_{LL}^B, the THEMIS data imply that both diffusion coefficients are of the same magnitude, in agreement with prior results presented by *Pokhotelov et al.*

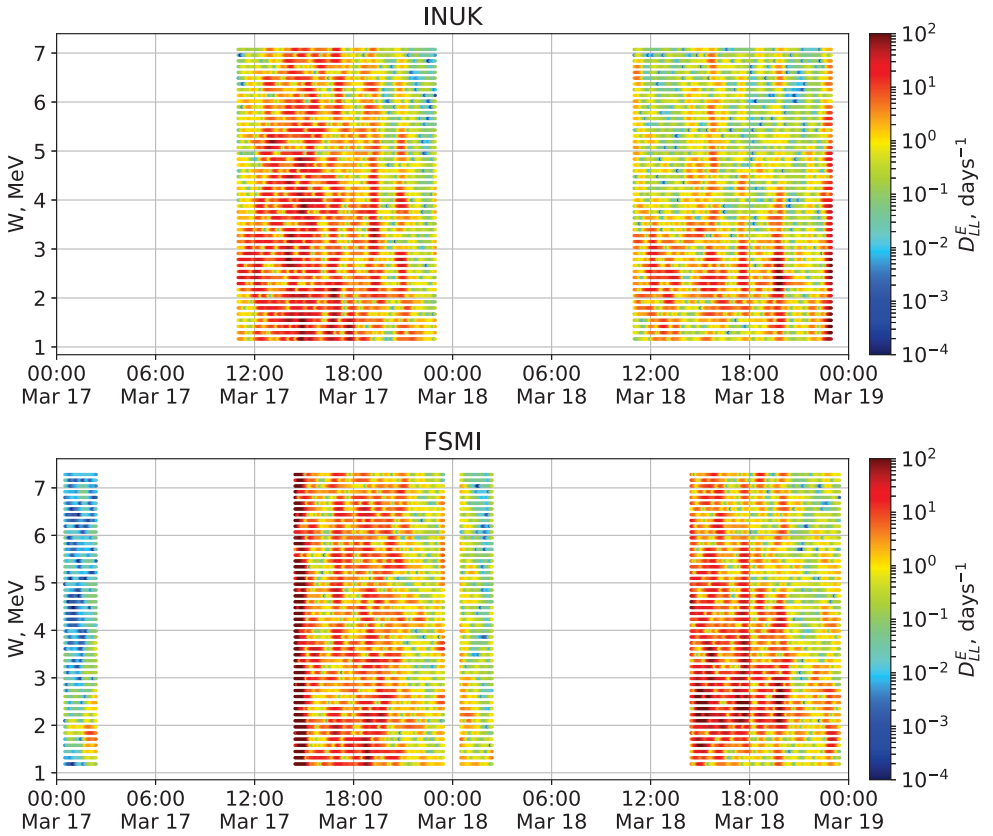

Figure 3.11: D_{LL}^E electric diffusion coefficient as a function of time and drift (m=1) resonant electron energy calculated using the *Fei et al.* (2006) formulas. The power spectral density of equatorial E_ϕ is obtained by mapping the D-component of the magnetic field on the ground to the equatorial plane using the *Ozeke et al.* (2009) technique. The top panel shows data corresponding to Inukjuak (INUK) magnetometer (close to magnetic conjugate to GOES-13), and the bottom panel shows data derived from for Fort Smith (FSMI) magnetometer (close to GOES-15).

(2016) using THEMIS and Van Allen Probes measurements for the October 2012 magnetic storm. To examine this relationship further, we also examine the relative magnitude of in-situ $\langle D_{LL}^B \rangle$ as derived from GOES magnetometer data and $\langle D_{LL}^E \rangle$ as derived by mapping data from magnetically conjugate ground-based magnetometers to the equatorial plane, proximal to the GOES satellites. Figure 3.12 shows a comparison between the average radial diffusion coefficients $\langle D_{LL}^B \rangle$ derived from GOES-13 magnetometer, corresponding $\langle D_{LL}^E \rangle$ derived from the INUK ground-based magnetometer, and the *Ozeke et al.* (2014) statistics on the geosynchronous orbit. Figure 3.13 shows the

same comparison between these diffusion coefficients at geosynchronous orbit near GOES-15.

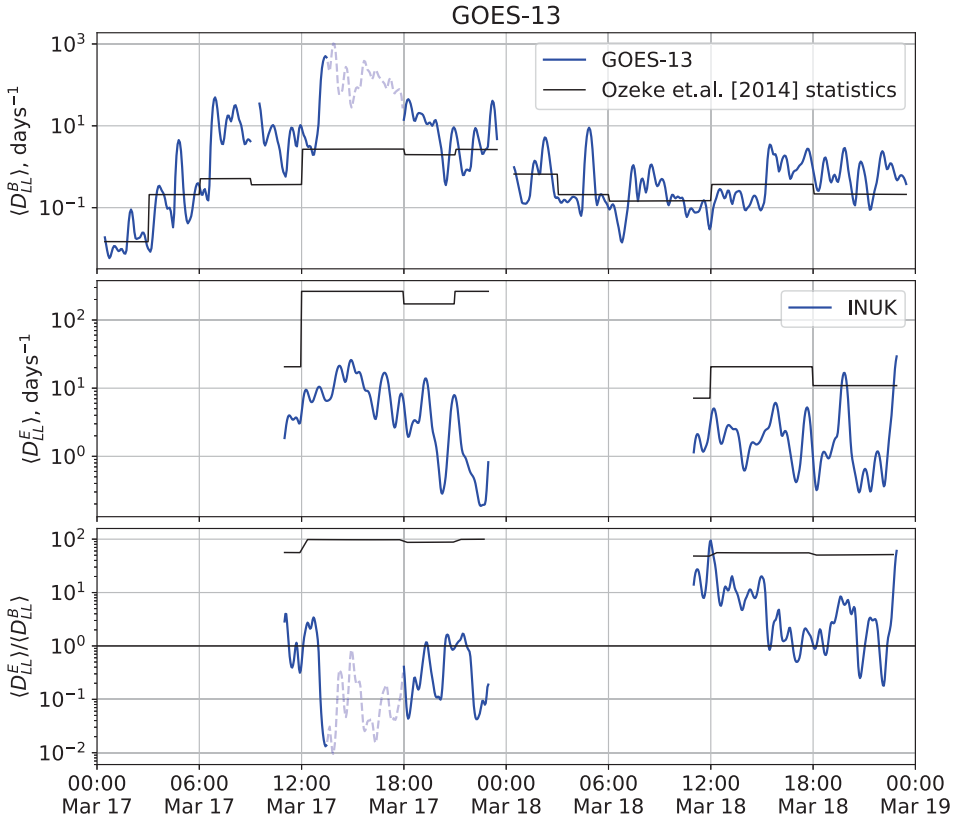

Figure 3.12: Comparison of various radial diffusion coefficients for March 17-18, 2015 storm at the locations of the GOES-13 satellite. In the top panel, the blue line represents $\langle D_{LL}^B \rangle$ data obtained using in-situ GOES-13 magnetic observations, meanwhile the black line represents the (event independent) D_{LL}^B from the *Ozeke et al.* (2014) Kp statistics. The middle panel shows the average $\langle D_{LL}^E \rangle$ coefficient in blue obtained by mapping the D-component ULF wave power from the Inakjuak ground-based magnetometer to the equatorial plane, and the *Ozeke et al.* (2014) Kp-dependent statistical model in black. The bottom panel shows the ratio of $\langle D_{LL}^E \rangle$ and $\langle D_{LL}^B \rangle$ for both observational (blue) and *Ozeke et al.* (2014) Kp-dependent empirical model (black). See text for more details.

Consistent with the results from the THEMIS satellites (Figure 3.7), the radial diffusion coefficients at geosynchronous orbit show the same discrepancy between storm specific and statistically expected D_{LL} values during the

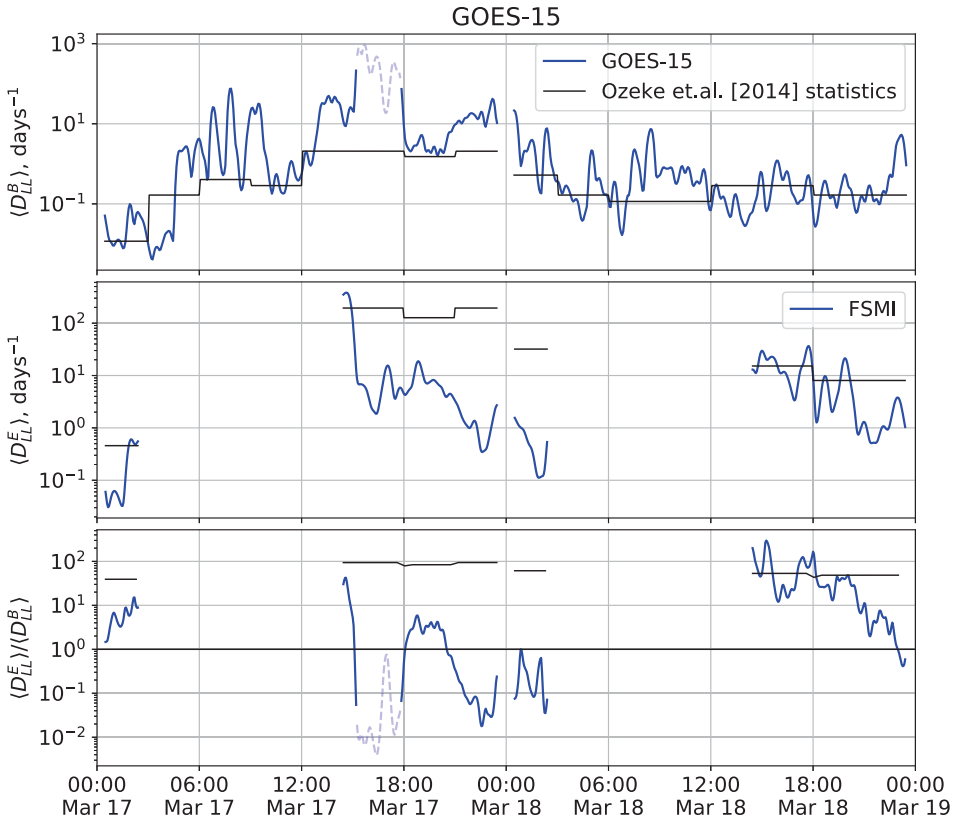

Figure 3.13: Comparison of the radial diffusion coefficients for data from GOES-15 satellite and Fort Smith ground-based magnetometer during March 17-18, 2015 storm. The same format as Figure 3.12.

main phase of the storm. In particular, the D_{LL}^B coefficients from the in-situ GOES measurements are larger than those predicted by the *Ozeke et al.* (2014) Kp-parameterization by almost a factor of 100 during the main phase of the storm (top panels of Figures 3.12 and 3.13). Meanwhile, the mapped D_{LL}^E coefficients derived from the ground-based magnetometer data are smaller than *Ozeke et al.* (2014) statistics (middle panels of Figures 3.12 and 3.13). Also consistent with the in-situ THEMIS data, during the main phase of the storm, the D_{LL}^B coefficients are of the same order of magnitude as D_{LL}^E. Therefore, the *Ozeke et al.* (2014) Kp-parameterization underestimates the relative importance of the D_{LL}^B coefficient (black lines in the bottom panels of Figures 3.7,

3.12, and 3.13) during the main phase. Hence, use of the *Ozeke et al.* (2014) Kp-parameterization in a radial diffusion simulation may lead to an underestimation of the total radial transport during the main phase by a factor of 2 or more. Note, however, that the storm-specific data-derived D_{LL}^{E}, D_{LL}^{B}, and their ratio are the same as predicted by the *Ozeke et al.* (2014) parametrization during the recovery phase on March 18, 2015.

It is also worthwhile to compare the results presented in this chapter with similar studies of other magnetic storms and other prior approaches used to study the 17-18 March 2015 event. In particular, it is interesting to compare our calculations of power spectral densities with the results reported by *Li et al.* (2016, 2017). In their studies, Li et al. used the Lyon-Fedder-Mobarry (LFM) magnetohydrodynamic model to examine ULF perturbations in the magnetosphere and adapted the *Fei et al.* (2006) analytic approach to calculate the radial diffusion coefficients in the simulation during the 17-18 March 2015 magnetic storm. Figure 5 of *Li et al.* (2016) shows spectrograms of P^E (their "E_Φ power") and P^B (their "B_Z power") as functions of frequency f and azimuthal wave number, m, during the pre-storm and the main phase of the storm. Their LFM simulation showed that the power stored in perturbations with $m = 1$ is dominant and larger than for waves with $m \geq 2$ by more than two orders of magnitude. This result validates our approach of assuming m=1 in this thesis. Note, however, that especially during periods where the m=1 assumption is violated our results may represent an estimation of a lower threshold of the storm specific radial diffusion coefficients.

According to the GOES data presented in our Figure 3.8, the bandwidth of compressional power spectral density is larger than that reported by *Li et al.* (2016) in their simulation during the main phase of the storm at 12:30 UT. GOES measurements show that the discrepancy between P^B at 1 mHz and P^B at 8 mHz is 1 order of magnitude. Meanwhile, the simulation by *Li et al.* (2016) shows a difference of almost 5 orders of magnitude. Similar broadband wave was observed on THEMIS-E inbound pass in Figure 3.4 at around the same time. However, during the recovery phase where the IMF $B_z \approx 0$ nT, the observed compressional wave power narrows and resembles results in *Li*

et al. (2016) for the pre-storm phase. This shows that the LFM model, at least in the resolution reported by *Li et al.* (2016), underestimates compressional power spectral density during the period of the strong southward IMF in the main phase. However, the same slight frequency dependence of P^E is observed in our analysis and the Li et al. simulations for m=1 during the main phase of the storm.

Additionally, *Li et al.* (2016) performed calculation of the D_{LL}^B and D_{LL}^E coefficients for electrons with different first adiabatic invariants in their Figure 6. The Li et al. results show that the magnetic radial diffusion coefficients in their simulations are independent of the first adiabatic invariant – a result consistent with the strong energy coherence of magnetic diffusion reported in this chapter. Meanwhile, Li et al. report a slight energy dependence of the electric diffusion coefficients during the main phase of the storm which disappears when IMF $B_z \approx 0$ nT. Note that in our analysis of THEMIS data, which relies on the assumption that $m = 1$ rather than a spectrum of multiple m's considered by Li et al., the energy dependence of D_{LL}^E in the main phase is somewhat larger than reported by *Li et al.* (2016). Nonetheless, this energy dependence remains weaker than the time dependence, as was described above.

However, as in the *Ozeke et al.* (2014) Kp-dependent statistical model the D_{LL}^E remain larger than D_{LL}^B by 2 or 3 orders of magnitude in *Li et al.* (2016) simulations, depending on storm phase. In contrast, the D_{LL}^B obtained from THEMIS measurements in this chapter are either larger than, or have the same magnitude as, D_{LL}^E during the main phase of the storm. A comparison of the in-situ D_{LL}^B derived data from GOES satellites at geosynchronous orbit, and D_{LL}^E derived from ground-based magnetometer data, show the same behavior. Note that during the main phase of the storm on March 17, $D_{LL}^B \approx 10^1$ days^{-1} at geosynchronous orbit according to our GOES data-driven calculations. Meanwhile, the LFM model estimates $D_{LL}^B \approx 10^{-2}$ days^{-1}. Overall, this further suggests that there are magnetospheric processes which are active in the main phase of intense geomagnetic storms during periods of strongly southward IMF, and which produce large in-situ compressional ULF

fields as observed here in THEMIS and GOES satellite data. However, such processes may not be well-represented in current MHD models such as LFM.

Analysis of in-situ THEMIS data (Figure 3.7) shows estimate of D_{LL}^{B} within range from 10^{0} days^{-1} to 10^{1} days^{-1} depending on L-shell, whilst D_{LL}^{E} is between 10^{-1} days^{-1} and 10^{0} days^{-1}, during the main phase of the storm. Therefore, according to the in-situ THEMIS data, magnetic (D_{LL}^{B}) diffusion may dominate an electric diffusion (D_{LL}^{E}) during the storm main phase. The same is also true for the geostationary orbit when comparing data obtained in-situ from the GOES satellites, and derived from ground-based magnetometer data (Figure 3.12 and 3.13). Meanwhile, the Kp-dependent *Ozeke et al.* (2014) model show an opposite picture with $D_{LL}^{B} << D_{LL}^{E}$. Note that the storm specific D_{LL} coefficients reverse their ratio and are well-repeated by the *Ozeke et al.* (2014) Kp-parametrization during the recovery phase at least on 18 March during this storm. These results show that the *Ozeke et al.* (2014) parametrization may fail to accurately describe the D_{LL} coefficients during storm main phase especially during intervals with a strong southward IMF component ($B_z \approx -20$ nT).

Overall, ULF waves in the Pc4-Pc5 band, resulting in $D_{LL} \sim 10^{1}$ days^{-1}, i.e., characteristic diffusion time $\tau = D_{LL}^{-1} = 2.5$ hours, provides means of rapid outward particle radial transport during the March 2015 geomagnetic storm. This provides a compelling potential mechanism for depleting electron outer radiation belt by transporting charged particles to the magnetopause. *Olifer et al.* (2018b), i.e., the analysis in Chapter 5 of this thesis, showed that transport to the outer boundary can be examined in the context of an analysis of the dynamics of the last closed drift shell (LCDS). According to the analysis presented by *Olifer et al.* (2018b), during the main phase of the storm on March 17, 2015 the separation in L^* the LCDS and the heart of the radiation belt may only be around L^*=1 (see Figure 3 of *Olifer et al.* (2018b)). According to the radial diffusion paradigm, such a separation can be easily bridged by fast outward radial diffusion. Additionally, in this chapter, we demonstrate that the storm specific radial diffusion coefficients may be largely energy independent. This agrees nicely with the results of *Olifer et al.* (2018b)

(e.g., their Figure S2 in the supplementary material) where it was shown that the loss patterns and LCDS dynamics are not only closely related, but also similar across a wide range of energies during the March 2015 storm.

As mentioned above, it is interesting to compare our results with those of *Pokhotelov et al.* (2016) where a similar analysis of D_{LL} coefficients was performed for the 8-9 October 2012 geomagnetic storm using THEMIS and Van Allen Probes data. Pokhotelov et al. report similar features whereby the radial diffusion coefficients demonstrate the characteristics that $D_{LL}^{B} \sim D_{LL}^{E}$ during the main phase of that storm and with a similar southward IMF ($B_z \approx -15$ nT). In the *Pokhotelov et al.* (2016) results, the Kp-dependent model overestimates D_{LL}^{E} by orders of magnitude as compared to the observations. Meanwhile, the event-specific D_{LL}^{B} is being underestimated by the Kp-parametrization in the statistical models by a factor of $\sim$4. The behavior of the electric diffusion coefficient is similar to that which we report in this chapter for the March 17-18, 2015 storm. However, the level of disagreement between data-driven and statistical D_{LL}^{B} is much higher for this event. One difference between the October 2012 storm and the March 2015 event studied here is that the latter was much more intense in terms of ring current dynamics with SYM-H index reaching -225 nT as compared to -120 nT during the October 2012 storm. In addition, the March 2015 storm has more strongly southward IMF conditions ($B_z \approx -20$ nT) than observed during the October 2012 storm ($B_z \approx -15$ nT). If the strong compressional disturbances observed during the March 2015 storm are driven by processes associated with strongly southward IMF then this might explain the discrepancy. Consistent with this hypothesis, very recent analysis of 15 years of ground-based magnetometer data by *Bentley et al.* (2018) showed a strong connection between enhanced ULF wave power and the magnitude of the southward component of the IMF. For example, their Figure 6 shows that the well-known increase of ULF wave power with increasing solar wind speed is significantly further enhanced by increasingly negative B_z.

In summary, and overall, our analysis of data-driven radial diffusion coefficients shows that the relative magnitudes of D_{LL}^{E} and D_{LL}^{B} may be significantly

different during storm main phase than at other times. For example, using in-situ THEMIS and GOES data we show that during the main phase of the intense March 2015 storm the radial diffusion coefficients are not well-described by the *Ozeke et al.* (2014) empirical Kp-dependent statistical model. Firstly, the D_{LL}^{B} coefficient is underestimated by the Kp-parametrization. Secondly, the solar cycle derived Kp-statistics imply that the D_{LL}^{B} should be negligibly small in comparison to D_{LL}^{E}. However, during the main phase of the March 2015 storm, the event-specific results show different behavior with $D_{LL}^{E} \lesssim D_{LL}^{B}$. Thus, using the *Ozeke et al.* (2014) parametrization to represent the diffusion coefficients for radial diffusion simulations may lead to underestimation of the total D_{LL} coefficient during the main phase. This suggests that there is an urgent need to produce new statistical models for D_{LL} coefficients during the main phase of a storm, perhaps including the influence of processes active during southward IMF. Providing more accurate radial transport models, especially for example during intense radiation belt extinction events (e.g., *Ozeke et al.*, 2017; *Olifer et al.*, 2018b) may help to improve the accuracy of the magnetopause shadowing losses predicted by radial diffusion models. Understanding the relative contributions of fast outward radial diffusion to the last closed drift shell, and therefore magnetopause shadowing, and local wave-particle scattering losses to the atmosphere, remains a major challenge for improving the accuracy of the radiation belt modeling. Improved future characterizations of especially the compressional disturbances that increase main phase D_{LL}^{B} could help significantly in that regard.

Chapter 4

Magnetopause Shadowing During Intense Geomagnetic Storms

This chapter presents observations of very fast radiation belt loss as resolved using high time resolution electron flux data from the constellation of Global Positioning System (GPS) satellites. The timescale of these losses is revealed to be as short as $\sim 0.5 - 2$ hours during intense magnetic storms, with some storms demonstrating almost total loss on these timescales and which we characterize as radiation belt extinction. The intense March 2013 and March 2015 storms both show such fast extinction, with a rapid recovery, while the September 2014 storm shows fast extinction but no recovery for around two weeks. By contrast, the moderate September 2012 storm which generated a three radiation belt morphology shows a more gradual loss. The last closed drift shell (LCDS) was computed for each of these four storms and the results show a very strong correspondence between the LCDS and the loss patterns of trapped electrons in each storm. Most significantly, the location of the LCDS closely mirrors the high time resolution losses observed in GPS flux. The fast losses occur on a timescale shorter than the Van Allen Probes orbital period, are explained by proximity to the LCDS, and progress inward, consistent with outward transport to the LCDS by fast ULF wave radial diffusion. Expressing the location of the LCDS in L^*, and not model magnetopause standoff distance in units of R_E, clearly reveals magnetopause shadowing as the cause of

the fast loss observed by the GPS satellites.

Particularly, here we examine electron flux data from the Van Allen Probes together with that available from sensors on-board the GPS satellite constellation to examine the timescales of storm-time radiation belt loss. We compare the losses in the two intense March 2013 and March 2015 storms, as well during the extended depletion during the September 2014 storm (*Ozeke et al.*, 2017), and in the interval of loss associated with the generation of the third radiation belt morphology observed by *Baker et al.* (2013b) during the moderate September 2012 storm (see also *Mann et al.* (2016)). In order to probe such fast losses, electron flux data available from the constellation of GPS satellites has recently been released, offering high time resolution monitoring on hour timescales or less (*Morley et al.*, 2010a, 2016, 2017).

Note that the content of this Chapter have been already published in *Olifer et al.* (2018b), where I performed the data analysis and was in charge of composing the manuscript. Meanwhile, I.R. Mann and L.G. Ozeke were advisors in this project, and S.K. Morley helped with obtaining and interpretation of electron flux data from the GPS satellite constellation as well as provided full calculation of the LCDS for the March 2015 event.

4.1 Description of the Storms

A summary of the solar wind, resulting geomagnetic indices, and the resulting 2.6 MeV radiation belt flux response for the March 2013 are shown in figure 4.1, for the March 2015 in figure 3.1, for the September 2014 in figure 4.2, and for the September 2014 in figure 4.3. Solar wind data was taken from Operating Missions as a Node on the Internet (OMNI) database. Energetic particle data was taken from NASA's Van Allen Probes database for the Relativistic Electron-Proton Telescope (REPT) instrument (*Baker et al.*, 2013a). Figures 4.1, 3.1, and 4.2 show that in the first three events (March 2013, 2015, and September 2014) the radiation belt loss happened on a timescale which is too short to be fully resolved along the orbit of the Van Allen Probes mission, the orbital period being too long to provide an explicit picture of what hap-

pened. Thus in this chapter, we additionally focus on GPS satellite electron flux measurements from the Combined X-ray Dosimeter (CXD) (*Tuszewski et al.*, 2004; *Morley et al.*, 2010a, 2016). Combined data from $11 - 17$ satellites, depending on the year, delivers high (~ 30 minutes) temporal resolution and explicitly shows the dropout patterns even in fast loss events. Note that the GPS satellites have an orbital radius of 4.2 Earth radii, therefore the lowest McIlwain L-shell which can be observed by the constellation is $L = 4.2$. In this chapter, we attempt to explain the losses seen in those four storms by magnetopause shadowing. To confirm this hypothesis, we analyze how the last closed drift shell (LCDS) which we calculate as a function of L^* compares with the observed radiation belt dropout.

It is a known problem that the calculation of the LCDS is time and resource consuming. Usually, it is done using a method described in *Roederer* (1970). However, to speed up calculations, a neural network was created by training it on full calculations for different events (*Koller et al.*, 2009; *Yu et al.*, 2012). This software is a part of the LANL* project. All calculations of any L^* parameter (*Roederer*, 1970) in this chapter was done using TS04 *Tsyganenko and Sitnov* (2005) model. To be confident that the neural network returns reliable results we compare its output and the one obtained from the full calculation for the March 2013 event. This was done by using a variant of the *Roederer* (1970) method to find L^* for a given second adiabatic invariant K. In this study, we use the LANLGeoMag software library (*Henderson et al.*, 2017). It was also used in previous studies by *Spence et al.* (2013) and *Morley et al.* (2013). LCDS calculations using this approach were successfully performed by *Xiang et al.* (2017) for the 22-23 June 2015 event. As was shown for example by *Ukhorskiy et al.* (2011), the drift orbit of an electron can change significantly in the presence of off-equatorial magnetic field strength minima as a result of the development of Shebansky orbit (e.g., *McCollough et al.*, 2012). The existence of Shebansky orbit effects are not accounted for the standard prescriptions by *Roederer* (1970) for LCDS calculations. This effect is ignored in this study.

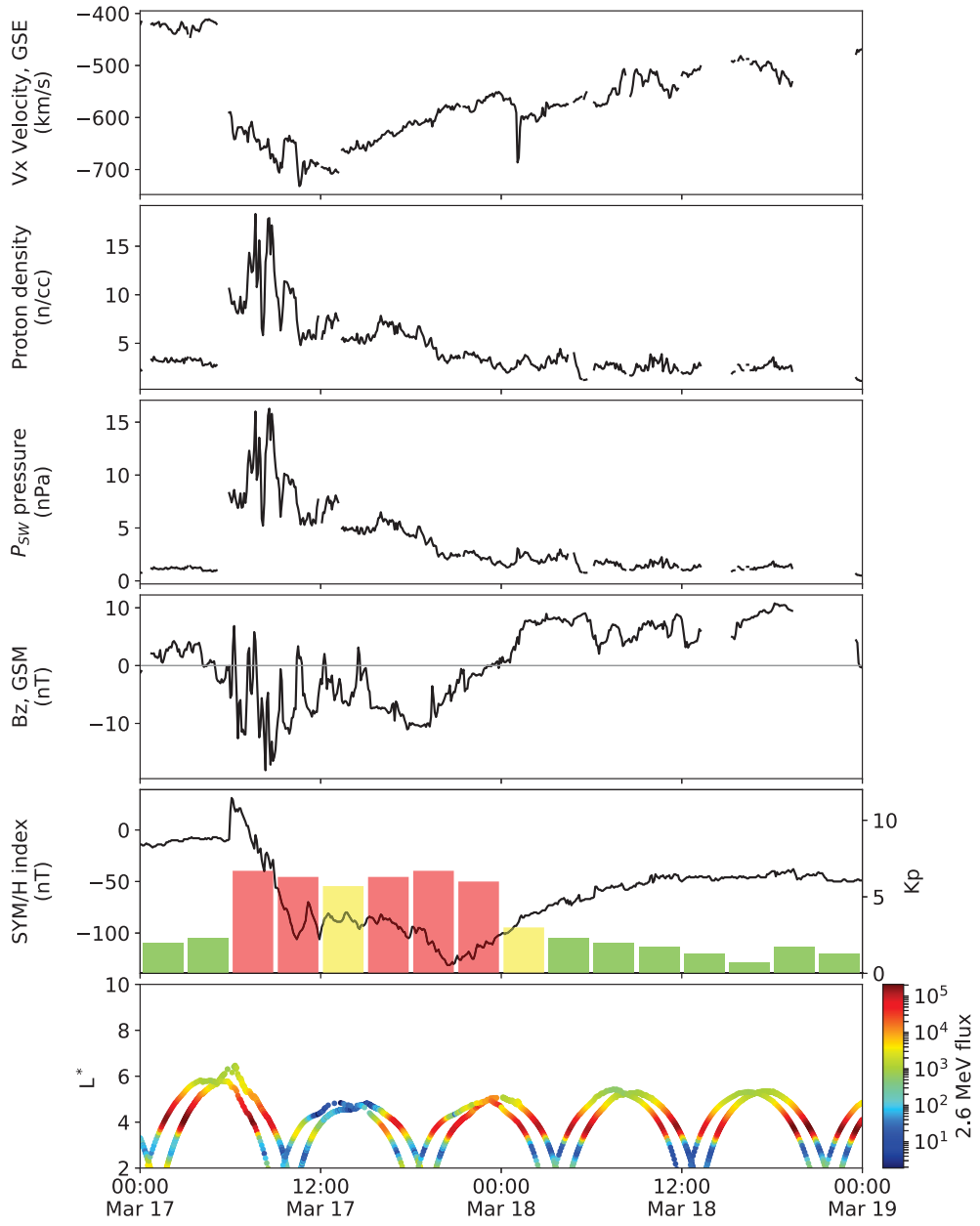

Figure 4.1: Summary of the solar wind, resulting geomagnetic indices, and 2.6 MeV radiation belt electron response for the March 2013 geomagnetic storm. From top to bottom for each storm: solar wind velocity x-component in GSE coordinates; proton density; solar wind dynamic pressure; z-component of the interplanetary magnetic field in GSM coordinates; geomagnetic SYM-H index as a line plot and Kp index as a bar plot; and 2.6 MeV electron differential flux measured by the REPT instrument on Van Allen Probes A and B as a function of L^* and time in $\mathrm{cm}^{-2}\mathrm{s}^{-1}\mathrm{sr}^{-1}\mathrm{MeV}^{-1}$.

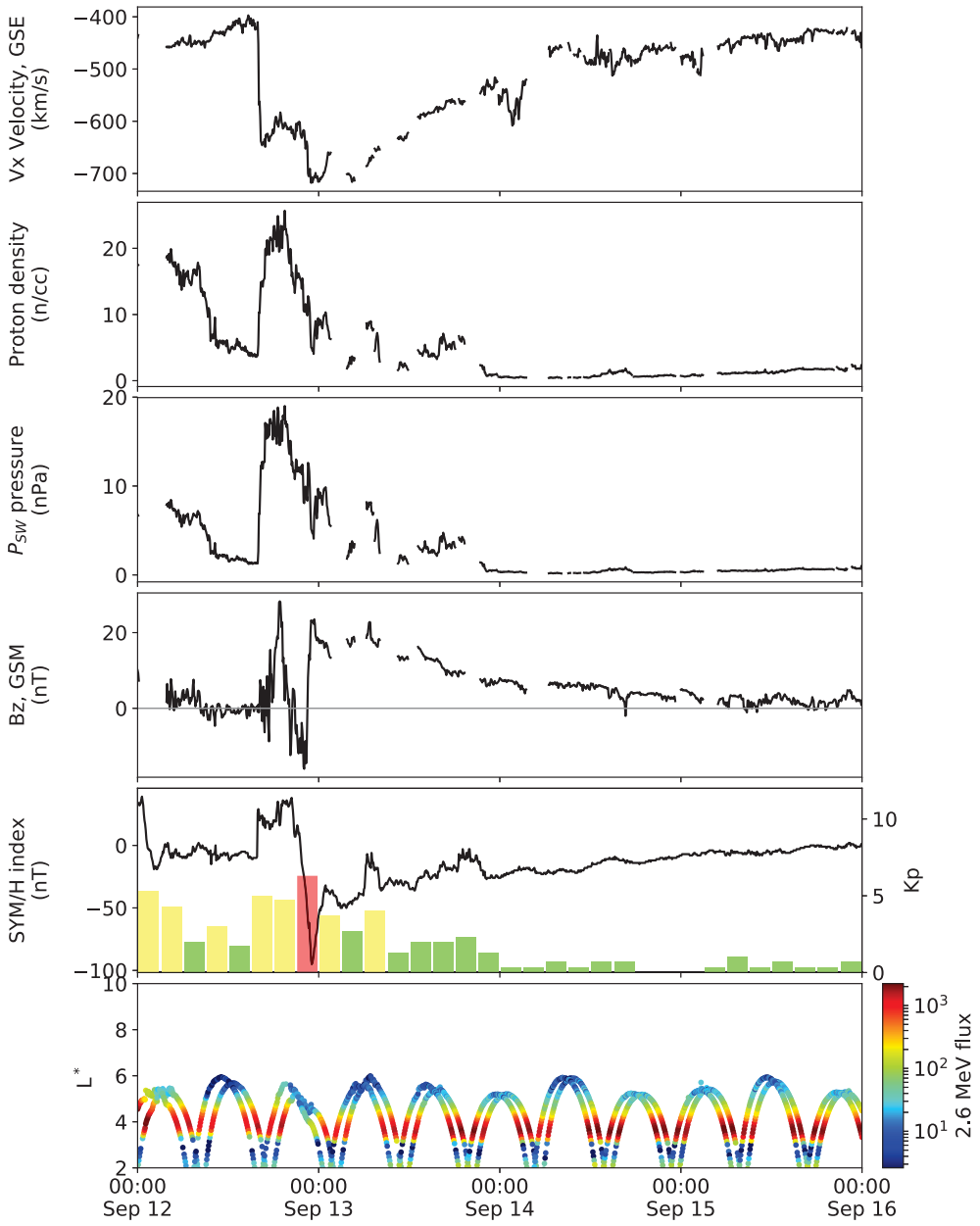

Figure 4.2: Summary of the solar wind, resulting geomagnetic indices, and 2.6 MeV radiation belt electron response for the September 2012 storm. Same format as figure 4.1.

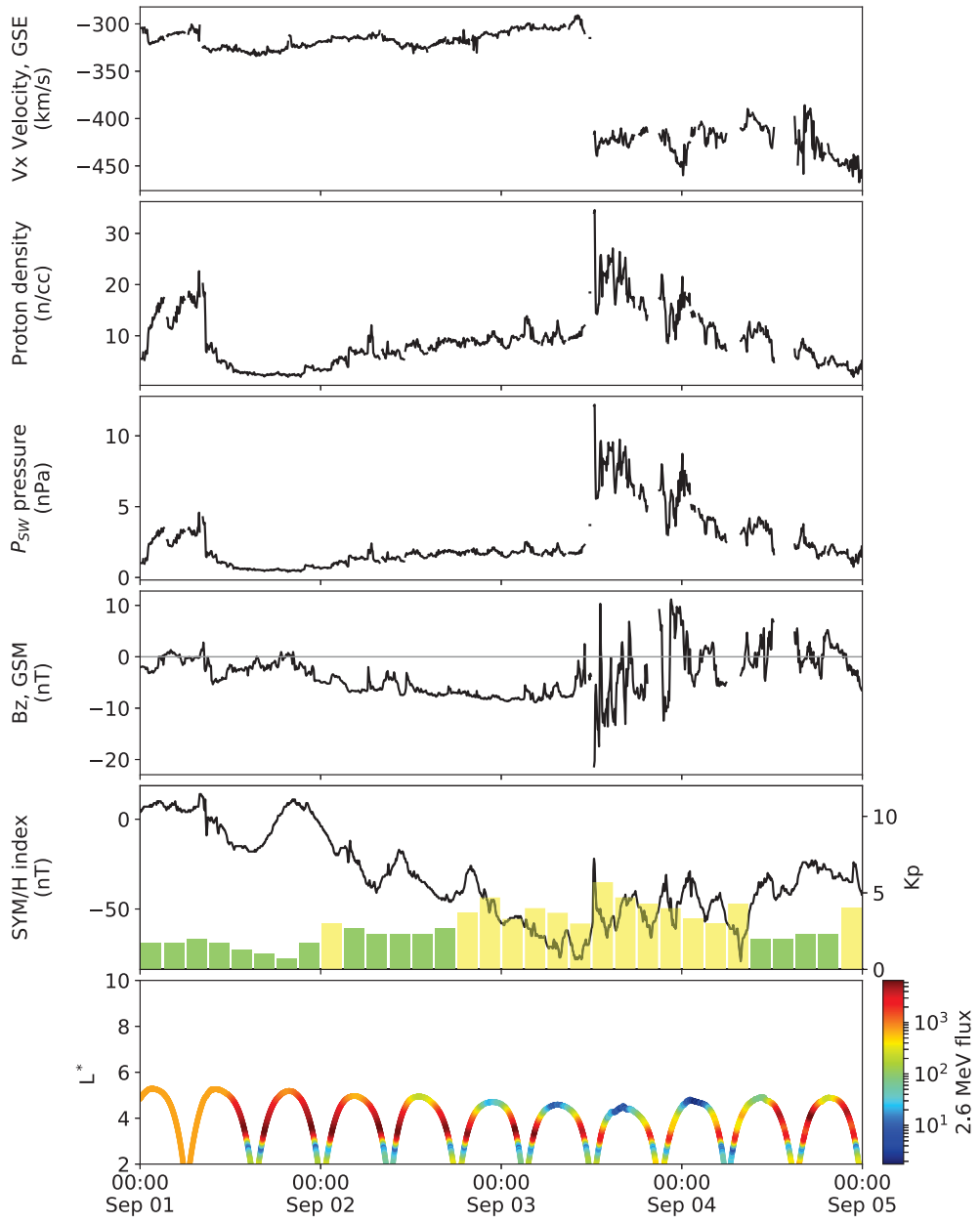

Figure 4.3: Summary of the solar wind, resulting geomagnetic indices, and 2.6 MeV radiation belt electron response for the September 2014 geomagnetic storm. Same format as figure 4.1.

4.2 Results

In this section, we show in-situ measurements of particle fluxes from the GPS constellation of satellites as a function of L^* and time as well as detailed data from the Van Allen Probes for the March 2013, March 2015, September 2012, and September 2014 storms. Additionally, in the GPS data plots we show the last closed drift shell (LCDS) as a function of L^* (left axis), calculated using LANL* neural network. The figures also show the magnetopause standoff distance in units of Earth radii (R_E), calculated using the *Shue et al.* (1998) model and plotted as a function of R_E on the right axis. We also overlay the data for the March 2013 event with the full calculation of the L^* of the LCDS for $K = 0.11\,\mathrm{R_E G^{1/2}}$, which corresponds to equatorial pitch angles of 50-55 deg in a magnetic dipole. This full LCDS calculation was done as a part of the Geospace Environment Modeling focus group "Quantitative Assessment of Radiation Belt Modeling" challenge (*Brito and Morley*, 2017).

4.2.1 March 2013 and March 2015 Storms

Figure 4.4 shows data from Van Allen Probes A and B for the March 2013 (left) and March 2015 (right) events where the top panels (a, d) show in- and out-bound passes as a function of L^* for both probes. The middle panels (b, e) show the observed flux of 2.6 MeV electrons. The bottom panels show two Van Allen Probe passes right before and right after the fast radiation belt extinction was observed for both storms. For example, in the March 2013 event Figure 4.4(c) shows the pre-depletion inbound pass of Probe A and the first post-depletion outbound pass of Probe B. The differences in fluxes between those passes is at one order of magnitude for both storms which suggests that the main loss in both of these storms happened with a timescale much shorter than the orbital period of the Van Allen Probes. Thus, we use the GPS constellation of satellites to obtain higher time resolution. We used 12 satellites for the March 2013 event and 17 satellites for the March 2015 event and the data is shown in Figure 4.5. Here we show the combined flux data for 3 MeV electrons as a function of L^* (left axis), the LCDS as a function of L^*

calculated using the LANL* neural network with red lines, and the full LCDS calculation for the March 2013 event with a blue line. The magnetopause position in units of Earth radii, R_E, was calculated using *Shue et al.* (1998) model is also shown with a green line on the right hand axis.

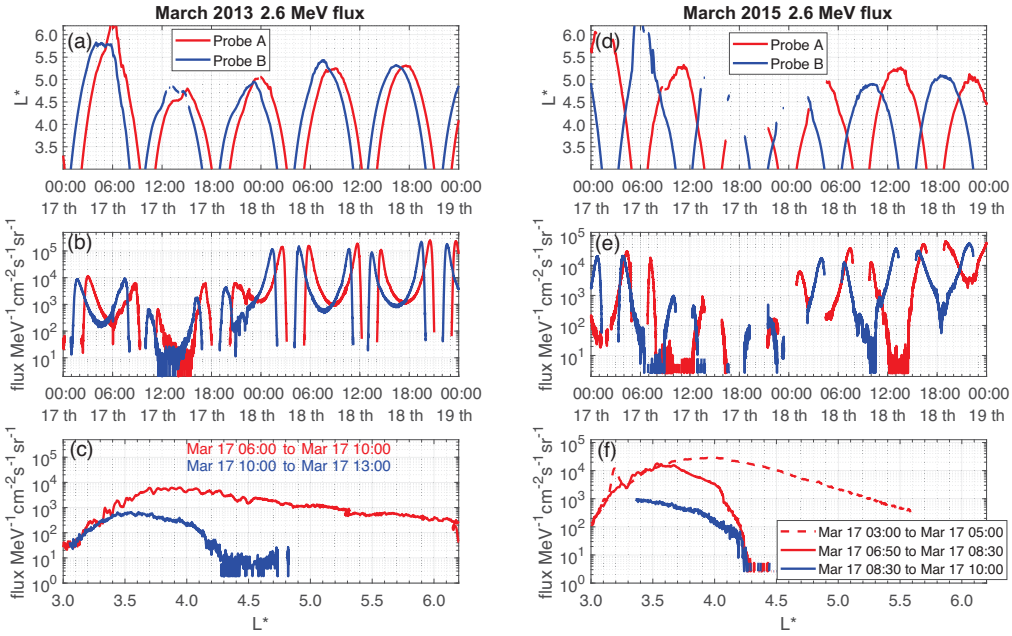

Figure 4.4: Summary of the Van Allen Probe A (red) and B (blue) data for the March 2013 and March 2015 storms: (top row) Van Allen Probes' L^*; (middle row) measured flux of 2.6 MeV electrons; (bottom row) L^* dependence of the flux during the fast loss. For the March 2013 storm we show the last inbound pass of Van Allen Probe A when the radiation belt is still present and the first outbound pass of Van Allen Probes B after the dropout happened. For the 2015 storm we show the last outbound pass of probe A when the radiation belt is still present and the first inbound pass of probe B after the dropout. With the red dashed line we show the flux measured by the in-bound pass of Probe A when the first solar wind shock arrived at around 04:40 UT, but no radiation belt loss had happened yet.

Apart from the clear correspondence between the LCDS and the flux data in Figure 4.5, we also note how well the neural network reproduces results from the full simulation for a moderately low second adiabatic invariant, K, for the March 2013 event (the top panel of Figure 4.5). We also note that the LCDS derived from the full calculations for different values of K are qualitatively similar and only show a small offset as a function of K. Based on this result,

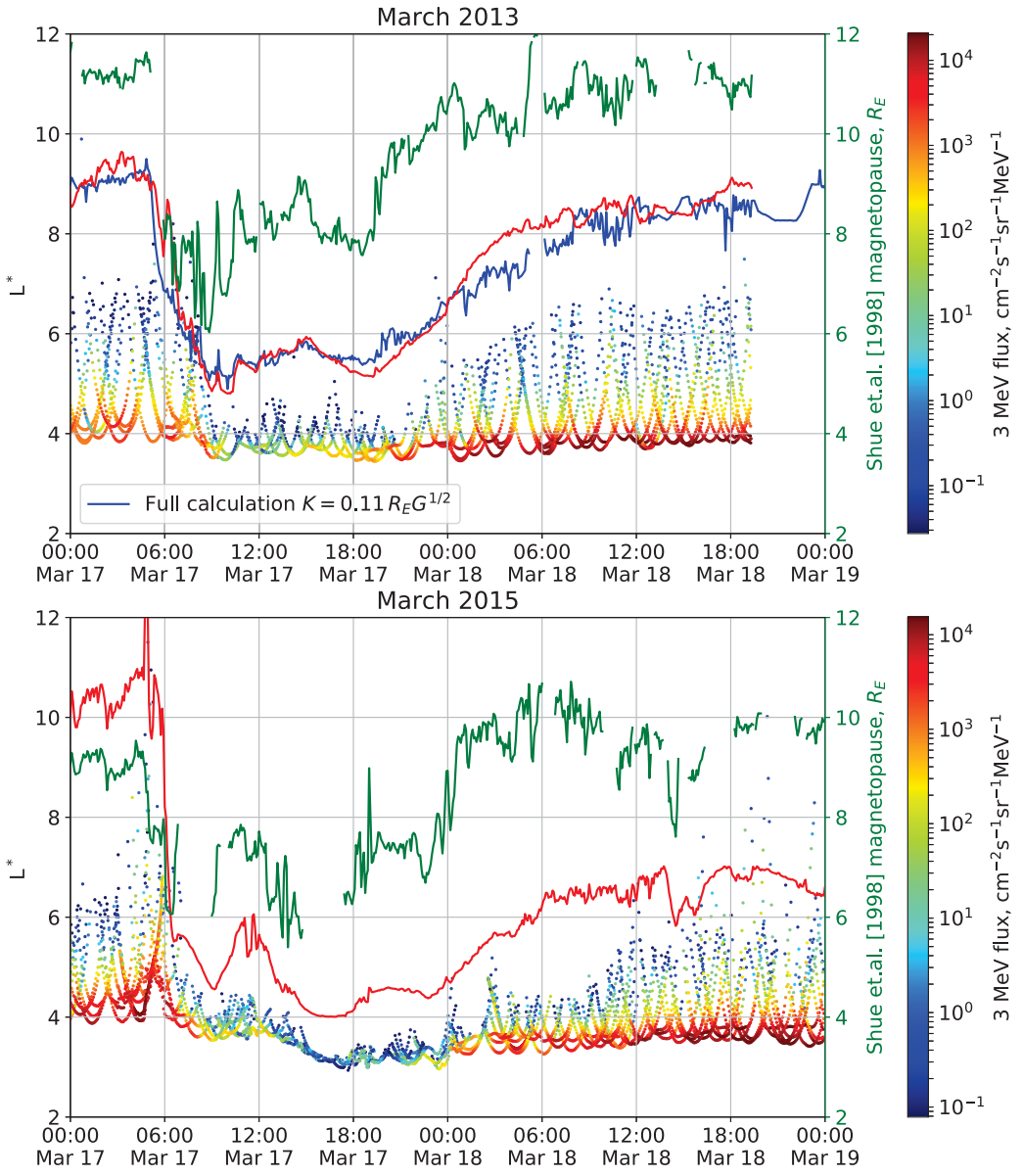

Figure 4.5: 3 MeV electron flux from the GPS constellation as a function of L^* (left axis) for the March 2013 and March 2015 storms. Last closed drift shell (LCDS) L^*, calculated using LANL* neural network, is shown with a red line. The magnetopause standoff distance in units of Earth radii, calculated using the *Shue et al.* (1998) model, is shown with a green line and should be read from the right hand axis. For the 2013 event we also show the full calculation for the L^* of the LCDS with a blue line (see text for details).

we are confident that the LANL* neural network LCDS calculation approach can give quite accurate results. For numerical efficiency, for the subsequent three storms we hence calculate the LCDS with the LANL* neural network approach. Note also that for the period around $5-6$ UT on March 18, 2013, there is a strong anomaly in the full LCDS calculation, and this interval is not plotted in Figure 4.5.

Figure 4.5 shows a remarkable high time resolution coherence between the location of the LCDS, its proximity to the Van Allen Belt, and the observed fast loss as characterized in GPS electron flux data. The strong correlation between measured flux and LCDS is present for both of these storms. They were so powerful, that the LCDS dropped down to $L^*\sim 5$ and $L^*\sim 4$ in 2013 and 2015, respectively, for a relatively long time of ~ 6 hours. For the March 2013 storm, the LCDS gradually moves inward following the storm commencement and significant belt losses are observed early in the main phase before the minimum in SYM-H. Losses are seen clearly in Van Allen Probe data (Figure 4.4) at $L^*= 4.5$ between around 08 UT and 12 UT, and at $L^*= 4$ between around 08:30 UT and 11 UT. The GPS data (Figure 4.5, top panel) reveals the spatio-temporal characteristics of this loss in much greater detail, with rapid loss occurring around 08-09 UT, and with losses moving inward deeper into the belt in concert with the inward motion of the LCDS from $L^*\sim 6$ to $L^*\sim 5$. Van Allen Probe data suggest that the losses have reached inside GPS orbit to at least $L^*\lesssim 3.5$ by ∼10:20 UT. For March 2013 there remains a separation between the LCDS and the L^* where the loss is observed since the LCDS does not drop below $L^*\sim 5$. However, in the presence of steep gradients in phase space density and strong storm main phase ULF wave power (*Dimitrakoudis et al.*, 2015; *Murphy et al.*, 2015) the timescales in the the modeling of *Mann and Ozeke* (2016) suggest that outward radial diffusion to the LCDS could be sufficient to explain the observed rapid losses and radiation belt extinction.

Arguably, the March 2015 event shows even faster loss. As described by *Baker et al.* (2016) and as can be seen from Figure 3.1, a solar wind shock arrives around 04:40 UT and the magnetopause position moves in by ≈ 2 L.

This shock arrival was discussed in detail by *Baker et al.* (2016) (their Figure 7) who emphasized the generation of drift echoes following the shock impact. However, the GPS data does not show any signs of loss until after 06:00 UT. This is the time that the IMF turns southward and the LCDS moves inward with the loss starts immediately after (Figure 3.1 top right plot). For the March 2013 event, which was discussed by *Baker et al.* (2014), the IMF turns southward almost immediately at storm onset which causes the LCDS and the magnetopause to move inward at the same time. This implies that the governing factor of the loss in both of these events is the location of the LCDS. Note however that it is crucial to take the LCDS location into consideration as a function of L^* rather than regarding the *Shue et al.* (1998) magnetopause location in units of Earth radii as being equivalent to the LCDS position in L^*.

Additionally to GPS flux data for 3 MeV electrons, we present data for a wider range of GPS energies. Figure 4.6 shows that similar dropouts also happened for different energy populations, and all of them follow the same trend as the LCDS. The fact that a wide range of energies show similar behavior is consistent with the response expected for magnetopause shadowing; but is most likely inconsistent with the hypothesis that plasma wave-particle scattering into the atmosphere was the dominant loss process. The very fast, $\lesssim$hour timescale, losses of at least an order of magnitude in flux revealed by the GPS satellites suggest that these losses might be described in terms of radiation belt extinction, consistent with the characteristics of the very fast losses reported by *Ozeke et al.* (2017) for the September 2014 storm. Energies vary from top to bottom as 1 MeV, 1.6 MeV, 2 MeV, 4 MeV, 5 MeV.

4.2.2 September 2014 and September 2012 Storms

Similar to the previous subsections we show the data from Van Allen Probes A and B for the September 2014 and September 2012 events in Figure 4.7. Figure 4.7(c) shows the last pre-depletion outbound pass of Probe A and the first post-depletion inbound pass of Probe B. As discussed by *Ozeke et al.* (2017) and shown in Figure 4.7 here, the loss in the September 2014 event

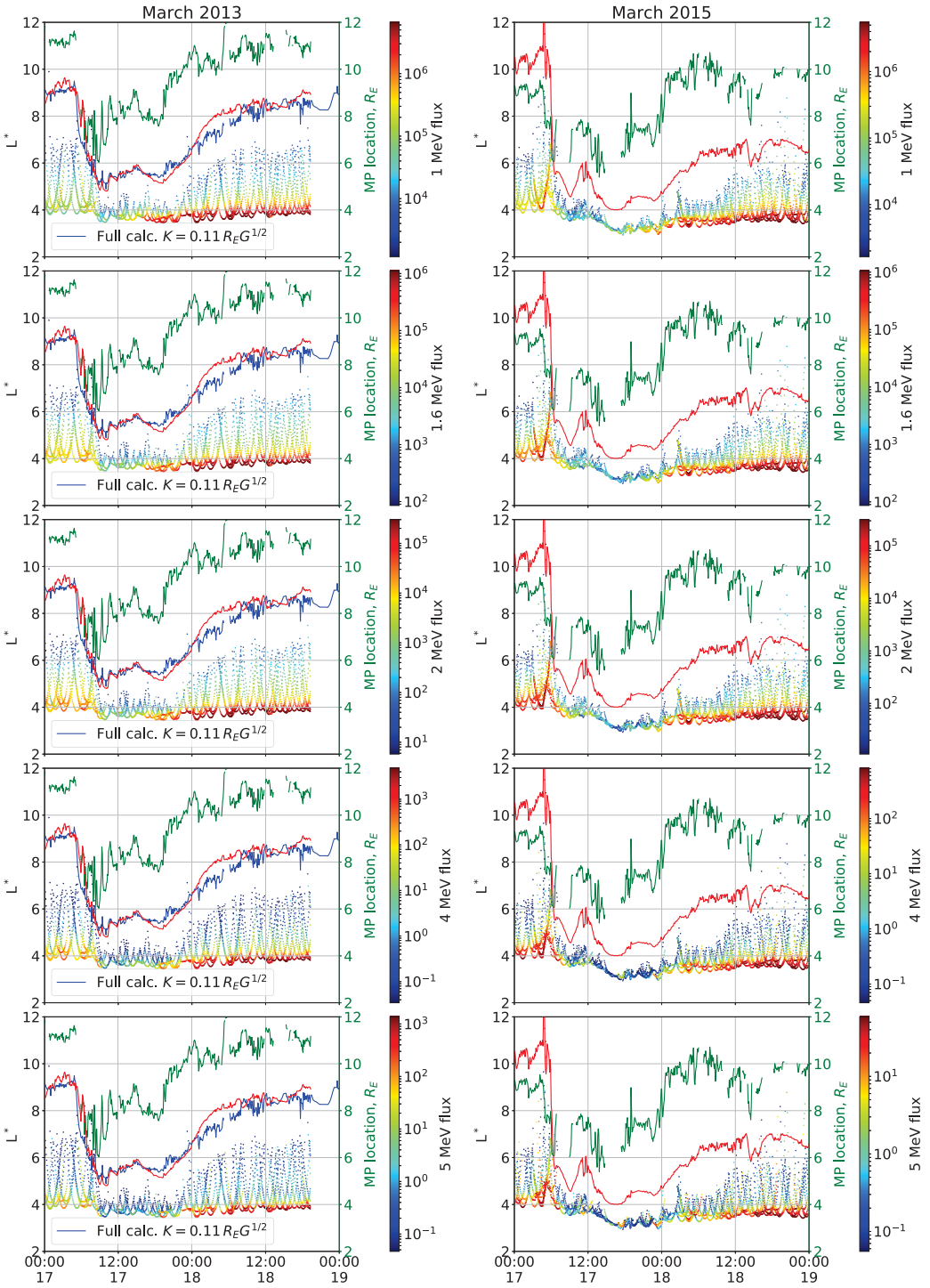

Figure 4.6: Energetic electron fluxes ($\mathrm{cm^{-2}s^{-1}sr^{-1}MeV^{-1}}$) from the GPS satellite constellation data for March 2013 and March 2015 events. Last closed drift shell position in units of L^*, calculated using the LANL* neural network, is shown with a red line. Magnetopause position, calculated using the *Shue et al.* (1998) model in units of R_E, is shown with a green line. For the March 2013 event we also show the full calculation of the LCDS at $K = 0.11\,\mathrm{R_E G^{1/2}}$ with a blue line.

(Figure 4.7(a-c)) can also be characterized in terms of radiation belt extinction. In contrast, losses in the September 2012 event (Figure 4.7(d-f)) are more gradual.

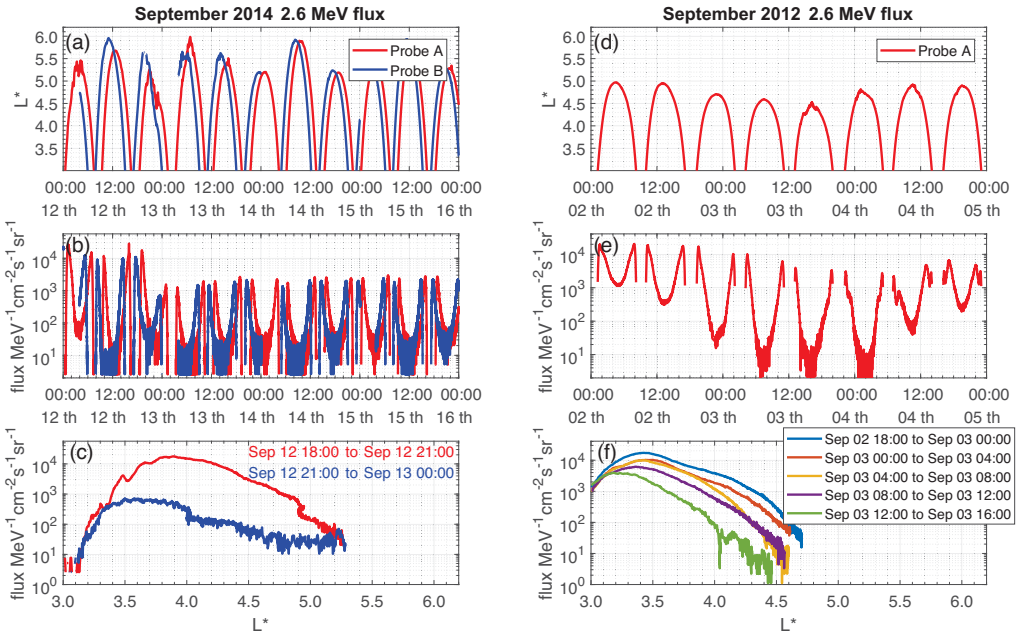

Figure 4.7: Summary of the Van Allen Probe A (red) and B (blue) data for the September 2014 and 2012 storms: (top row) Van Allen Probes' L^*; (middle row) measured flux of 2.6 MeV electrons; (bottom row) L^* dependence of the flux during the fast loss. For the September 2014 storm we show the last outbound pass of probe A when the radiation belt is still present and the first inbound pass of probe B after the dropout. For 2012 storm we show gradual loss with different colors, which happened through multiple orbits of Van Allen Probe A.

GPS data for the September 2014 and September 2012 storms is shown in Figure 4.8 in the same format as Figure 4.5. Note that here we analyze events not in chronological order since the loss characteristics during the September 2014 event are closer to those also seen for the March 2013 and March 2015 events; in all three cases the depletion happened very fast ($\lesssim 0.5-2$ hours). In contrast, the September 2012 event has a more gradual loss. For the September 2014 event, the top panel of Figure 4.8 shows that despite the sudden inward motion of the magnetopause at 16:00 UT on September 12, 2014, the loss does not start until the IMF turns southward at 20:15 UT and when the LCDS rapidly moves inward to $L^* \approx 5$. Even this short inward excursion of the

LCDS is sufficient to cause the fast losses and belt extinction.

For the September 2012 event (bottom panel of Figure 4.8) the IMF turns southward at the beginning of the storm but only gradually increases in its magnitude over the next 48 hours. The LCDS gradually moves inward during this interval to reach $L^*\approx 6$. Significantly, the magnetopause remains at a standoff distance of $\gtrsim 10$ Earth radii throughout this interval until the shock arrival at around 12 UT on September 3. Note that this event, although characterized by the generation of a third radiation belt, was only a moderate storm with SYM-H only reaching a minimum of $-77\,\mathrm{nT}$. Figure 4.7 shows that the Van Allen Probes reveal a period of rather gradual loss in September 2012, in advance of the arrival of the interplanetary shock. This is consistent with the analysis by *Mann et al.* (2016) who asserted that outward ULF wave radial diffusion was responsible for the losses during this storm and which began in advance of the shock arrival. Interestingly, as shown in Figure 4.8 (bottom panel), at GPS altitudes the shock does not seem to be associated with additional fast losses, although as the LCDS moves in further the fluxes at GPS gradually are further reduced in concert with the proximity of the LCDS.

Overall, Figure 4.8 emphasizes the importance of the proximity of the calculated LCDS as a function of L^* for assessing radiation belt losses, as opposed to merely regarding *Shue et al.* (1998) magnetopause location in units of R_E as and approximation for the L^* of the LCDS. Consistent with the analysis of the LCDS in *Alves et al.* (2016), the September 2014 storm is characterized by fast outward losses through the LCDS. During this event, the LCDS remains at $L^*\approx 6$ for a couple of hours, presumably low enough in L^* for fast outward ULF wave transport to create the observed extinction. This contrasts with the September 2012 event where, consistent with the calculations of *Mann et al.* (2016), a more distant LCDS appears to lead to a more gradual rate of loss for the belts. For these September storm events, we also present data for additional GPS energy channels in figure 4.9. Data from this wider range of energy channels again supports the conclusion that outward transport to the LCDS was responsible for the observed losses.

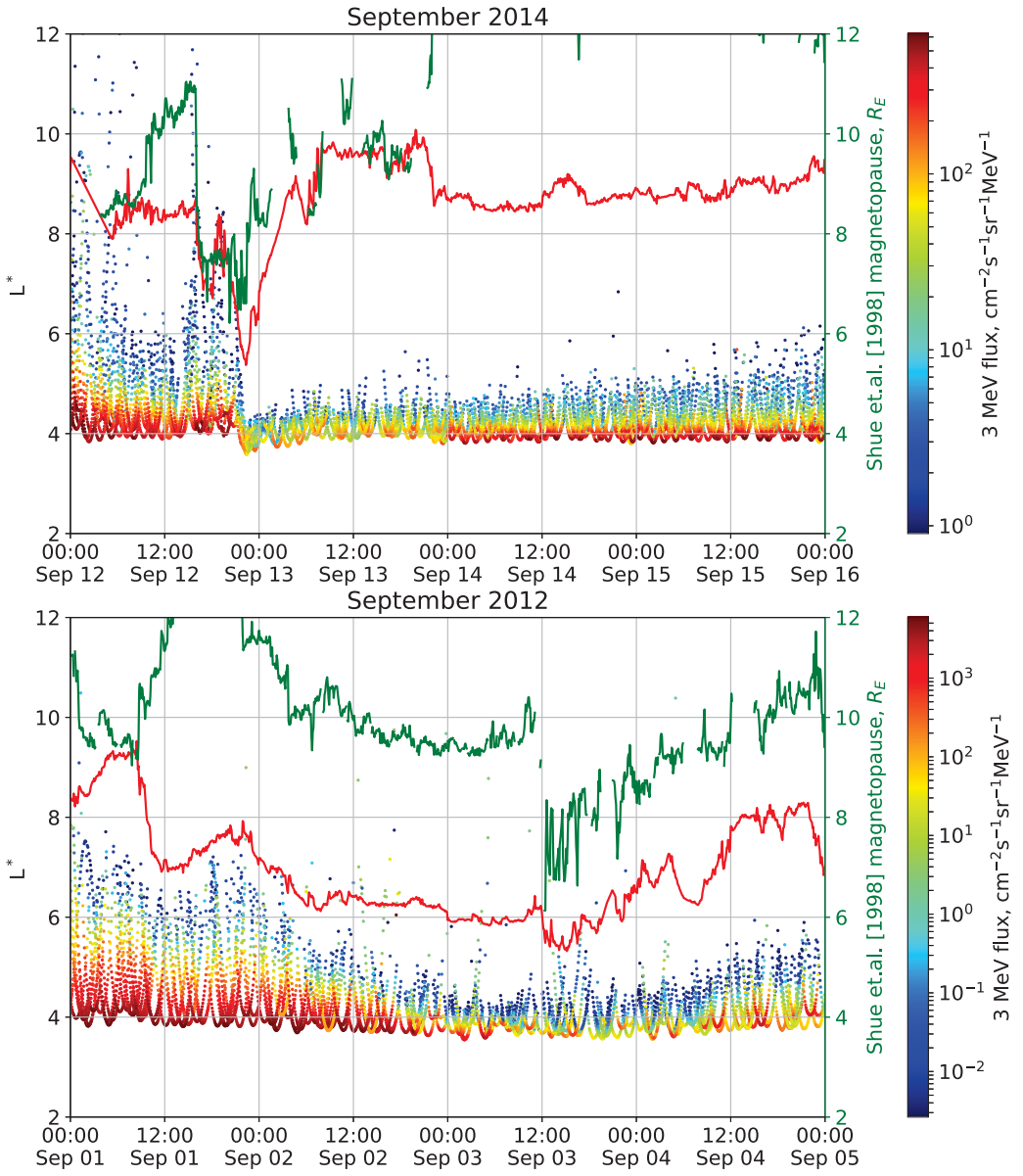

Figure 4.8: 3 MeV electron flux from the GPS satellite constellation as a function of L^* (left axis) for the September 2012 and September 2014 storms. Last closed drift shell L^*, calculated using LANL* neural network, is shown with a red line. The magnetopause standoff distance in units of Earth radii, calculated using *Shue et al.* (1998) model, is shown with a green line and should be read from the right hand axis. Note that for the September 2014 event the *Shue et al.* (1998) model gives a magnetopause position > 12 L for an extended period of time.

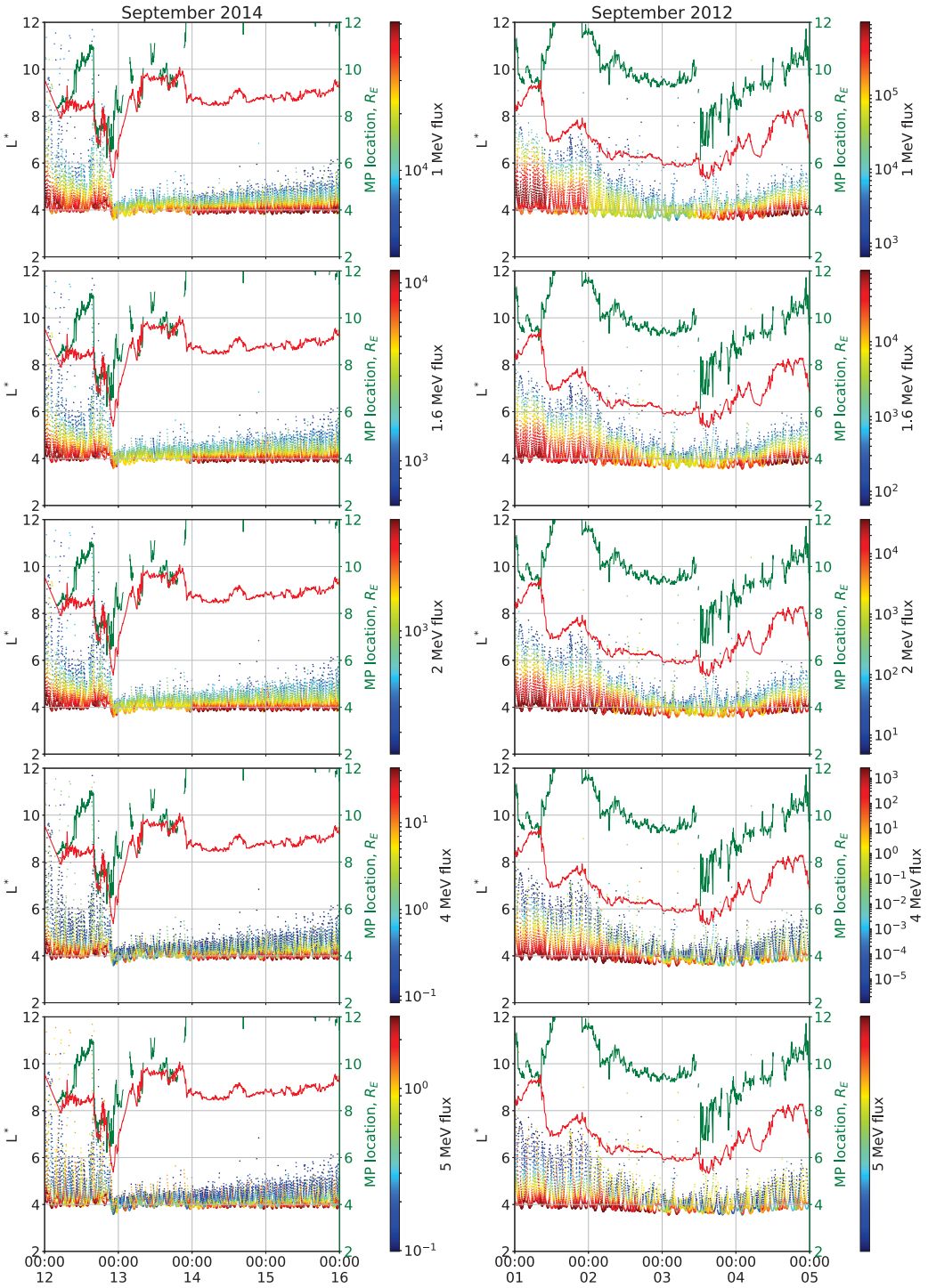

Figure 4.9: Energetic electron fluxes ($cm^{-2}s^{-1}sr^{-1}MeV^{-1}$) from the GPS satellite constellation data for the September 2014 and September 2012 events. Last closed drift shell position in L^*, calculated using the LANL* neural network, is shown with a red line. Magnetopause position, calculated using the *Shue et al.* (1998) model in units of R_E, is shown with a green line. Note, that for the 2014 event the *Shue et al.* (1998) model gives a magnetopause position $> 12\,\mathrm{L}$ for extended period of time.

4.2.3 Loss timescales

It is also relevant to analyze the time-dependence of the mean GPS flux as a function of McIlwain L-shell to study the morphology of the dropouts from a different perspective. This data is shown in Figure 4.10 for the March 2013 and 2015 events, and in Figure 4.11 for September 2014 and 2012. Each of the plots shows the average flux measured by the GPS satellites which are present in the specified L-shell bins. Figure 4.10 shows that for both the March 2013 and March 2015 events the dropouts happened first at high L-shell and then later at lower L-shell. Note that on March 17, 2015, following the dropout, the data on the higher L-shells is close to the noise floor and not shown. Figure 4.10 shows the same picture for both March storms with depletion on higher L-shells happening earlier than on the lower L-shells. Very significantly this indicates an inward propagation of loss consistent with magnetopause shadowing.

What is also very clearly seen in Figures 4.10 and 4.11, at least for the March 2013, March 2015, and September 2014 events, is that the timescale of the loss is very short, only $\sim 0.5 - 2$ hours, depending on the storm and L-shell bin. In all of these cases, the fastest losses occurred at the highest L-shells, while more gradual losses happened at lower L-shells but still within a short $\sim$ 2 hour timescale. The same overall pattern is also seen for the September 2012 storm, again with faster losses at higher L-shells and overall inward propagation of losses – consistent with magnetopause shadowing as proposed by *Mann et al.* (2016) – just on relatively slower timescales.

The September 2012 storm was characterized by losses at higher L-shells, which left the remnant belt at the inner edge of the outer zone. Following subsequent flux recovery on higher L-shells, this resulted in a third belt morphology with a flux gap between the remnant belt and the newly recovered outer belt (*Baker et al.*, 2013b). *Shprits et al.* (2013) introduced localized EMIC wave losses in the gap region into their modeling in order to reproduce the observed third belt morphology. More recently, *Mann et al.* (2016) argued that the remnant belt could be produced by outward ULF wave radial diffusion to the magnetopause, and that the third belt morphology did not require

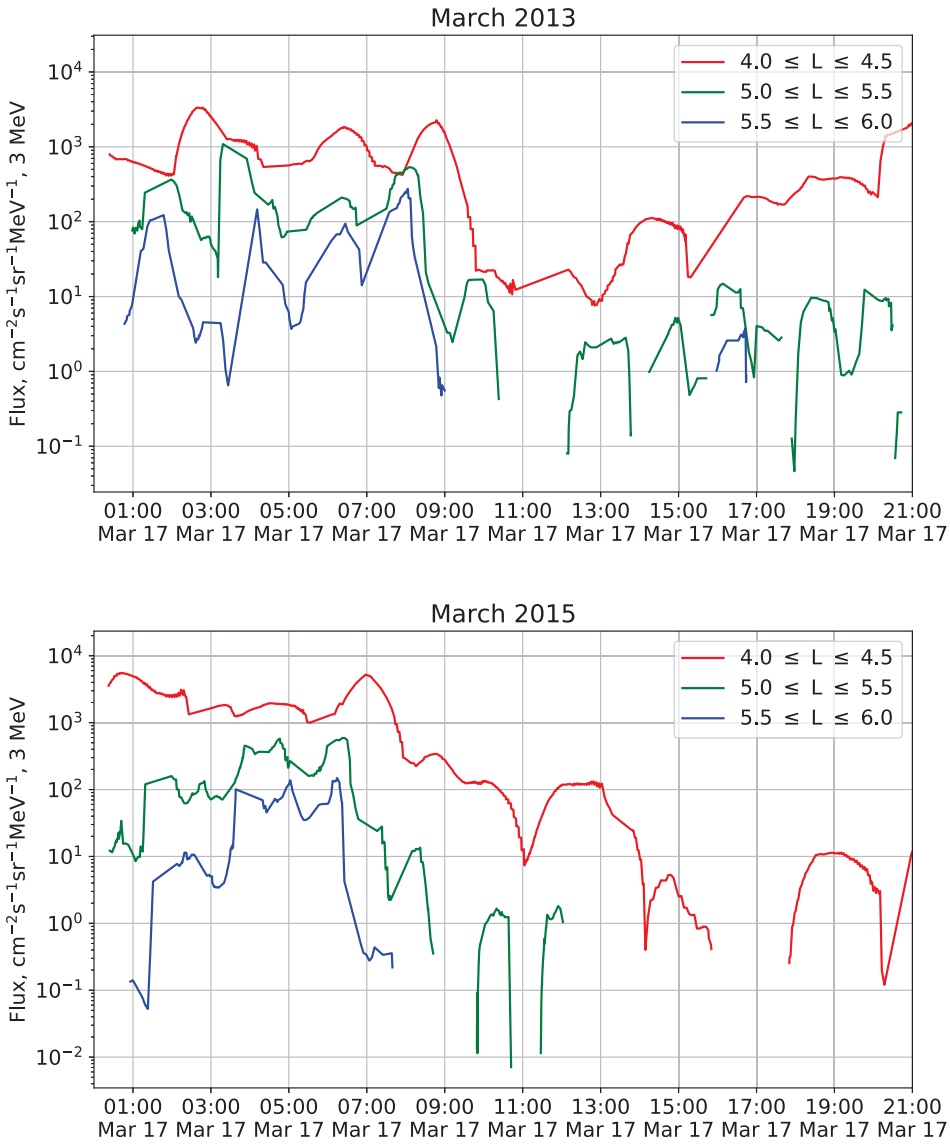

Figure 4.10: Time dependence of mean 3 MeV electron flux observed from the GPS satellite constellation binned in three L-shell ranges for the March 2013 and March 2015 storms.

the action of EMIC waves. *Shprits et al.* (2018) argue that the conclusions of *Mann et al.* (2016) are incorrect, and reiterate that in their view EMIC waves are necessary to create the third belt. In their reply to the *Shprits et al.* (2018) comment, *Mann et al.* (2018) presents phase space density profiles which decrease with L^* during the loss period consistent with their earlier hypothesis that magnetopause shadowing explains the creation of the third belt. The GPS

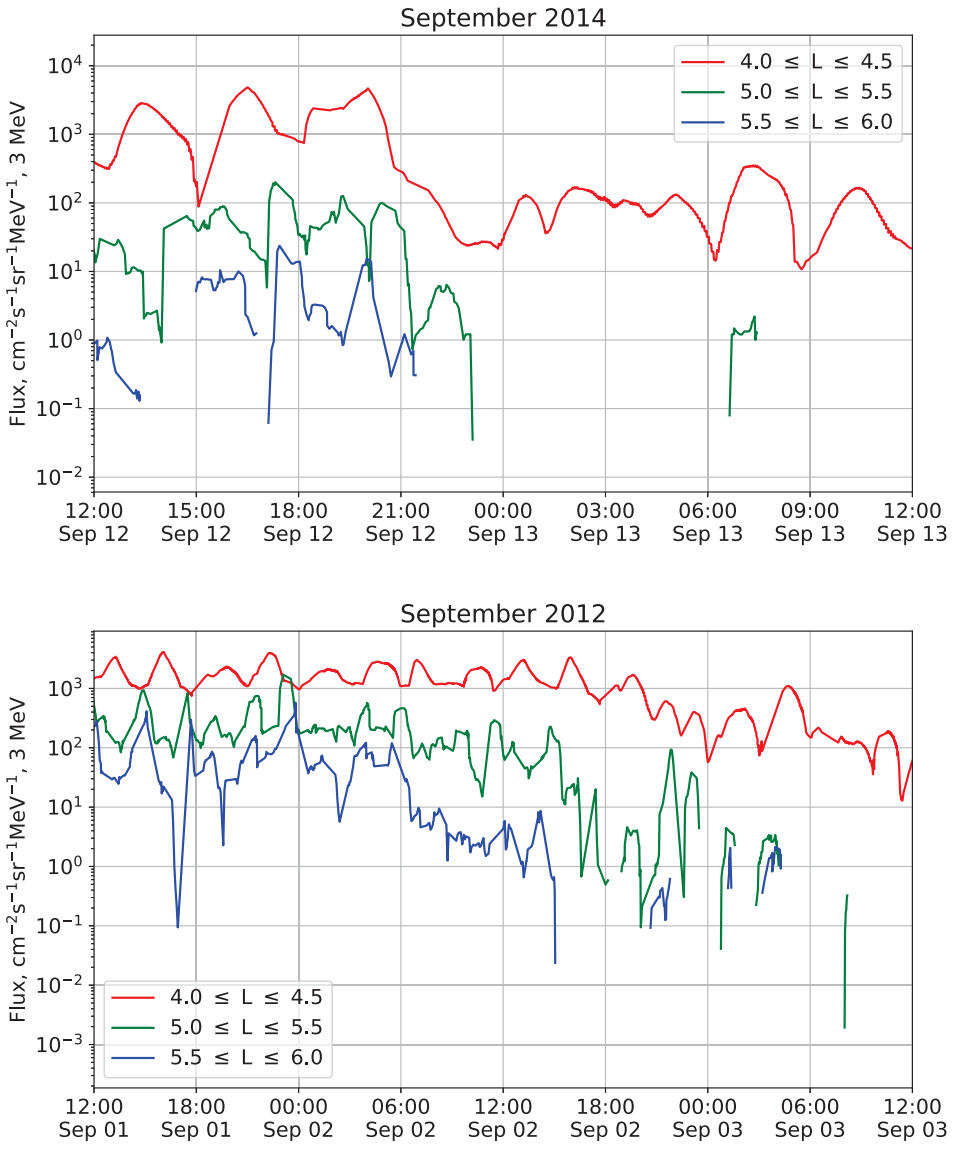

Figure 4.11: Time dependence of mean 3 MeV electron flux observed from the GPS satellite constellation binned in three L-shell ranges for the September 2014 and September 2012 storms. Note only 24 hours of data is shown for September 2014, whilst 48 hours is shown for September 2012.

and LCDS data in Figure 4.8 appears to be consistent with the conclusion of *Mann et al.* (2016) and *Mann et al.* (2018) that gradual outward ULF wave transport and magnetopause shadowing losses played a large role in creating the third radiation belt morphology.

4.3 Discussion and Conclusions

It is worthwhile to compare the results presented here to the results presented by *Morley et al.* (2010b). These authors compared the GPS electron flux as a function of dipole L observed in 61 sudden impulse events and superposed them with *Shue et al.* (1998) magnetopause location. The Morley et al. study hence clearly suggested a substantial role for solar wind compressions, a result which has also been reported in subsequent studies. However, for the sudden impulse events in the Morley et al. superposition, the magnetopause remained $\sim 2-3$ L-shells away from the location of the observed GPS losses. However, as we show here, when the location of the LCDS is calculated as a function of L^*, it lies much closer to the radiation belt where the losses are observed. As discussed by *Mann et al.* (2016), the remaining separation between the LCDS and the radiation belt can also be bridged by ULF wave outward radial diffusion. Our results imply that fast outward diffusion to a proximal LCDS can not only result in fast losses but under the appropriate conditions during intense storms, that such losses can create radiation belt extinctions and which can have a global effect on very fast timescales. As we showed here, such loss timescales are much shorter than the orbital periods of the Van Allen Probes. As we further demonstrated here, combining electron flux data for the constellation of GPS satellites allows such very fast radiation belt losses to be resolved, at least at the altitudes and L-shell ranges covered by the GPS satellite constellation.

Overall, *Morley et al.* (2010b) showed that there is a correlation between the radiation belt loss patterns in a geomagnetic storm and the dynamics of the magnetopause (classically calculated using the *Shue et al.* (1998) model). Similar patterns are present in some of the events from this chapter. However, a much stronger correlation exists between the loss trends and the last closed drift shell when calculated as a function of L^*. This LCDS correlation holds even for the rapid radiation belt extinction events of March 2015 and September 2014, and for these events, the inward motion of the magnetopause standoff is inconsistent with the timing of the actual dropout. This implies

that the crucial factor governing the loss in these events is the location of the LCDS. As the outer boundary in those events, losses at the LCDS will produce steep gradients in particle phase density in much closer proximity to the heart of radiation belt than implied by assuming it occurs on L-shells equal to the standoff distance in the *Shue et al.* (1998) magnetopause model. In our view in order to accurately model ULF wave outward transport, which is mostly governed by steep gradients in phase space density, the calculated L^* location of the LCDS is likely the key.

Studies of the temporal evolution of electron fluxes on different L-shells, as well as across a wide range of energies, reinforce our conclusion that transport to the LCDS and related magnetopause shadowing were the primary cause of the loss in the four storms studied here. In particular, the fact that the loss moves inwards and happens first on high L-shells and later on lower L-shells is consistent with outward ULF wave transport to an outer boundary determined in our case by calculation of the LCDS. Additionally, the observed loss patterns are the same for different energies from 1 MeV to 5 MeV (see figures 4.6 and 4.9) and all of them are strongly correlated with the LCDS. Our analysis was done using high resolution data from all available GPS satellites. This allows us to study electron flux dynamics with $\approx$ 30 minutes temporal and $\approx$ 0.25 Earth radii spatial resolution, as opposed to the $\approx$ 9 hours orbital period of the Van Allen Probes.

In this study, we used the LANL* neural network to perform the calculation of the LCDS. This approach has a tremendous advantage over the full calculation method in terms of the required computational resources. However, the neural network itself does not have any knowledge of the governing physics. Nevertheless, it was shown that the LCDS calculated using the LANL* neural network agreed well with the full LCDS calculation, at least for the March 2013 storm where we completed a validation. All of the above implies that when assessing magnetopause shadowing losses in the Van Allen radiation belts analyzing the last closed drift shell and working in L^* space is more reasonable than regarding a classical *Shue et al.* (1998) model of magnetopause standoff distance in terms of Earth radii as the L-shell where shadowing losses occur.

Chapter 5

Superposed Epoch Analysis of Magnetopause Shadowing Events

As was shown in the previous chapter, knowing the location of the last closed drift shell (LCDS) in L^* space as determined by the location of the magnetopause and the electron drift orbits, appears to be crucial when assessing radiation belt extinction events during intense geomagnetic storms. The significant inward motion of the LCDS is often present in such events, and where the primary cause of the loss appears to be the outward radial diffusion combined with the magnetopause shadowing. These results suggest the possibility of investigating the behavior of the Van Allen belts from the inverse direction. By organizing the dynamics with respect to the LCDS, instead of investigating the measured flux or phase space density (PSD) can pinpoint times where the radiation belts would be expected to experience loss due to magnetopause shadowing. Selecting events in such a way can be validated by investigating the trapped radiation populations.

In this chapter, we investigate 64 geomagnetic storms, that happened between 2012 and 2018, by analyzing flux and PSD data from the Van Allen Probes arranged by the dynamics of the LCDS. We perform a statistical analysis of these storms using a superposed epoch approach, where zero epoch is selected as the time of the minimum L^* of the LCDS in each storm. Our results show that during the main phase of these storms the dynamics of the Van

Allen belts stay consistent from storm to storm. Additionally, the behavior of the electron population in the superposition is very similar for different energies or first adiabatic invariants – the result being consistent with the radial diffusion and magnetopause shadowing paradigm. However, the behavior during the recovery phase may vary not only between individual storms but also is different at different energies. In particular, the analysis of flux data from the Van Allen Probes reveals that the lower energies recover faster, contrary to common assumption often made with the radiation diffusion paradigm. Moreover, the PSD data reveal that the PSD at higher L-shells recovers faster, with recovery timescales being on the order of couple hours. Since this timescale can be shorter than the revisit times available for the Van Allen Probe orbit, the latter implies that when assessing individual radiation belt loss events, it may be crucial to analyze data with higher time and L-shell resolution. Such data can be provided by the constellation of the GPS satellites.

5.1 Data and Methodology

The statistical analysis of these 64 storm events was performed for the Van Allan Probes era which starts in September 2012. In particular, for this study, we used data from September 2012 until May 2018. As was mentioned above, the selection of the storms to be used in the superposed epoch analysis was based on last closed drift shell dynamics. This approach requires information on the LCDS location during these 6 years with high enough resolution to resolve effects happening on 1-hour timescales. Multiple approaches currently exist for the LCDS calculation (*Albert et al.*, 2018). However, as was mentioned in the previous chapter, the fastest way to calculate the LCDS is using the LANLmax algorithm (*Yu et al.*, 2012) from the LANL^* neural network provided by SpacePy (*Morley et al.*, 2011) python package. Following the results of *Brito and Morley* (2017), we perform calculations of the LCDS and all L^* parameters based on the *Tsyganenko and Sitnov* (2005) model. As the inputs for the neural network, we use the magnetic field input parameters derived from data on OMNIWeb, also known as QinDenton parameters and available

through the Van Allen Probes data hub. In particular, we used 5-minute and 1-minute resolution data in this study.

Observations of the recurrence of magnetic storms show that because of the variable nature of the solar wind two consecutive storms can be separated by times as short as one day or as long as one month. Therefore, to ensure that during the analysis we used storms with a single radiation belt loss-restoration cycle, we developed an algorithm for magnetopause shadowing event selection. The algorithm was based on two rules. The first that the LCDS should drop below L^* of 5.8, and the second that there are no other instances of such a low LCDS locations up to either three days before or three days after the event. Processing 1-minute LCDS data for the almost six-year period, calculated as mentioned above, 64 storms were selected. The full list of the selected events is shown in Appendix A.

Each of the selected storm events shows signs of magnetopause shadowing as a governing factor in the loss. For example, all of the four storms, discussed in the previous chapter were also selected for this analysis by the algorithm. To investigate the response of the radiation belt during the 64 selected events we used data from Van Allen Probes A and B. The Van Allen Probes provide electron flux data from the Relativistic Electron-Proton Telescope (REPT) instrument (*Baker et al.*, 2013a) and the Magnetic Electron Ion Spectrometer (MagEIS) (*Blake et al.*, 2013). REPT provides electron flux data for highly-relativistic electrons with energies above 1 MeV. Meanwhile, MagEIS provides electron flux data for lower energies. The REPT and MagEIS instruments provide not only energy but also pitch angle resolution of trapped radiation. With combination with a magnetic field model, it allows us to calculate the electron PSD from the flux data, with the goal of removing adiabatic effects arising for example from the Dst effect (e.g., *Li et al.*, 1997) to help with data interpretation. Therefore, in this study, we perform superposed epoch analysis of not only electron flux but also PSD. Note that we focus on the analysis of omnidirectional flux, as well as PSD with $K = 0.01\ R_E\mathrm{G}^{0.5}$ which corresponds to equatorial pitch angles of 85°-90° at Van Allen Probes altitudes.

The PSD calculation at fixed adiabatic invariants was performed by merg-

ing both REPT and MagEIS data into the single dataset to provide a more comprehensive energy range. Energies above 1.6 MeV are taken from the REPT instrument, and below 1.6 MeV from MagEIS. Even though MagEIS provides coverage at higher energies, but the data on those channels are often close to the noise floor. Also, note that both the MagEIS and REPT datasets were calibrated by the Van Allen Prbes team over a long period and currently provide consistent data between each other (see MagEIS Release 4 notes on RBSP ECT team website for more detail `www.rbsp-ect.lanl.gov/`). The PSD calculation was performed by using the LANLGeoMag software library (*Henderson et al.*, 2017) for the *Tsyganenko and Sitnov* (2005) magnetic field model. During the calculation, flux as a function of pitch angle, energy, and the position of the satellite was converted to PSD as a function of three adiabatic invariants μ, K, and L^*.

In this study, we perform the *superposed epoch analysis*. For each of the events, a zero epoch time was selected as the minimum L^* of the LCDS. Afterward, all 64 events were superposed based on this epoch. We superposed space weather parameters for the different storms to perform a statistical analysis. Solar wind parameters and the LCDS location were averaged between different storms to provide mean solar wind data as a function of the superposed epoch. Figure 5.1 shows mean solar wind conditions and the mean LCDS location for the ensemble of 64 selected storms. We show mean values with the red line, the median values with the black line, and the quartiles with the gray lines. Note that even though the selected events all have the LCDS minimum L^* lower than 5.8, the average (and median) value during zero epoch is only 5.5. Meaning that LCDS L^* values lower than 5 are extremely rare, as confirmed by the data table in Appendix A.

Performing the superposed epoch analysis of the flux or PSD data for the Van Allen Probes is more complicated than just averaging over events at different times. Because the Van Allen Probe orbits constrain the observations of the trapped radiation, such that a particular position (L^*) is absent at a specific time during the storm for a single satellite, we performed the superposed analysis by mapping the observations of the flux or PSD onto a grid.

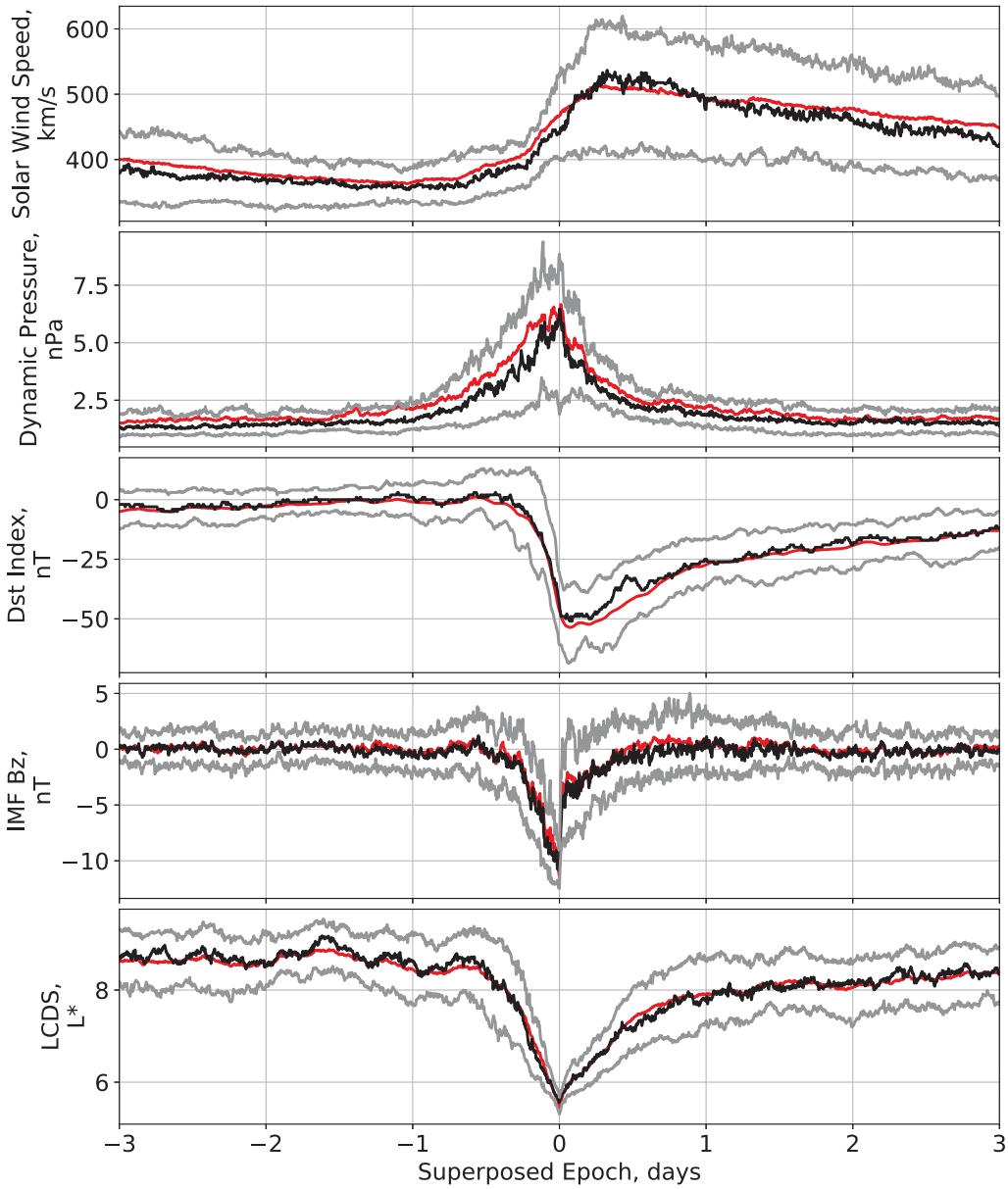

Figure 5.1: Superposed epoch summary of selected solar wind, geomagnetic indices, and the last closed drift shell L^* location for the selected events. From top to bottom for each storm: x-component solar wind velocity in GSE coordinates; solar wind dynamic pressure; Dst index; z-component of the interplanetary magnetic field in GSM coordinates; and the LCDS location in L^*. For each panel the mean value across all events is shown with the red line. Black line and two gray lines represent the median value with the lower and upper quartiles respectively.

Figure 5.2 shows a schematic representation of this process. The top left panel of Figure 5.2 schematically shows the track of one of the Van Allen Probes during one of the selected events. This track was discretized on a fine grid to produce data bounded to specific points in (L^*, t) space which are consistent across different events. The discretization is schematically shown in the top right panel of Figure 5.2. The median PSD or flux value is then assigned to each of the grid cells. Note that the median value is of course only taken over that data which coincides with the respective grid cell. The top right panel of Figure 5.2 shows cells in the (L^*, t) space containing data in black and those without data in white. Additionally, the middle row of the Figure 5.2 shows the same scheme but for a different probe or event. Each cell in (L^*, t) space is hence filled with an array of data by performing discretization on the same grid for both Van Allen Probes for all 64 storm events. To illustrate the combination of the data from the two grids, combined coverage of the two orbital passes in the passage above is shown in the right-hand panel on the bottom row of the Figure. Superposing these grids from 64 different storms for both Van Allen Probes A and B creates the grid with approximately evenly filled cells (see Figure 5.3). Note that if the cell has more than one entry from different probes or events, the median value of PSD or flux is assigned as the final superposed epoch value. in each bin in the (L^*, t) space.

The (L^*, t) grid used in this study has 120 cells in the superposed epoch ranging from -3 to 3 days, and L^* was split into 50 cells ranging from 1 to 7.5. Note that the L^* has a slight dependence on the particle pitch angle, or in relation to PSD the second adiabatic invariant. Therefore, slightly different coverage of this grid is present for different values of these variables. As was mentioned above, for the flux comparison we use omnidirectional flux from the Van Allen Probes. However, the L^* value used for the flux analysis was calculated by assuming the 90° pitch angle, consistent with the fact that the pitch angle distributions are most often peaked at 90°. Figure 5.3 shows how many events contributed to each cell when analyzing the omnidirectional flux. The average coverage for L^* from 3 to 5 is 29 storms per cell, with a standard deviation of 4. The outer radiation belt mostly spans this L^* region. Figure 5.3

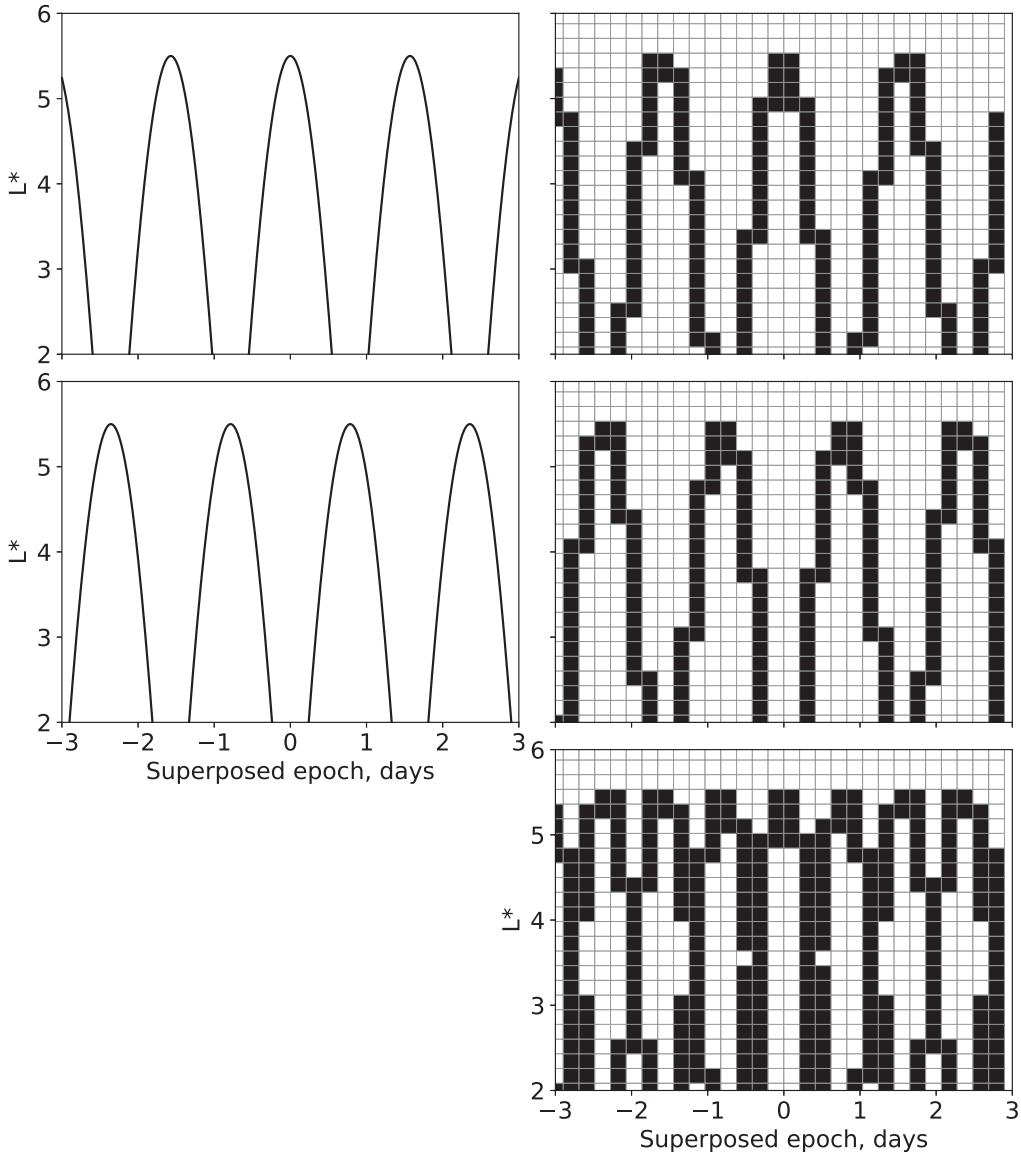

Figure 5.2: Schematic representation of the approach used to develop L^* and time superposed epoch analyses in this study. The left column schematically represents the actual orbits of the Van Allen Probes A and B as the function of L^* and time and which were discretized on a grid, shown in the right column. The black cells represent those containing data from at least one storm or probe. Meanwhile, the white cells represent no data. The bottom row schematically shows the superposed analysis from two storms and the final coverage of the grid. The superposed epoch results were then obtained by completing this process for all 64 selected storms and estimating median values in each cell. See text for more details.

also shows that there is a slight fluctuation of the coverage from cell to cell. However, the fluctuations stay at approximately the same level for different epoch times, thus proving that the selected grid resolution is appropriate for the superposed epoch analysis. Figure 5.3 also shows the mean, median, and quartile statistical location of the LCDS in the same format as in Figure 5.1.

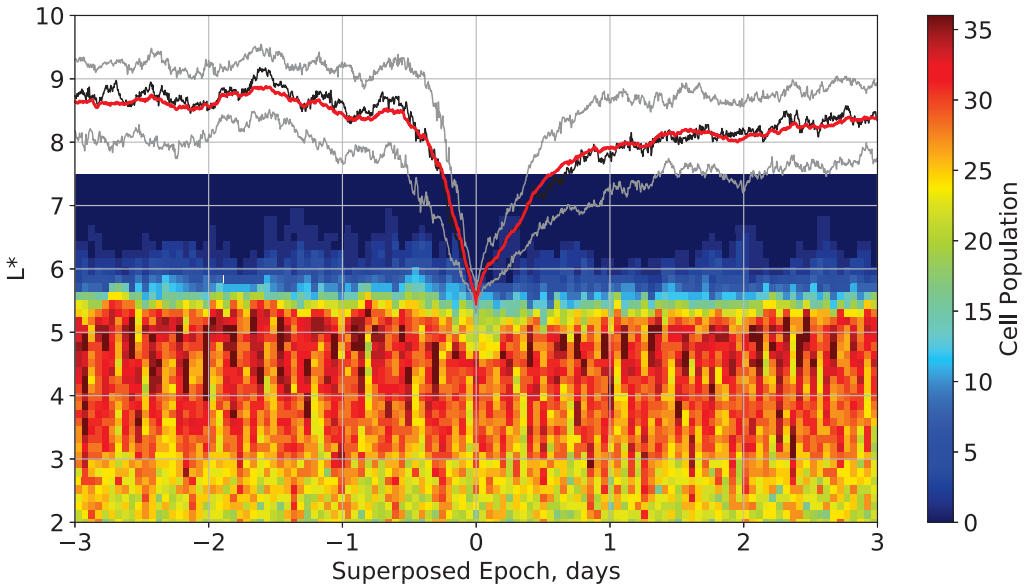

Figure 5.3: The number of events per cell which was used when determining the median omnidirectional flux in the superposed epoch analysis. Note that the average cell coverage for the L^* range from 3 to 5 is 29 storms per cell with a standard deviation of 4.

5.2 Superposed Epoch Analysis of the Electron Flux

Figure 5.4 shows the median omnidirectional flux for different energies and which was obtained using the previously described superposed epoch analysis on a fixed grid. The flux, although the omnidirectional flux is determined from spacecraft spin averaging, is provided in units of $\mathrm{cm}^{-2}\mathrm{s}^{-1}\mathrm{sr}^{-1}\mathrm{MeV}^{-1}$. Note that the upper and lower energy range is the same in the color scheme in each panel. Additionally, each panel shows the statistics of the superposed LCDS position in the same format as in Figure 5.1. Data from all of the

panels reveal that there are no apparent changes in the median pre-storm flux along different L-shells approximately half a day before the minimal LCDS L^* location. However, after the statistical LCDS location starts to move inwards from the average pre-storm value of $L^*= 8.75$, changes in the independent measurements of the electron flux for the Van Allen Probes start to appear in all of the energy channels. From the data presented in Figure 5.4 it seems that the losses are happening with rather consistent rates across the different energy channels, and starting earlier on higher L^*. However, after the minimum in the LCDS L^*, the lower energy populations begin to recover earlier and, reach the flux levels slightly above pre-storm values.

Significantly, the losses can penetrate deep into the heart of the outer belt with the median flux showing signs of loss on L^* as low as $L^*\approx3$. However, from the representation of the data in Figure 5.4, it is hard to visually gauge the actual L^* and energy dependence of the loss as a function of time. Therefore, to perform a more detailed numerical analysis of the flux data, we show, as an example, a cross-section made along fixed L^* of 5 for the flux of 2.1 MeV electron energy in Figure 5.5.

The top panel of Figure 5.5 shows result for the cross-section of the second panel in Figure 5.4, representing the median flux of 2.1 MeV energy electrons at $L^*= 5.05$. The solid black points show the median flux values, while, the upper and lower quartiles are represented as the error bars at each time point for this L^* bin. This plot confirms the previous observation, shown in Figure 5.4, that there are no apparent changes in the median flux up until at least 0.5 days before the minimum L^* of the LCDS. It also shows, in terms of the median flux for this ensemble of storms, that the final post-storm flux recovers slightly above its pre-storm value. An interesting observation is that the error bars maintain an almost constant magnitude throughout the interval spanning from the pre-storm, trough the period of the electron loss, and even into the post-storm period. However, this superposition does not allow one to distinguish between individual events where the flux recovered to either below or above the pre-storm values.

The relatively large error bars during the pre-storm phase in the top panel

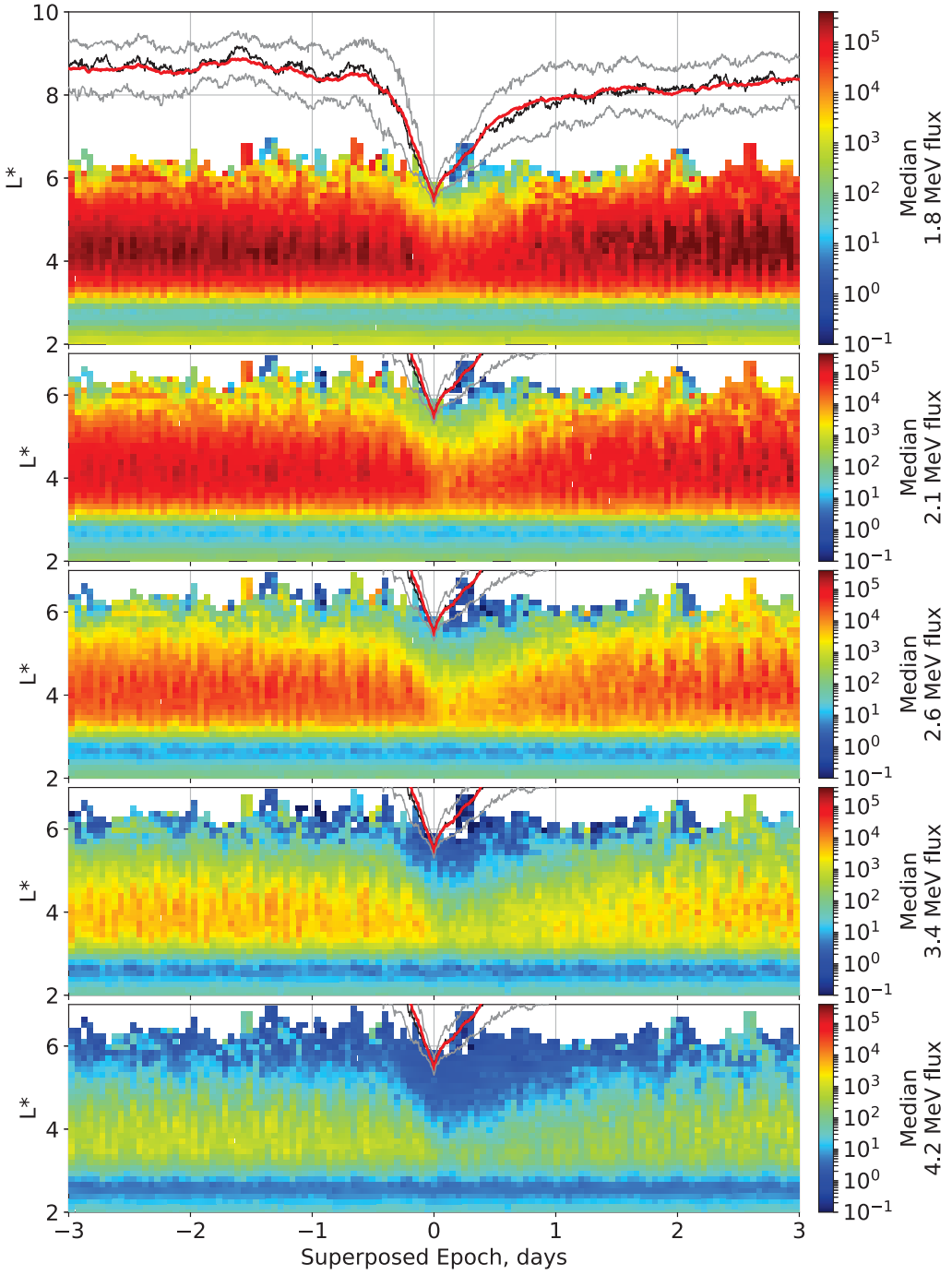

Figure 5.4: Superposed epoch analysis of the median electron flux in units of $cm^{-2}s^{-1}sr^{-1}MeV^{-1}$ for different energies for 64 storms associated with inward motion of the LCDS. From top to bottom panels show median omnidirectional flux in the different energy channels. All data was taken from the REPT instrument on board of the both Van Allen Probes. The statistical mean, median, and quartile location of the LCDS is overplotted in the same format as in Figure 5.1.

of the Figure 5.5 mean that there is a wide range of initial, pre-storm, flux. Therefore, to examine the repeatability of the loss during each of the storms and to investigate the loss-recovery process in more detail, it is convenient to introduce a *normalized flux* at fixed energy. The value of the flux is divided by its median value at a particular L^*, and where the median is taken over the pre-storm period from 3 to 1.5 days before the minimum of the LCDS L^*. The normalization flux may also be considered to represent an *initial flux*. Note that this initial flux will be different for different energies, L^*'s, or events. However, it is determined using data from both Van Allen Probes A and B during the same event and hence is the same for both probes. An example of the superposed epoch analysis of the normalized fluxes for each of the storms is shown in the bottom panel of Figure 5.5, where the median normalized flux with its quartiles is shown for the 2.1 MeV energy channel population at L^*=5.05. Note also that the normalization was performed for each L^* in each event, and after performing the superposition of all events, the median normalized flux was determined with quartiles and plotted on the bottom panel of Figure 5.5.

The results presented in the bottom panel of Figure 5.5 show that during the pre-storm phase until $\sim$ 1 day before the minimum LCDS L^* that there are no apparent changes in the median normalized flux. Moreover, the error bars, which now represent the upper and lower quartiles in the normalized flux, remain relatively small during this period. After the loss starts after $t = -0.5$ days, it continues until $t \sim +0.25$ days, meaning that the loss on this particular L-shell continues even after the LCDS minima in L^* was reached. During this period of loss, the error bars in normalized flux increase, representing different rates of loss. However, they still stay relatively small. After $t \sim +0.5$ days, the recovery phase starts and the error bars, as well as fluctuations of the median values, increase significantly by approximately an order of magnitude. However, the almost symmetrical spread of the error bars around the median normalized flux values during the recovery phase, suggests that the recovered flux is as almost equally likely to be larger than the pre-storm level as it is to be lower. Moreover, the median of the final recovered

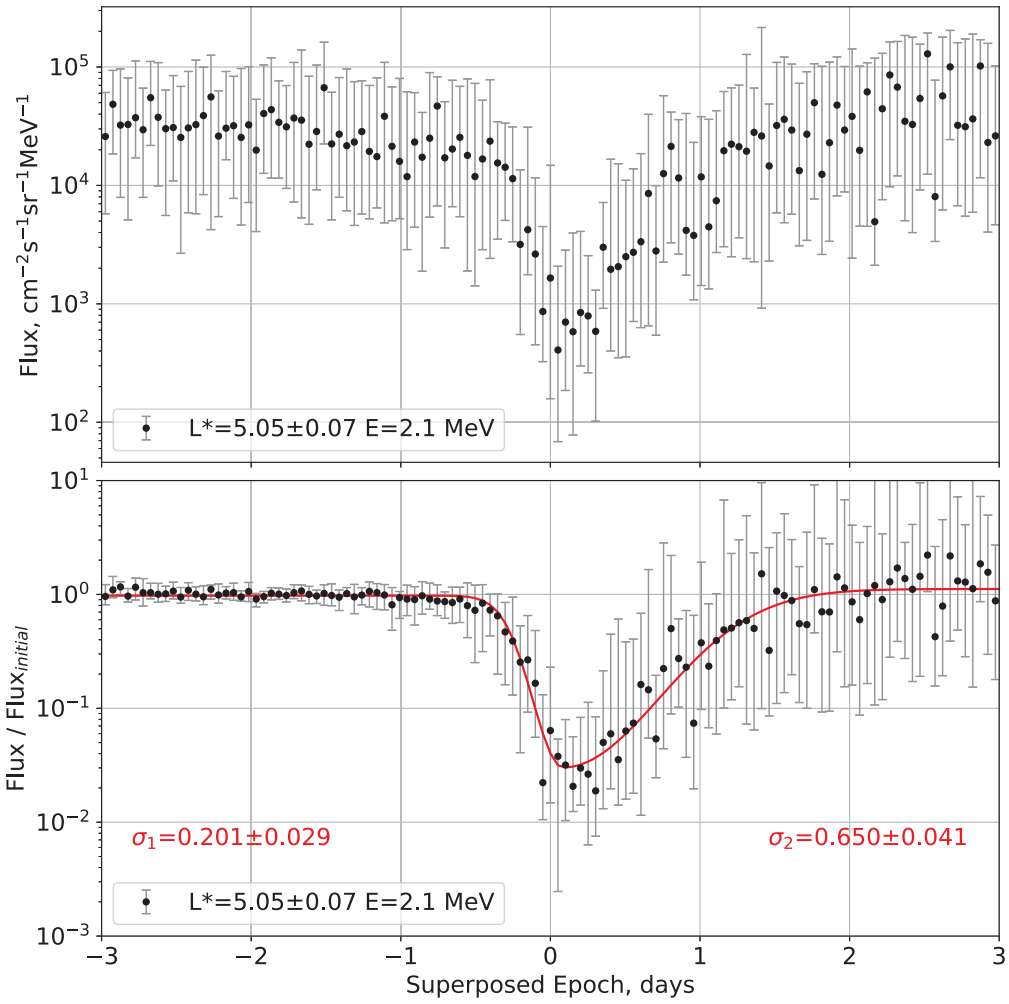

Figure 5.5: Superposed epoch 2.1 MeV energy electron flux (top panel) and normalized flux (bottom panel) at L^* bin with the mean L^*= 5.05 and the with the boundaries away from the mean by 0.07. The black scatter plot shows the median values of the flux as a function of the superposed epoch. The error bars represent the upper and lower quartiles for a particular time. The bottom panel also shows the fit of the median normalized flux with a two-sided Gaussian (equation 5.1).

normalized flux is only slightly higher than the initial flux, suggesting increases and decreases in the flux are approximately equal in magnitude and of equal likelihood.

To assign numerical values to analyze the processes happening during the loss and recovery phases we fit the normalized flux data in the bottom panel of Figure 5.5 with a two-sided Gaussian, shown in red, in logarithmic space

such as:

$$f(t) = \begin{cases} (A - b_1) \exp\left\{-\frac{(t-\mu)^2}{2\sigma_1^2}\right\} + b_1, & \text{if } t < \mu, \\ (A - b_2) \exp\left\{-\frac{(t-\mu)^2}{2\sigma_2^2}\right\} + b_2, & \text{otherwise,} \end{cases} \tag{5.1}$$

where A, b_1, b_2, μ, σ_1, and σ_2 are fit parameters, t is the superposed epoch, and f is $\log_{10}(\text{Flux}/\text{Flux}_{\text{Initial}})$. Note that the function $f(t)$ is constructed in a way such that if $t = \mu$, the first and the second equation provide the same result, characterizing the normalized flux minimum and equal to A. Parameters b_1 and b_2 determine how much loss and recovery there is compared to the flux minimum A. σ_1 determines how early the loss starts, and σ_2 determines how long it takes for the flux to recover. Note that we also fit the μ parameter which determines when the loss stops and the recovery begins. This time is independent of the zero in the epoch time and which is defined by the minimum L^* of the LCDS of each storm. The fitting was performed using python `curve_fit` algorithm available through scipy package (`www.scipy.org`). The uncertainty of the fit parameters was determined from the diagonal elements of the covariance matrix in this function. However, no uncertainties were used in this fitting routine. The fitting of the normalized flux with the two-sided Gaussian function in (5.1) nicely represents the characteristics of the data.

Performing the fitting for multiple values of L^* and energy channels we can investigate how the typical loss time (σ_1) and typical recovery time (σ_2) depend on those parameters. Appendix B provides these results with figures showing all of the fits, similar to the bottom panel of the Figure 5.5, but for different L^* and energy channels. Figure 5.6 shows a summary of the fit parameters σ_1 and σ_2 in grouped form with respect to L^* for different energy channels. Note that the error bars for the data points were obtained from the fitting algorithm and that the scale of each panel is different. Note that the error bars for the data points were obtained from the fitting algorithm and that the scale of each panel is different.

The top panel of Figure 5.6 shows the dependence of σ_1 on L^* for different energy channels, each shown in a different color. With the exception of the very lowest L^* channel where the flux count is low, starting at L^* of 3.75 the

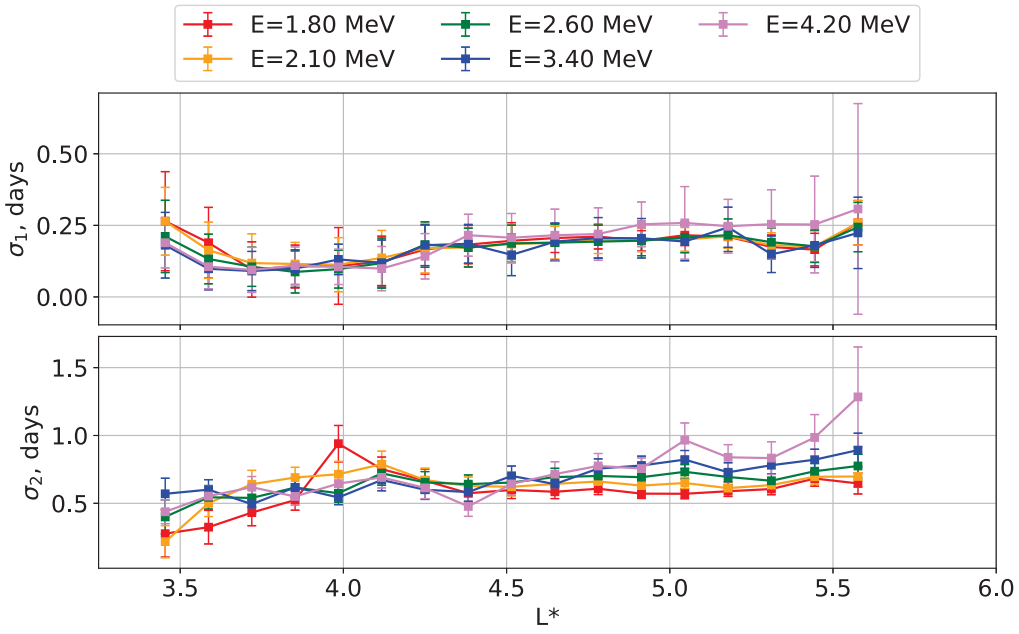

Figure 5.6: Normalized flux fit parameters σ_1 (top panel) and σ_2 (bottom panel) as a function of L^* for different energy channels. σ_1 represents the characteristic time of the loss of normalized flux, while, σ_2 represents the characteristic time of normalized flux recovery. The error bars were determined during the least squares fitting algorithm.

value of σ_1 monotonically increases with L^* value, meaning that the losses start earlier at higher L-shells and reach values of $\sigma_1 \approx 0.2$ at L^* of 5.5. These results are consistent with the magnetopause shadowing paradigm, where the higher L-shells are expected to be affected earlier by losses to the magnetopause and which over time gradually moves inward. An interesting observation is that the σ_1 parameters for all energies are very close to each, across all L^*, suggesting that the radiation belt response during periods of the loss is energy independent, which is consistent with the magnetopause shadowing paradigm. None of the σ_1 for a particular energy channel deviate from other channels for more than one standard deviation. It is also an interesting observation that the characteristic timescale of the loss on the L^* of 5.5, as determined by half width at half maximum (HWHM) and equal to 0.23 ± 0.02 days, is the same as the characteristic timescale of the dynamics of the LCDS, with HWHM=0.23 days. The agreement between these two values suggests that the separation with L^* of 2 is small and can be easily breached, by fast outward

radial diffusion acting during the magnetopause shadowing events.

Similarly, the bottom panel of the Figure 5.6 shows the flux recovery phase fit parameter σ_2. Unlike σ_1, there is an apparent energy dependence of the fit parameters, being clearest at L^* above $\approx$4.5. This energy dependence is also present to some degree on the lower L-shells but is not as clean.

If the radiation belts are replenished as a result of the inward transport of new source populations, the rate of flux recovery at different energies might be expected to be strongly controlled by the rate of recovery of new source populations at the outer edge of the Van Allen belts. However, there are very few such studies published in the literature. Based on modeling of the September 2012 third radiation belt (*Baker et al.*, 2013b), *Mann et al.* (2018) suggested that such energy dependent flux recovery might happen during the recovery phase of that storm. *Mann et al.* (2018) argue that the flux recovery was dominated by the inward motion of particles and their acceleration due to the ULF wave radial diffusion. Their observations and modeling suggest that lower energy source flux at the outer belt might recover first, which is consistent with the results presented in this chapter. The bottom panel of Figure 5.6 additionally shows that σ_2 slowly increases in magnitude with L^* at fixed energy. However, this might also be caused by adiabatic effects and this is addressed in the next section where the dynamics of the electron PSD are investigated.

5.3 Superposed Epoch Analysis of the Electron Phase Space Density

Similar to the analysis of the electron flux presented in the previous section, here we show results for a superposed epoch analysis of the electron phase space density during the same 64 magnetopause shadowing events. Figure 5.7 shows the superposed epoch PSD for different first adiabatic invariants, μ, in the same format as Figure 5.4. The second adiabatic invariant is fixed during this analysis at $K = 0.01\ R_E\mathrm{G}^{0.5}$. Note that all panels in Figure 5.7 have the same color scale.

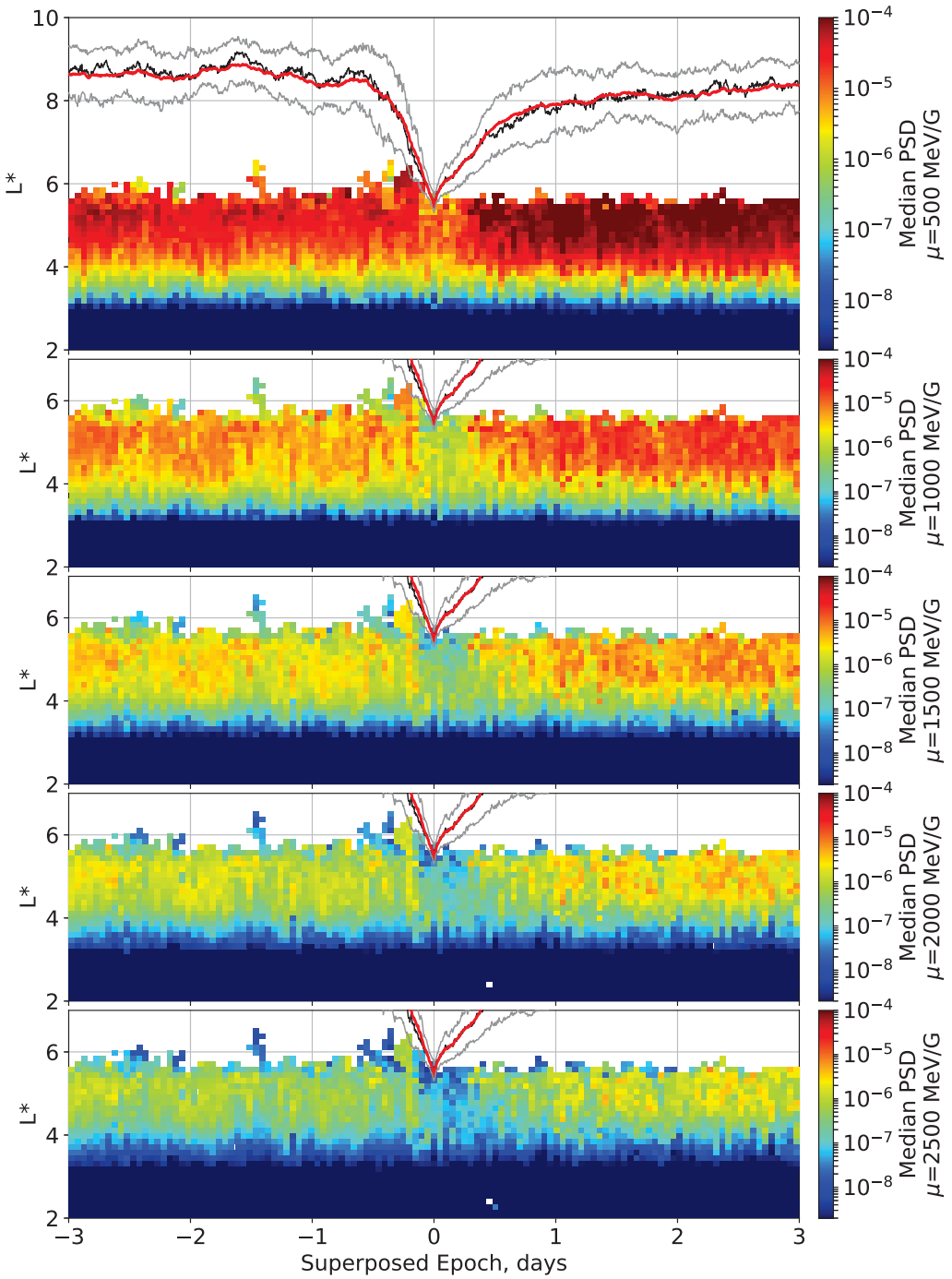

Figure 5.7: Superposed epoch PSD from the Van Allen Probes for different first adiabatic invariants in units of (c cm^{-1} MeV^{-1})^3 for different first adiabatic invariants for 64 storms associated with inward motion of the LCDS. Note that the color scale of the plots is the same. Also, the location of the LCDS is shown in the same format as in Figure 5.1.

The calculation of PSD as a function of adiabatic invariants from the flux measurements can be a challenging task. It relies on a magnetic field model and a number of assumptions (see e.g., *Chen*, 2005; *Spence et al.*, 2013; *Mann et al.*, 2018; *Shprits et al.*, 2018). Perhaps, because electron flux is the measured parameter and because of uncertainties in the model magnetic field, the results of the superposed epoch analysis for the PSD data do not appear to be as clean as those for the flux. However, the PSD representation does provide multiple additional insights. The immediate observation is that the recovered PSD is clearly larger than the pre-storm level by almost an order of magnitude for all values of μ shown in Figure 5.7. Also, it seems that there are no apparent differences if PSD behavior at different L^* during the loss phase, i.e., all L^* are being depleted at the same time with very short timescales, presumably by very fast acting losses from magnetopause shadowing. However, during the recovery phase, there is a clear L^* dependence of the PSD dynamics with higher L^* recovering faster. This is consistent with the hypothesis that inward transport motion and acceleration of new source populations explain the flux recovery during the recovery phase.

In the same manner as before, we further performed fitting with the two-sided Gaussian function (equation 5.1) using median normalized electron PSD data for different L^* and μ. The values of σ_1 and σ_2 as a function of L^* for different μ are shown in Figure 5.8. Meanwhile, Appendix C shows details of the median PSD plots for each L^* and μ with their fits, similarly to those shown in the bottom panel of Figure 5.5 and in Appendix B for electron flux data. We would like to note that the PSD at $L^*<4.5$ are almost completely unaffected by any loss and the processes on those L^*'s are dominated purely by subsequent PSD increases. Therefore the fitting of such dependencies with a two-sided Gaussian fails, at least for σ_1. However, at $L^*>4.5$ the two-sided Gaussian fitting nicely represents the median values as shown in figures in Appendix C.

The top panel of Figure 5.8 shows a summary of the fitted values of σ_1. The analysis of this data shows that the behavior of the electron PSD during the loss phase is similar to those observed in flux. That is, higher L^* reacts

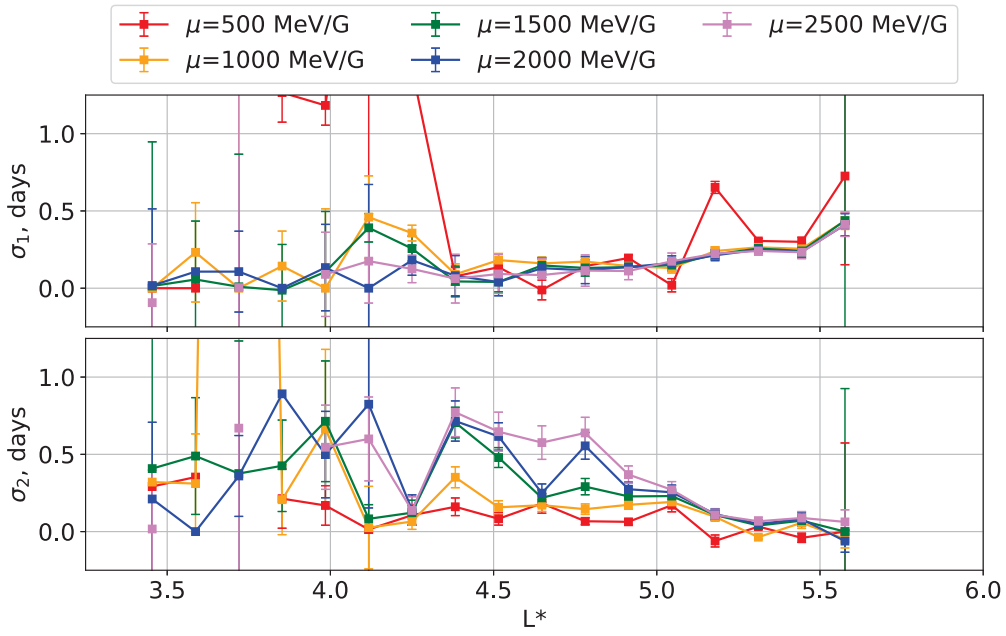

Figure 5.8: Normalized PSD fit parameters σ_1 (top panel) and σ_2 (bottom panel) as a function of L^* for different first adiabatic invariants μ. σ_1 represent the characteristic time of the loss. Meanwhile, σ_2 represent the characteristic time of recovery. The error bars were determined during the least squares fitting algorithm.

and demonstrate loss earlier than at lower L^* as represented by larger values of σ_1. This is again consistent with the signatures expected from the magnetopause shadowing where losses start first on the high L^* and move inward. Moreover, there is no apparent μ dependence suggesting that populations with different energies (and μ) react in the same manner, again consistent wiht the magnetopause shadowing loss. Nonetheless, the bottom panel of the Figure 5.8 confirms the same conclusion obtained using flux on the energy such that lower first invariants (with lower energies at the fixed magnetic field) recover faster than the higher ones. The bottom panel of Figure 5.8 also shows earlier electron PSD recovery of the higher L^*. Meaning, that when viewed in terms of PSD the recovery process happens first at higher L^* consistent with inward particle transport and acceleration of a new source population following earlier magnetopause shadowing losses.

5.4 Discussion and Conclusions

It is interesting to compare the results presented in this chapter with the results of *Morley et al.* (2010b). *Morley et al.* analyzed the response of the radiation belt associated with the impact of 67 solar wind stream interfaces on the magnetopause using a superposed epoch analysis of the electron flux measured by satellites in the GPS constellation. *Morley et al.* (2010b) showed that the dynamics of the superposed GPS flux nicely followed the locus of the compressed magnetopause, calculated using the *Shue et al.* (1998) empirical model. The selection of the events analysed in *Morley et al.* (2010b) differs from our approach. However, it is similar since a transition from a slow to fast solar wind at such interface can cause the LCDS to move inward. Moreover, the shape of the median LCDS in this research and the shape of the median *Shue et al.* (1998) standoff magnetopause distance presented by *Morley et al.* (2010b) are almost the same, but are separated by $L^*{\approx}2$ throughout the whole superposed epoch period.

Similar to our results, *Morley et al.* (2010b) observed gradual GPS flux losses starting ∼0.5-1 days prior to the arrival of the stream interfaces which is consistent with our observations of the loss timescales. *Morley et al.* interpreted their observations as arising from the loses due to the effects of outward diffusion and magnetopause shadowing. Our results further confirm this conclusion, showing that the flux and PSD at higher L^* are affected earlier, and that the loss propagates inward. Our results and those of *Morley et al.* (2010b) also both show that the ultra-relativistic electron population has similar loss patterns across the energy spectrum.

We further investigated the electron flux and PSD dynamics here and showed statistically that the losses of both flux and PSD are consistent across different energies or first adiabatic invariants with losses happening earlier at higher L^*. We conclude that during the rapid motion of the LCDS, also associated with the magnetopause compressions, that the outer radiation belt is most likely to be rapidly affected by magnetopause shadowing and the outward radial transport of particles to the compressed magnetopause.

It is also interesting to compare our results to those of *Murphy et al.* (2018) who also completed a superposed epoch study of total radiation belt content. They investigated the total radiation belt electron content calculated from Van Allen Probes phase space density in 52 magnetic storm events with SYM-H$\leq$-50 nT. Again, their events were selected differently from ours, and no emphasis placed on the outer magnetosphere boundary or LCDS in their events selection. However, the dynamics of the median IMF B_z, V_{SW}, and proton density in their storm events are very similar to those reported in this study. This suggests that the resulting shape of the LCDS in events reported by *Murphy et al.* (2018) might be similar to ours, suggesting that the results from the two analysis can be compared. *Murphy et al.* showed that the dynamics of the outer belt during loss and recovery phases in their storms are rather repeatable being characterized by fast losses and the subsequent enhancement in the outer radiation belt electron populations. We confirm these results with our analysis of magnetopause shadowing events; our results suggest further that the repeatability might be more significant than that of the recovery. The loss phase is represented by a much smaller deviation of the median from the upper and lower quartiles when analyzing both the superposed normalized flux and PSD. Meanwhile, our results show that the recovery varies more significantly. Nonetheless, the electron flux is restored to the pre-storm levels on average. The similarity in the upper and lower quartiles indicate an equal chance for the belt to be restored to levels either lower or higher than the pre-storm ones. Analysis of the PSD shows that the phase space density restores, on average, to levels greater than the pre-storm by a factor of $\sim$3, but with a large spread in the quartiles also still remaining.

Another statistical analysis of the radiation belts during the Van Allen Probes era was made by *Xiang et al.* (2018). In their study, *Xiang et al.* performed an investigation of the outer radiation belt dropouts by investigating PSD for constant μ, K, and L^*. Their analysis showed that the main phase losses occur more frequently on higher L^*. However, the intensity of the losses at hight L^* was inferred to be lower than those that occurred on the L^*<4.5. *Xiang et al.* (2018) use their result to argue that the EMIC wave scattering

is the dominant loss mechanism in low L^* regions, and that EMIC losses still play a major role at high L^* where magnetopause shadowing losses might act as well. However, in our superposed epoch studies presented here, we show that the typical loss-recovery timescale of PSD for $L^*>5$ is very fast and only $\sim$8 hours. We conclude that during magnetopause shadowing events, the Van Allen Probes with the orbital period of 8 hours, might have a hard time actually resolving losses at higher L^*. In our view, when performing a statistical analysis of the trapped radiation by investigating multiple events separately, it is likely important to have information with a higher resolution than provided by the Van Allen Probes orbits. Otherwise, under-resolution of the flux can lead to underestimation of the intensity of the losses, especially at the higher L^*. To resolve this, data from the GPS satellites could be used to provide electron flux data on high L^* with a time resolution of $\sim$30 minutes (*Morley et al.*, 2010b,a; *Tuszewski et al.*, 2004; *Morley et al.*, 2016; *Olifer et al.*, 2018b). We intended to complete such analysis in the future work.

Overall, we conclude that our investigation of the Van Allen belts using superposed epoch analysis for events where the last closed drift shell moves inward to at least L^* of 5.5 has provided tremendous additional insight to the loss processes acting in the radiation belts of the Earth. First and foremost, our analysis showed that the rapid inward motion of the LCDS is most likely to cause rapid event independent radiation belt depletion which starts at high L^* and propagates inward. This result is consistent with the paradigm of magnetopause shadowing acting in concert with fast outward radial diffusion. During the recovery phase, we show that the PSD recovered faster at higher L^*. Additionally, we show that there is an apparent energy dependence of the recovery of both flux and PSD, with lower energies (or first adiabatic invariants) recovering faster. This is consistent with suggestions made by *Mann et al.* (2018) who emphasized the possible role of radial diffusion as the primary cause of both radiation belt loss and recovery. An energy-dependent recovery of the source population at the outer boundary can explain the observed energy dependence of the flux recovery through inward radial diffusion following fast losses associated with magnetopause shadowing. We emphasize

that during the main phase of the storm, when the loss happens, the radiation belt population behaves rather self-similarly from storm to storm. This is important because it suggests that the processes causing the radiation belt depletion are not affected by the existing population and are highly repeatable.

Chapter 6

Thesis Summary and Future Plans

This thesis presents an analysis of the dynamics of the outer Van Allen belt during intense geomagnetic storms. Specifically, we focus our analysis on very fast losses associated with radiation belt extinction events and try to determine if such particle dynamics can be explained from the perspective of outward ULF wave radial diffusion and magnetopause shadowing. In Chapter 3 we performed a case study of the March 17-18, 2015 magnetic storm and focused our analysis on the magnitude of the radial diffusion coefficients. Analysis of the data-driven electric and magnetic D_{LL}^{E} and D_{LL}^{B} radial diffusion coefficients showed that their relative magnitudes might be significantly different during the main storm phase than at other times. Data from THEMIS and GOES satellites, as well as from ground-based magnetometers, revealed that during the main phase of the intense March 2015 storm the radial diffusion coefficients are not well-described by the *Ozeke et al.* (2014) empirical Kp-dependent statistical model; D_{LL}^{B} is greatly underestimated by the statistics, and D_{LL}^{E} overestimated. Moreover, our results also showed that during the main phase of the storm $D_{LL}^{E} \lesssim D_{LL}^{B}$, contrary to the statistical estimates in Kp-dependent models where the effects of D_{LL}^{B} are usually neglected. Thus, using the *Ozeke et al.* (2014) parametrization to represent the diffusion coefficients for radial diffusion simulations may lead to underestimation of the total D_{LL} coefficient during the main phase and the wrong rates of diffusion in simulations. We also argue that the strong discrepancy between the event-specific

and statistically estimated radial diffusion coefficients is largest during periods of strong southward interplanetary magnetic field. Therefore, some changes to the current empirical models for radial diffusion coefficients should likely be made to more accurately reproduce the rates of diffusion. This might be especially important for modeling extremely fast losses associated with magnetopause shadowing and outward ULF wave radial diffusion.

Additionally, in Chapter 3 we performed an analysis of the energy dependence of the ULF wave radial diffusion coefficients D_{LL}^{B} and D_{LL}^{E}. Our results showed that the D_{LL}^{B} coefficient appears to be rather energy coherent, i.e., with more significant changes happening as a function of time than energy. Meanwhile, the D_{LL}^{E} coefficient has only a slight energy dependence during the main phase of the storm. Both of these results are in general consistent with recent magnetohydrodynamic (MHD) simulations (e.g., *Li et al.*, 2016, 2017). However, the magnitudes of the data-specific magnetic radial diffusion coefficients that we obtained remain strongly underestimated in MHD simulations of the main phase of this storm, perhaps because the simulation fail to accurately represent all of the ULF wave excitation associated with strong southward IMF during the main phase on the magnetic storm.

Chapter 4 focuses on case studies of four different geomagnetic storms which all show signs of fast radiation belt depletion, sometimes referred to as radiation belt extinction (e.g., *Ozeke et al.*, 2017). We studied the March 2013, March 2015, September 2012, and September 2014 magnetic storms by analyzing the electron differential flux data from the GPS constellation of satellites in the context of the location of the last closed drift shell. We argued that magnetopause shadowing is most probably the cause of the rapid loss during all of these storms. Also, we emphasized that when assessing magnetopause shadowing losses in the Van Allen radiation belts analyzing the last closed drift shell and working in L* space is more reasonable than regarding a classical *Shue et al.* (1998) model of magnetopause standoff distance in terms of Earth radii as the L-shell where shadowing losses occur. Additionally, in Chapter 4, we compared the results of the neural network LANL* and full calculation of the LCDS for the March 2013 geomagnetic storm. The comparison showed

that both approaches agree at least for this storm, suggesting that even during conditions of strongly southward IMF ($B_z \approx -15$ nT) the neural network produces a reasonable LCDS location and that the LANL* routine can be used to quickly estimate the location of the LCDS over a long period of time with high time resolution while using only modest computational resources.

In Chapter 5 we used the location of the last closed drift shell, calculated using the LANL* neural network, to select isolated geomagnetic storms during which the LCDS dropped below L^* of 5.8. We then performed a superposed epoch analysis of the radiation belt flux dynamics, organized by the time of minimum LCDS L^* location. Based on electron flux and derived electron phase space density (PSD) from the Van Allen Probes during 64 selected geomagnetic storms, we not only confirmed that magnetopause shadowing losses are most likely to occur when the LCDS rapidly moves in, but also that the loss phase has substantial self-similarity from storm to storm. Moreover, we show for the first time that electron recovery, after the radiation belt population has been lost to the magnetosheath, has an apparent energy dependence with lower energies recovering faster. This result was inferred by *Mann et al.* (2018) in radial diffusion simulations when analyzing the losses and recovery of electrons observed in the September 2012 storm. Moreover, we emphasize that the PSD data from the Van Allen Probes should be used with care when addressing the very fast dynamics of trapped electron radiation due to the limitations of monitoring imposed by the orbital period of the Probes. According to our superposed epoch analysis, the typical recovery times are smaller with larger L*, meaning that during intense storms the electron population on L*>5 can be lost and recovered inbetween two subsequent Van Allen Probes passes.

Overall, this thesis emphasizes the importance of radial diffusion and magnetopause shadowing for the losses of the highly energetic electron population in the outer Van Allen radiation belt of the Earth. Our results show that the signatures of magnetopause shadowing losses and the outward ULF wave radial diffusion of electrons to a compressed magnetopause are present in many geomagnetic storms. Our results suggest that a relatively simple model of such particle loss to the magnetosheath with the subsequent recovery and in-

ward particle motion and acceleration can provide a fairly good description of the electron dynamics in the outer belt in a large number of all geomagnetic storms. However, to reproduce the very fast losses associated with radiation belt extinction events and use this radial diffusion paradigm in more complicated tasks, e.g., space weather prediction, some changes to the current empirical models for the rates of radial diffusion should be made.

6.1 Future Research Plans

First, we are planning to continue working on the superposed epoch analysis to investigate the average response of the trapped electron radiation for different pitch angles, α, and second invariants, K. We are also planning to repeat and extend this study using electron flux data from the GPS satellites. Investigation of different second invariants can provide more insight into the average electron population response during magnetopause shadowing events. Meanwhile, adding electron flux data from GPS satellite constellation which has much higher time resolution that available from the Van Allen Probes can improve both the temporal resolution and the statistics of superposed belt dynamics.

Second, we are planning to investigate different approaches for calculating electron PSD. Currently, different space physics research groups use different methods and different magnetospheric models for this calculation. However, these approaches do not always produce consistent results. We are aiming to analyze this discrepancy and look for reasons that could have caused it. In this research, we will also investigate methods of deriving PSD from electron flux data which is not actually pitch angle resolved. The latter will provide the possibility of the PSD calculation from multiple satellite missions, e.g., GPS.

Lastly, we plan to continue using or developing cutting-edge computational techniques in our space physics research and validating them. The current success with the neural network approach for calculating L^* and the LCDS suggests that developing models based on machine learning can help in revealing some of the complicated dependencies between driving solar wind and the

Earth's magnetospheric response. For example, it could be used to produce a new parametrization of the radial diffusion coefficients, perhaps dependent on the conditions or parameters such as magnetic local time, IMF, solar wind speed, etc. – the need for the development of which was emphasized in the results presented in this thesis.

Bibliography

Akasofu, S. I., and S. Chapman (1973), Solar-terrestrial physics, *Quarterly Journal of the Royal Meteorological Society*, *99*(422), 793–793, doi:10.1002/qj.49709942230.

Albert, J. M. (2005), Evaluation of quasi-linear diffusion coefficients for whistler mode waves in a plasma with arbitrary density ratio, *Journal of Geophysical Research: Space Physics*, *110*(A3), doi:10.1029/2004JA010844, a03218.

Albert, J. M., R. S. Selesnick, S. K. Morley, M. G. Henderson, and A. C. Kellerman (2018), Calculation of last closed drift shells for the 2013 GEM radiation belt challenge events, *Journal of Geophysical Research: Space Physics*, doi:10.1029/2018ja025991.

Alves, L. R., L. A. Da Silva, V. M. Souza, D. G. Sibeck, P. R. Jauer, L. E. A. Vieira, B. M. Walsh, M. V. D. Silveira, J. P. Marchezi, M. Rockenbach, A. D. Lago, O. Mendes, B. T. Tsurutani, D. Koga, S. G. Kanekal, D. N. Baker, J. R. Wygant, and C. A. Kletzing (2016), Outer radiation belt dropout dynamics following the arrival of two interplanetary coronal mass ejections, *Geophysical Research Letters*, *43*(3), 978–987, doi:10.1002/2015GL067066, 2015GL067066.

Angelopoulos, V. (2008), The THEMIS mission, *Space Science Reviews*, *141*(1-4), 5–34, doi:10.1007/s11214-008-9336-1.

Auster, H. U., K. H. Glassmeier, W. Magnes, O. Aydogar, W. Baumjohann, D. Constantinescu, D. Fischer, K. H. Fornacon, E. Georgescu, P. Harvey, O. Hillenmaier, R. Kroth, M. Ludlam, Y. Narita, R. Nakamura, K. Okrafka, F. Plaschke, I. Richter, H. Schwarzl, B. Stoll, A. Valavanoglou, and M. Wiedemann (2008), The THEMIS Fluxgate Magnetometer, *Space Science Reviews*, *141*(1), 235–264, doi:10.1007/s11214-008-9365-9.

Baker, D. N., S. G. Kanekal, X. Li, S. P. Monk, J. Goldstein, and J. L. Burch (2004), An extreme distortion of the van allen belt arising from the Halloween solar storm in 2003, *Nature*, *432*, 878.

Baker, D. N., S. G. Kanekal, V. C. Hoxie, S. Batiste, M. Bolton, X. Li, S. R. Elkington, S. Monk, R. Reukauf, S. Steg, J. Westfall, C. Belting, B. Bolton, D. Braun, B. Cervelli, K. Hubbell, M. Kien, S. Knappmiller, S. Wade, B. Lamprecht, K. Stevens, J. Wallace, A. Yehle, H. E. Spence, and R. Friedel (2013a), The relativistic electron-proton telescope (REPT) instrument on board the radiation belt storm probes (RBSP) spacecraft: Characterization of Earth's radiation belt high-energy particle populations, *Space Science Reviews*, *179*(1), 337–381, doi:10.1007/s11214-012-9950-9.

Baker, D. N., S. G. Kanekal, V. C. Hoxie, M. G. Henderson, X. Li, H. E. Spence, S. R. Elkington, R. H. W. Friedel, J. Goldstein, M. K. Hudson, G. D. Reeves, R. M. Thorne, C. A. Kletzing, and S. G. Claudepierre (2013b), A Long-Lived Relativistic Electron Storage Ring Embedded in Earth's Outer Van Allen Belt, *Science*, *340*(6129), 186–190, doi:10.1126/science.1233518.

Baker, D. N., A. N. Jaynes, X. Li, M. G. Henderson, S. G. Kanekal, G. D. Reeves, H. E. Spence, S. G. Claudepierre, J. F. Fennell, M. K. Hudson, R. M. Thorne, J. C. Foster, P. J. Erickson, D. M. Malaspina, J. R. Wygant, A. Boyd, C. A. Kletzing, A. Drozdov, and Y. Y. Shprits (2014), Gradual diffusion and punctuated phase space density enhancements of highly relativistic electrons: Van allen probes observations, *Geophysical Research Letters*, *41*(5), 1351–1358, doi:10.1002/2013GL058942, 2013GL058942.

Baker, D. N., A. N. Jaynes, S. G. Kanekal, J. C. Foster, P. J. Erickson, J. F. Fennell, J. B. Blake, H. Zhao, X. Li, S. R. Elkington, M. G. Henderson, G. D. Reeves, H. E. Spence, C. A. Kletzing, and J. R. Wygant (2016), Highly relativistic radiation belt electron acceleration, transport, and loss: Large solar storm events of march and june 2015, *Journal of Geophysical Research: Space Physics*, *121*(7), 6647–6660, doi:10.1002/2016JA022502, 2016JA022502.

Bentley, S. N., C. E. J. Watt, M. J. Owens, and I. J. Rae (2018), ULF wave activity in the magnetosphere: Resolving solar wind interdependencies to identify driving mechanisms, *Journal of Geophysical Research: Space Physics*, *123*(4), 2745–2771, doi:10.1002/2017ja024740.

Blake, J. B., P. A. Carranza, S. G. Claudepierre, J. H. Clemmons, W. R. Crain, Y. Dotan, J. F. Fennell, F. H. Fuentes, R. M. Galvan, J. S. George, M. G. Henderson, M. Lalic, A. Y. Lin, M. D. Looper, D. J. Mabry, J. E. Mazur, B. McCarthy, C. Q. Nguyen, T. P. O'Brien, M. A. Perez, M. T. Redding, J. L. Roeder, D. J. Salvaggio, G. A. Sorensen, H. E. Spence, S. Yi, and M. P. Zakrzewski (2013), The magnetic electron ion spectrometer (MagEIS) instruments aboard the radiation belt storm probes (RBSP) spacecraft, *Space Science Reviews*, *179*(1-4), 383–421, doi:10.1007/s11214-013-9991-8.

Bonnell, J. W., F. S. Mozer, G. T. Delory, A. J. Hull, R. E. Ergun, C. M. Cully, V. Angelopoulos, and P. R. Harvey (2008), The Electric Field Instrument (EFI) for THEMIS, *Space Science Reviews*, *141*(1), 303–341, doi:10.1007/s11214-008-9469-2.

Brito, T. V., and S. K. Morley (2017), Improving empirical magnetic field models by fitting to in situ data using an optimized parameter approach, *Space Weather*, *15*(12), 1628–1648, doi:10.1002/2017sw001702.

Brizard, A. J., and A. A. Chan (2001), Relativistic bounce-averaged quasilinear diffusion equation for low-frequency electromagnetic fluctuations, *Physics of Plasmas*, *8*(11), 4762–4771, doi:10.1063/1.1408623.

Chen, Y. (2005), Multisatellite determination of the relativistic electron phase space density at geosynchronous orbit: Methodology and results during geomagnetically quiet times, *Journal of Geophysical Research*, *110*(A10), doi:10.1029/2004ja010895.

Connors, M., I. Schofield, K. Reiter, P. J. Chi, K. M. Rowe, and C. T. Russell (2016), The AUTUMNX magnetometer meridian chain in Québec, Canada, *Earth, Planets and Space*, *68*(1), doi:10.1186/s40623-015-0354-4.

Cravens, T. (2004), *Physics of Solar System Plasmas*, Cambridge Atmospheric and Space Science Series, Cambridge University Press.

Dimitrakoudis, S., I. R. Mann, G. Balasis, C. Papadimitriou, A. Anastasiadis, and I. A. Daglis (2015), Accurately specifying storm-time ULF wave radial diffusion in the radiation belts, *Geophysical Research Letters*, *42*(14), 5711–5718, doi:10.1002/2015gl064707.

Dungey, J. W. (1961), Interplanetary magnetic field and the auroral zones, *Physical Review Letters*, *6*(2), 47–48, doi:10.1103/physrevlett.6.47.

Elkington, S. R., and T. E. Sarris (2016), The role of Pc-5 ULF waves in the radiation belts: Current understanding and open questions, in *Waves, Particles, and Storms in Geospace*, edited by G. Balasis, I. A. Daglis, and I. R. Mann, chap. 4, pp. 80–101, Oxford University Press, Oxford, doi:10.1093/acprof:oso/9780198705246.001.0001.

Fei, Y., A. A. Chan, S. R. Elkington, and M. J. Wiltberger (2006), Radial diffusion and MHD particle simulations of relativistic electron transport by ULF waves in the september 1998 storm, *Journal of Geophysical Research*, *111*(A12), doi:10.1029/2005ja011211.

Fraser, B., S. Morley, R. Grew, and H. Singer (2013), Classification of Pc1-2 Electromagnetic Ion Cyclotron waves at geosynchronous orbit, in *Dynamics of the Earth Radiation Belts and Inner Magnetosphere*, pp. 53–68, American Geophysical Union, doi:10.1029/2012gm001353.

Friedel, R., G. Reeves, and T. Obara (2002), Relativistic electron dynamics in the inner magnetosphere – a review, *Journal of Atmospheric and Solar-Terrestrial Physics*, *64*(2), 265 – 282, doi:https://doi.org/10.1016/S1364-6826(01)00088-8, sTEP-Results, Applications and Modelling Phase (S-RAMP).

Glatzmaier, G. A., and P. H. Roberts (1995), A three-dimensional convective dynamo solution with rotating and finitely conducting inner core and mantle, *Physics of the Earth and Planetary Interiors*, *91*(1-3), 63–75, doi:10.1016/0031-9201(95)03049-3.

Golub, L. (2010), *The solar corona*, Cambridge University Press, Cambridge, UK New York.

Henderson, M., S. Morley, J. Niehof, and B. Larsen (2017), drsteve/lanlgeomag: Lanlgeomag v.1.5.15-alpha, doi:10.5281/zenodo.1133782.

Horne, R. B., R. M. Thorne, S. A. Glauert, J. M. Albert, N. P. Meredith, and R. R. Anderson (2005), Timescale for radiation belt electron acceleration by whistler mode chorus waves, *Journal of Geophysical Research: Space Physics*, *110*(A3), doi:10.1029/2004JA010811, a03225.

Hughes, W. J. (1995), The magnetopause, magnetotail, and magnetic reconection, in *Introduction to Space Physics*, edited by M. G. Kivelson and C. T. Russell, Cambridge atmospheric and space science series, chap. 9, pp. 227–287, Cambridge University Press, Cambridge.

Hundhausen, A. J. (1972), *Coronal Expansion and Solar Wind*, Springer Berlin Heidelberg, doi:10.1007/978-3-642-65414-5.

Kang, S. B., M. C. Fok, A. Glocer, K. W. Min, C. R. Choi, E. Choi, and J. Hwang (2016), Simulation of a rapid dropout event for highly relativistic electrons with the RBE model, *Journal of Geophysical Research: Space Physics*, *121*(5), 4092–4102, doi:10.1002/2015JA021966, 2015JA021966.

Kersten, T., R. B. Horne, S. A. Glauert, N. P. Meredith, B. J. Fraser, and R. S. Grew (2014), Electron losses from the radiation belts caused by EMIC waves, *Journal of Geophysical Research: Space Physics*, *119*(11), 8820–8837, doi:10.1002/2014JA020366.

King, J. H. (2005), Solar wind spatial scales in and comparisons of hourly wind and ACE plasma and magnetic field data, *Journal of Geophysical Research*, *110*(A2), doi:10.1029/2004ja010649.

Kivelson, M. G. (1995), Physics of space plasma, in *Introduction to Space Physics*, edited by M. G. Kivelson and C. T. Russell, Cambridge atmospheric and space science series, chap. 2, pp. 27–57, Cambridge University Press, Cambridge.

Koller, J., G. D. Reeves, and R. H. W. Friedel (2009), Lanl* v1.0: a radiation belt drift shell model suitable for real-time and reanalysis applications, *Geoscientific Model Development*, *2*(2), 113–122, doi:10.5194/gmd-2-113-2009.

Kuang, W., and J. Bloxham (1997), An earth-like numerical dynamo model, *Nature*, *389*(6649), 371–374, doi:10.1038/38712.

Landau, L., and E. Lifshitz (1976), The canonical equations, in *Mechanics*, pp. 131–167, Elsevier, doi:10.1016/b978-0-08-050347-9.50012-5.

Lee, J., K. Min, and K. Kim (2013), Characteristic dimension of electromagnetic ion cyclotron wave activity in the magnetosphere, *Journal of Geophysical Research: Space Physics*, *118*(4), 1651–1658, doi:10.1002/jgra.50242.

Li, W., R. M. Thorne, Q. Ma, B. Ni, J. Bortnik, D. N. Baker, H. E. Spence, G. D. Reeves, S. G. Kanekal, J. C. Green, C. A. Kletzing, W. S. Kurth, G. B. Hospodarsky, J. B. Blake, J. F. Fennell, and S. G. Claudepierre (2014), Radiation belt electron acceleration by chorus waves during the 17 march 2013 storm, *Journal of Geophysical Research: Space Physics*, *119*(6), 4681–4693, doi:10.1002/2014ja019945.

Li, X., D. N. Baker, M. Temerin, T. E. Cayton, E. G. D. Reeves, R. A. Christensen, J. B. Blake, M. D. Looper, R. Nakamura, and S. G. Kanekal (1997), Multisatellite observations of the outer zone electron variation during the november 3-4, 1993, magnetic storm, *Journal of Geophysical Research: Space Physics*, *102*(A7), 14,123–14,140, doi:10.1029/97ja01101.

Li, Z., M. Hudson, J. Paral, M. Wiltberger, and D. Turner (2016), Global ULF wave analysis of radial diffusion coefficients using a global MHD model for the 17 March 2015 storm, *Journal of Geophysical Research: Space Physics*, *121*(7), 6196–6206, doi:10.1002/2016JA022508.

Li, Z., M. Hudson, M. Patel, M. Wiltberger, A. Boyd, and D. Turner (2017), ULF wave analysis and radial diffusion calculation using a global MHD model for the 17 March 2013 and 2015 storms, *Journal of Geophysical Research: Space Physics*, *122*(7), 7353–7363, doi:10.1002/2016JA023846.

Loto'aniu, T. M., H. J. Singer, C. L. Waters, V. Angelopoulos, I. R. Mann, S. R. Elkington, and J. W. Bonnell (2010), Relativistic electron loss due to ultralow frequency waves and enhanced outward radial diffusion, *Journal of Geophysical Research: Space Physics*, *115*(A12), doi:10.1029/2010JA015755, a12245.

Luhmann, J. G. (1995), Plasma interactions with unmagnetized bodies, in *Introduction to Space Physics*, edited by M. G. Kivelson and C. T. Russell, Cambridge atmospheric and space science series, chap. 8, pp. 203–225, Cambridge University Press, Cambridge.

Mann, I. R., and L. G. Ozeke (2016), How quickly, how deeply, and how strongly can dynamical outer boundary conditions impact Van Allen radiation belt morphology?, *Journal of Geophysical Research: Space Physics*, *121*(6), 5553–5558, doi:10.1002/2016JA022647, 2016JA022647.

Mann, I. R., D. K. Milling, I. J. Rae, L. G. Ozeke, A. Kale, Z. C. Kale, K. R. Murphy, A. Parent, M. Usanova, D. M. Pahud, E. A. Lee, V. Amalraj, D. D. Wallis, V. Angelopoulos, K. H. Glassmeier, C. T. Russell, H. U. Auster, and H. J. Singer (2008), The Upgraded CARISMA Magnetometer Array in the THEMIS Era, *Space Science Reviews*, *141*(1), 413–451, doi:10.1007/s11214-008-9457-6.

Mann, I. R., L. G. Ozeke, K. R. Murphy, S. G. Claudepierre, D. L. Turner, D. N. Baker, I. J. Rae, A. Kale, D. K. Milling, A. J. Boyd, H. E. Spence, G. D. Reeves, H. J. Singer, S. Dimitrakoudis, I. A. Daglis, and F. Honary (2016), Explaining the dynamics of the ultra-relativistic third Van Allen radiation belt, *Nature Physics*, *12*, 978–983, doi:10.1038/nphys3799.

Mann, I. R., L. G. Ozeke, S. K. Morley, K. R. Murphy, S. G. Claudepierre, D. L. Turner, D. N. Baker, I. J. Rae, A. Kale, D. K. Milling, A. J. Boyd, H. E. Spence, H. J. Singer, S. Dimitrakoudis, I. A. Daglis, and F. Honary (2018), Reply to 'The dynamics of Van Allen belts revisited', *Nature Physics*, *14*(2), 103–104, doi:10.1038/nphys4351.

McCollough, J. P., S. R. Elkington, and D. N. Baker (2012), The role of Shabansky orbits in compression related electromagnetic ion cyclotron wave growth, *Journal of Geophysical Research: Space Physics*, *117*(A1), doi:10.1029/2011JA016948.

McComas, D. J., B. L. Barraclough, H. O. Funsten, J. T. Gosling, E. Santiago-Muñoz, R. M. Skoug, B. E. Goldstein, M. Neugebauer, P. Riley, and A. Balogh (2002), Solar wind observations over ulysses' first full polar orbit, *Journal of Geophysical Research: Space Physics*, *105*(A5), 10,419–10,433, doi:10.1029/1999JA000383.

McIlwain, C. E. (1961), Coordinates for mapping the distribution of magnetically trapped particles, *Journal of Geophysical Research*, *66*(11), 3681–3691, doi:10.1029/jz066i011p03681.

Morley, S. K., R. H. W. Friedel, T. E. Cayton, and E. Noveroske (2010a), A rapid, global and prolonged electron radiation belt dropout observed with the Global Positioning System constellation, *Geophysical Research Letters*, *37*(6), doi:10.1029/2010gl042772.

Morley, S. K., R. H. W. Friedel, E. L. Spanswick, G. D. Reeves, J. T. Steinberg, J. Koller, T. Cayton, and E. Noveroske (2010b), Dropouts of the outer electron radiation belt in response to solar wind stream interfaces: global positioning system observations, *Proceedings of the Royal Society of London A: Mathematical, Physical and Engineering Sciences*, *466*(2123), 3329–3350, doi:10.1098/rspa.2010.0078.

Morley, S. K., J. Koller, D. T. Welling, B. A. Larsen, M. G. Henderson, and J. T. Niehof (2011), Spacepy - a python-based library of tools for the space sciences, in *Proceedings of the 9th Python in science conference (SciPy 2010)*, Austin, TX.

Morley, S. K., M. G. Henderson, G. D. Reeves, R. H. W. Friedel, and D. N. Baker (2013), Phase space density matching of relativistic electrons using the van allen probes: Rept results, *Geophysical Research Letters*, *40*(18), 4798–4802, doi:10.1002/grl.50909.

Morley, S. K., J. P. Sullivan, M. G. Henderson, J. B. Blake, and D. N. Baker (2016), The Global Positioning System constellation as a space weather monitor: Comparison of electron measurements with Van Allen Probes data, *Space Weather*, *14*(2), 76–92, doi:10.1002/2015sw001339.

Morley, S. K., J. P. Sullivan, M. R. Carver, R. M. Kippen, R. H. W. Friedel, G. D. Reeves, and M. G. Henderson (2017), Energetic particle data from the Global Positioning System constellation, *Space Weather*, *15*(2), 283–289, doi:10.1002/2017sw001604.

Murphy, K. R., I. R. Mann, and D. G. Sibeck (2015), On the dependence of storm time ulf wave power on magnetopause location: Impacts for ulf wave radial diffusion, *Geophysical Research Letters*, *42*(22), 9676–9684, doi:10.1002/2015GL066592, 2015GL066592.

Murphy, K. R., C. E. J. Watt, I. R. Mann, I. J. Rae, D. G. Sibeck, A. J. Boyd, C. F. Forsyth, D. L. Turner, S. G. Claudepierre, D. N. Baker, H. E. Spence, G. D. Reeves, J. B. Blake, and J. Fennell (2018), The global statistical response of the outer radiation belt during geomagnetic storms, *Geophysical Research Letters*, *45*(9), 3783–3792, doi:10.1002/2017gl076674.

Northrop, T. G. (1963), Adiabatic charged-particle motion, *Reviews of Geophysics*, *1*(3), 283, doi:10.1029/rg001i003p00283.

Olifer, L., I. R. Mann, L. G. Ozeke, I. J. Rae, and S. K. Morley (2018a), On the relative strength of electric and magnetic ulf wave radial diffusion during the march 2015 geomagnetic storm, *Under rewiev in Journal of Geophysical Research: Space Physics*.

Olifer, L., I. R. Mann, S. K. Morley, L. G. Ozeke, and D. Choi (2018b), On the role of last closed drift shell dynamics in driving fast losses and van allen radiation belt extinction, *Journal of Geophysical Research: Space Physics*, doi:10.1029/2018JA025190.

Omura, Y., N. Furuya, and D. Summers (2007), Relativistic turning acceleration of resonant electrons by coherent whistler mode waves in a dipole magnetic field, *Journal of Geophysical Research: Space Physics*, *112*(A6), doi:10.1029/2006JA012243, a06236.

Oppenheim, A. V., R. W. Schafer, and J. R. Buck (1999), *Discrete-time Signal Processing (2Nd Ed.)*, Prentice-Hall, Inc., Upper Saddle River, NJ, USA.

Ozeke, L. G., I. R. Mann, and J. I. Rae (2009), Mapping guided Alfvén wave magnetic field amplitudes observed on the ground to equatorial electric field amplitudes in space, *Journal of Geophysical Research: Space Physics*, *114*(A1), doi:10.1029/2008JA013041.

Ozeke, L. G., I. R. Mann, K. R. Murphy, J. I. Rae, and D. K. Milling (2014), Analytic expressions for ULF wave radiation belt radial diffusion coefficients, *Journal of Geophysical Research: Space Physics*, *119*(3), 1587–1605, doi:10.1002/2013JA019204, 2013JA019204.

Ozeke, L. G., I. R. Mann, K. R. Murphy, D. G. Sibeck, and D. N. Baker (2017), Ultra-relativistic radiation belt extinction and ULF wave radial diffusion: Modeling the September 2014 extended dropout event, *Geophysical Research Letters*, *44*(6), 2624–2633, doi:10.1002/2017GL072811.

Parker, E. N. (1958), Dynamics of the interplanetary gas and magnetic fields., *The Astrophysical Journal*, *128*, 664, doi:10.1086/146579.

Pokhotelov, D., I. J. Rae, K. R. Murphy, I. R. Mann, and L. Ozeke (2016), Effects of ULF wave power on relativistic radiation belt electrons: 8-9 October 2012 geomagnetic storm, *Journal of Geophysical Research: Space Physics*, *121*(12), 11,766–11,779, doi:10.1002/2016JA023130, 2016JA023130.

Priest, E. R. (1995), The Sun and its magnetohydrodynamics, in *Introduction to Space Physics*, edited by M. G. Kivelson and C. T. Russell, Cambridge atmospheric and space science series, chap. 3, pp. 58–89, Cambridge University Press, Cambridge.

Reeves, G. D., K. L. McAdams, R. H. W. Friedel, and T. P. O'Brien (2003), Acceleration and loss of relativistic electrons during geomagnetic storms, *Geophysical Research Letters*, *30*(10), doi:10.1029/2002gl016513.

Roederer, J. G. (1970), *Dynamics of Geomagnetically Trapped Radiation*, Springer Berlin Heidelberg, doi:10.1007/978-3-642-49300-3.

Russell, C. (1995), Brief history of solar terrestrial physics, in *Introduction to Space Physics*, edited by M. Kivelson and C. Russell, Cambridge atmospheric and space science series, chap. 1, pp. 1–26, Cambridge University Press, Cambridge.

Sawyer, D. M., and J. I. Vette (1976), AP-8 trapped proton environment for solar maximum and solar minimum, *NASA STI/Recon Technical Report N*, *77*.

Schiller, Q., W. Tu, A. F. Ali, X. Li, H. C. Godinez, D. L. Turner, S. K. Morley, and M. G. Henderson (2016), Simultaneous event-specific estimates of transport, loss, and source rates for relativistic outer radiation belt electrons, *Journal of Geophysical Research: Space Physics*, *122*(3), 3354–3373, doi:10.1002/2016JA023093.

Schulz, M., and L. J. Lanzerotti (1974), *Particle Diffusion in the Radiation Belts*, Springer Berlin Heidelberg, doi:10.1007/978-3-642-65675-0.

Shprits, Y. Y., R. M. Thorne, R. Friedel, G. D. Reeves, J. Fennell, D. N. Baker, and S. G. Kanekal (2006), Outward radial diffusion driven by losses at magnetopause, *Journal of Geophysical Research: Space Physics*, *111*(A11), doi:10.1029/2006JA011657, a11214.

Shprits, Y. Y., N. P. Meredith, and R. M. Thorne (2007), Parameterization of radiation belt electron loss timescales due to interactions with chorus waves, *Geophysical Research Letters*, *34*(11), doi:10.1029/2006GL029050, l11110.

Shprits, Y. Y., D. A. Subbotin, N. P. Meredith, and S. R. Elkington (2008), Review of modeling of losses and sources of relativistic electrons in the outer radiation belt II: Local acceleration and loss, *Journal of Atmospheric and Solar-Terrestrial Physics*, *70*(14), 1694 – 1713, doi:https://doi.org/10.1016/j.jastp.2008.06.014, dynamic Variability of Earth's Radiation Belts.

Shprits, Y. Y., D. Subbotin, A. Drozdov, M. E. Usanova, A. Kellerman, K. Orlova, D. N. Baker, D. L. Turner, and K.-C. Kim (2013), Unusual stable trapping of the ultrarelativistic electrons in the Van Allen radiation belts, *Nature Physics*, *9*(11), 699–703, doi:10.1038/nphys2760.

Shprits, Y. Y., A. Y. Drozdov, M. Spasojevic, A. C. Kellerman, M. E. Usanova, M. J. Engebretson, O. V. Agapitov, I. S. Zhelavskaya, T. J. Raita, H. E. Spence, D. N. Baker, H. Zhu, and N. A. Aseev (2016), Wave-induced loss of ultra-relativistic electrons in the Van Allen radiation belts, *Nature Communications*, *7*, 12,883, doi:10.1038/ncomms12883.

Shprits, Y. Y., R. B. Horne, A. C. Kellerman, and A. Y. Drozdov (2018), The dynamics of Van Allen belts revisited, *Nature Physics*, *14*(2), 102–103, doi:10.1038/nphys4350.

Shue, J. H., P. Song, C. T. Russell, J. T. Steinberg, J. K. Chao, G. Zastenker, O. L. Vaisberg, S. Kokubun, H. J. Singer, T. R. Detman, and H. Kawano (1998), Magnetopause location under extreme solar wind conditions, *Journal of Geophysical Research: Space Physics*, *103*(A8), 17,691–17,700, doi:10.1029/98JA01103.

Singer, H., L. Matheson, R. Grubb, A. Newman, and D. Bouwer (1996), Monitoring space weather with the GOES magnetometers, in *GOES-8 and Beyond*, edited by E. R. Washwell, SPIE, doi:10.1117/12.254077.

Spence, H. E., G. D. Reeves, D. N. Baker, J. B. Blake, M. Bolton, S. Bourdarie, A. A. Chan, S. G. Claudepierre, J. H. Clemmons, J. P. Cravens, S. R. Elkington, J. F. Fennell, R. H. W. Friedel, H. O. Funsten, J. Goldstein, J. C. Green, A. Guthrie, M. G. Henderson, R. B. Horne, M. K. Hudson, J. M. Jahn, V. K. Jordanova, S. G. Kanekal, B. W. Klatt, B. A. Larsen, X. Li, E. A. MacDonald, I. R. Mann, J. Niehof, T. P. O'Brien, T. G. Onsager, D. Salvaggio, R. M. Skoug, S. S. Smith, L. L. Suther, M. F. Thomsen, and R. M. Thorne (2013), Science goals and overview of the radiation belt storm probes (rbsp) energetic particle, composition, and thermal plasma (ect) suite on nasa's van allen probes mission, *Space Science Reviews*, *179*(1), 311–336, doi:10.1007/s11214-013-0007-5.

Spence, H. E., G. D. Reeves, and R. Kessel (2016), An overview of early results from the radiation belt storm probes energetic particle, composition, and thermal plasma suite on NASA's Van Allen Probes mission, in *Waves, Particles, and Storms in Geospace*, edited by G. Balasis, I. A. Daglis, and I. R. Mann, chap. 17, pp. 425–442, Oxford University Press, Oxford, doi: 10.1093/acprof:oso/9780198705246.001.0001.

Thébault, E., C. C. Finlay, C. D. Beggan, P. Alken, J. Aubert, O. Barrois, F. Bertrand, T. Bondar, A. Boness, L. Brocco, E. Canet, A. Chambodut, A. Chulliat, P. Coïsson, F. Civet, A. Du, A. Fournier, I. Fratter, N. Gillet, B. Hamilton, M. Hamoudi, G. Hulot, T. Jager, M. Korte, W. Kuang, X. Lalanne, B. Langlais, J.-M. Léger, V. Lesur, F. J. Lowes, S. Macmillan, M. Mandea, C. Manoj, S. Maus, N. Olsen, V. Petrov, V. Ridley, M. Rother, T. J. Sabaka, D. Saturnino, R. Schachtschneider, O. Sirol, A. Tangborn, A. Thomson, L. Tøffner-Clausen, P. Vigneron, I. Wardinski, and T. Zvereva (2015), International geomagnetic reference field: the 12th generation, *Earth, Planets and Space*, *67*(1), 79, doi:10.1186/s40623-015-0228-9.

Thorne, R. M., E. J. Smith, R. K. Burton, and R. E. Holzer (1973), Plasmaspheric hiss, *Journal of Geophysical Research*, *78*(10), 1581–1596, doi: 10.1029/JA078i010p01581.

Thorne, R. M., W. Li, B. Ni, Q. Ma, J. Bortnik, L. Chen, D. N. Baker, H. E. Spence, G. D. Reeves, M. G. Henderson, C. A. Kletzing, W. S. Kurth, G. B. Hospodarsky, J. B. Blake, J. F. Fennell, S. G. Claudepierre, and S. G. Kanekal (2013), Rapid local acceleration of relativistic radiation-belt electrons by magnetospheric chorus, *Nature*, *504*(7480), 411–414, doi:10.1038/nature12889.

Tsyganenko, N. A., and M. I. Sitnov (2005), Modeling the dynamics of the inner magnetosphere during strong geomagnetic storms, *Journal of Geophysical Research: Space Physics*, *110*(A3), doi:10.1029/2004JA010798, a03208.

Turner, D. L., Y. Shprits, M. Hartinger, and V. Angelopoulos (2012), Explaining sudden losses of outer radiation belt electrons during geomagnetic storms, *Nature Physics*, *8*, 208 EP–.

Tuszewski, M., T. E. Cayton, J. C. Ingraham, and R. M. Kippen (2004), Bremsstrahlung effects in energetic particle detectors, *Space Weather*, *2*(10), doi:10.1029/2003SW000057, s10S01.

Ukhorskiy, A. Y., M. I. Sitnov, R. M. Millan, and B. T. Kress (2011), The role of drift orbit bifurcations in energization and loss of electrons in the outer radiation belt, *Journal of Geophysical Research: Space Physics*, *116*(A9), doi:10.1029/2011JA016623, a09208.

Van Allen, J. A., and L. A. Frank (1959), Radiation around the earth to a radial distance of 107400 km., *Nature*, *183*(430), doi:10.1038/183430a0.

Vette, J. I. (1991), The AE-8 trapped electron model environment, *NASA STI/Recon Technical Report N*, *92*.

Walker, R. J., and C. T. Russel (1995), Solar-wind interactions with magnetized plannets, in *Introduction to Space Physics*, edited by M. G. Kivelson and C. T. Russell, Cambridge atmospheric and space science series, chap. 6, pp. 164–181, Cambridge University Press, Cambridge.

Walt, M. (1994), *Introduction to Geomagnetically Trapped Radiation*, Cambridge University Press, doi:10.1017/cbo9780511524981.

Xiang, Z., W. Tu, X. Li, B. Ni, S. K. Morley, and D. N. Baker (2017), Understanding the mechanisms of radiation belt dropouts observed by van allen probes, *Journal of Geophysical Research: Space Physics*, *122*(10), 9858–9879, doi:10.1002/2017JA024487, 2017JA024487.

Xiang, Z., W. Tu, B. Ni, M. G. Henderson, and X. Cao (2018), A statistical survey of radiation belt dropouts observed by van allen probes, *Geophysical Research Letters*, doi:10.1029/2018gl078907.

Yu, Y., J. Koller, S. Zaharia, and V. Jordanova (2012), L* neural networks from different magnetic field models and their applicability, *Space Weather*, *10*(2), doi:10.1029/2011sw000743.

Appendix A

List of Events Selected for the Superposed Epoch Analysis

Table A.1 shows the list of events observed by the Van Allen Probes and which were selected for the superposed epoch analysis in the study presented in Chapter 5 of this thesis. We show the list in two columns with the total of 64 events selected by the algorithm, described in the main text. For each selected event we present the date in format YYYY-MM-DD, time in UT, and the minimal value of the LCDS in L*. Note that the dates and times, shown in the table, were treated as zero epoch for each storm in the superposed analysis. Additionally, relative to the epoch time zero, we use data from 72 hours before the given epoch and 72 hours past it for each event.

Table A.1: Zero epoch and the value of the minimum LCDS location during each storm, selected for the superposed epoch analysis.

#	Date	Time	LCDS
1	2012-09-03	12:25:00	5.375
2	2012-10-01	02:25:00	5.022
3	2012-10-13	09:00:00	5.309
4	2012-11-01	11:55:00	5.313
5	2013-01-17	18:20:00	5.322
6	2013-03-01	10:05:00	5.430
7	2013-03-17	10:00:00	4.906
8	2013-05-01	07:15:00	5.790
9	2013-05-18	02:45:00	5.794
10	2013-06-01	06:30:00	5.007
11	2013-06-07	02:40:00	5.624
12	2013-06-29	11:10:00	5.294
13	2013-07-06	06:30:00	5.541
14	2013-07-10	11:55:00	5.604
15	2013-07-14	15:10:00	5.558
16	2013-08-04	21:35:00	5.612
17	2013-10-02	05:00:00	4.696
18	2013-10-08	22:40:00	5.397
19	2013-12-08	03:30:00	5.108
20	2013-12-25	13:35:00	5.686
21	2014-02-27	21:25:00	5.096
22	2014-04-12	06:00:00	5.697
23	2014-04-30	12:15:00	5.660
24	2014-05-08	08:35:00	5.601
25	2014-06-08	05:50:00	5.223
26	2014-09-12	22:20:00	5.317
27	2014-12-22	04:30:00	5.351
28	2015-01-26	10:00:00	5.564
29	2015-02-02	02:30:00	5.397
30	2015-02-17	22:35:00	5.560
31	2015-03-17	15:05:00	4.319
32	2015-05-06	16:10:00	5.506

#	Date	Time	LCDS
33	2015-06-08	07:00:00	5.216
34	2015-07-04	21:20:00	5.341
35	2015-07-11	04:05:00	5.504
36	2015-07-23	07:40:00	5.760
37	2015-10-07	16:10:00	5.174
38	2015-10-18	09:15:00	5.762
39	2015-11-03	08:50:00	5.605
40	2015-11-07	07:20:00	5.369
41	2015-12-14	18:00:00	5.213
42	2015-12-20	08:10:00	4.717
43	2016-02-16	17:05:00	5.704
44	2016-03-06	19:20:00	5.017
45	2016-04-07	20:55:00	5.649
46	2016-04-13	00:35:00	5.640
47	2016-06-05	14:20:00	5.558
48	2016-07-20	04:45:00	5.368
49	2016-08-03	10:35:00	5.487
50	2016-08-23	20:30:00	5.634
51	2016-10-13	12:15:00	4.858
52	2016-10-25	12:50:00	5.690
53	2016-11-10	17:00:00	5.784
54	2017-03-01	12:20:00	5.748
55	2017-03-27	10:00:00	5.577
56	2017-04-04	07:10:00	5.734
57	2017-04-20	06:00:00	5.779
58	2017-05-20	09:20:00	5.698
59	2017-07-16	11:25:00	5.266
60	2017-08-04	10:30:00	5.755
61	2017-08-31	11:55:00	5.577
62	2017-09-28	07:45:00	5.729
63	2017-12-04	18:45:00	5.630
64	2018-03-10	04:20:00	5.761

Appendix B

Fits of the Median Superposed Epoch Flux During Magnetopause Shadowing Events

In this Appendix, we show details of the magnetic storm epoch dependence of the median normalized flux for different fixed L* and energy values from the Van Allen Probes and the storms listed in Appendix A. Figures B.1 through B.5 show superposed epoch dependencies for different energies, similar to the one shown in the bottom panel of Figure 5.5 and discussed in the main text. Note that each of the figures presented here corresponds to a single particular energy. Meanwhile, the L* value decreases from 5.58 to 3.59 in each of the panels. We also show the loss and recovery σ_1 and σ_2 fit parameters (see text for details). Note that the error bars represent the upper and lower quartiles for each data point.

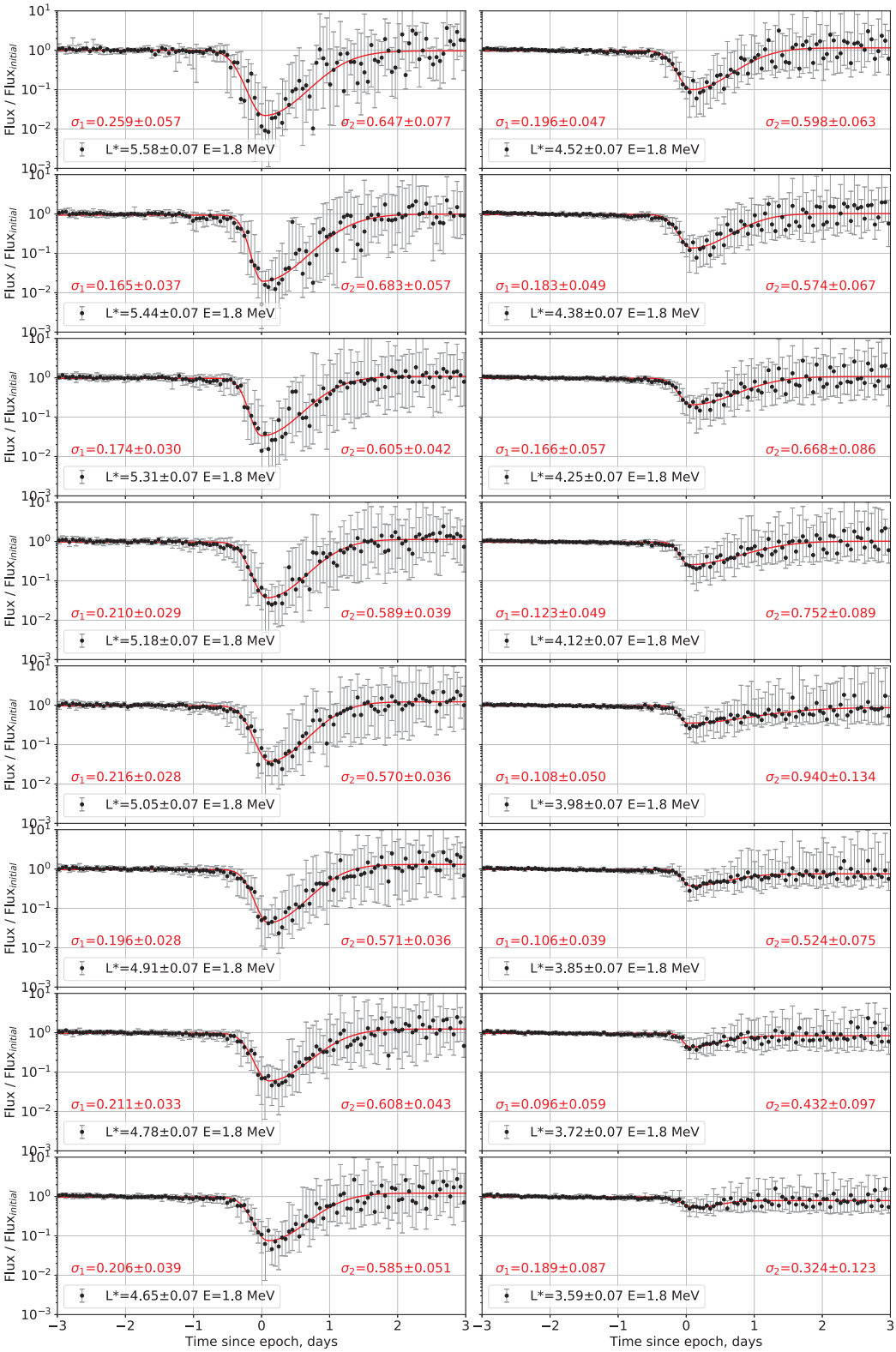

Figure B.1: The median normalized flux of 1.8 MeV electron population in different L* regions plotted with the fitted two-sided Gaussian function.

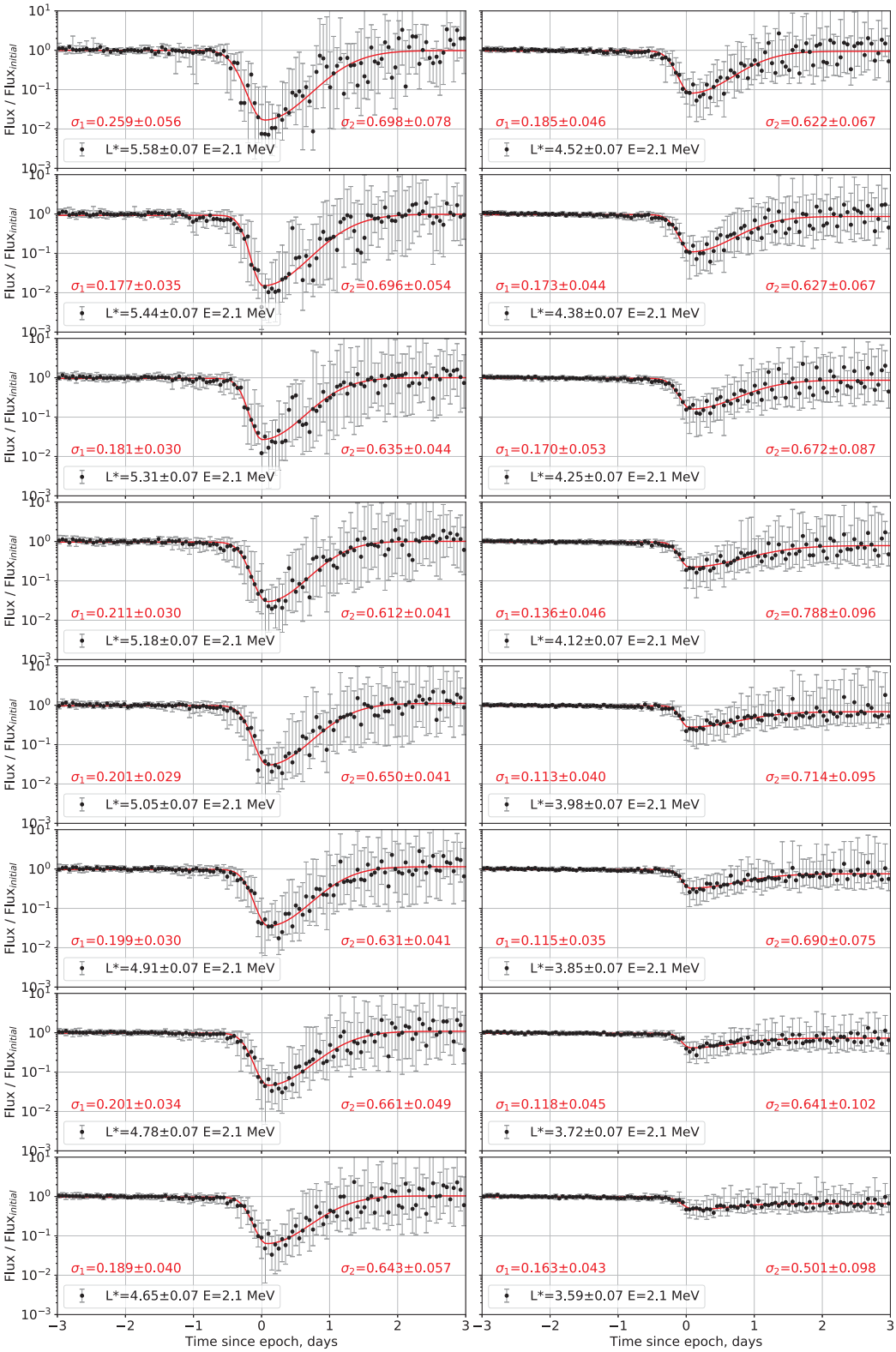

Figure B.2: The median normalized flux of 2.1 MeV electron population in different L* regions plotted with the fitted two-sided Gaussian function.

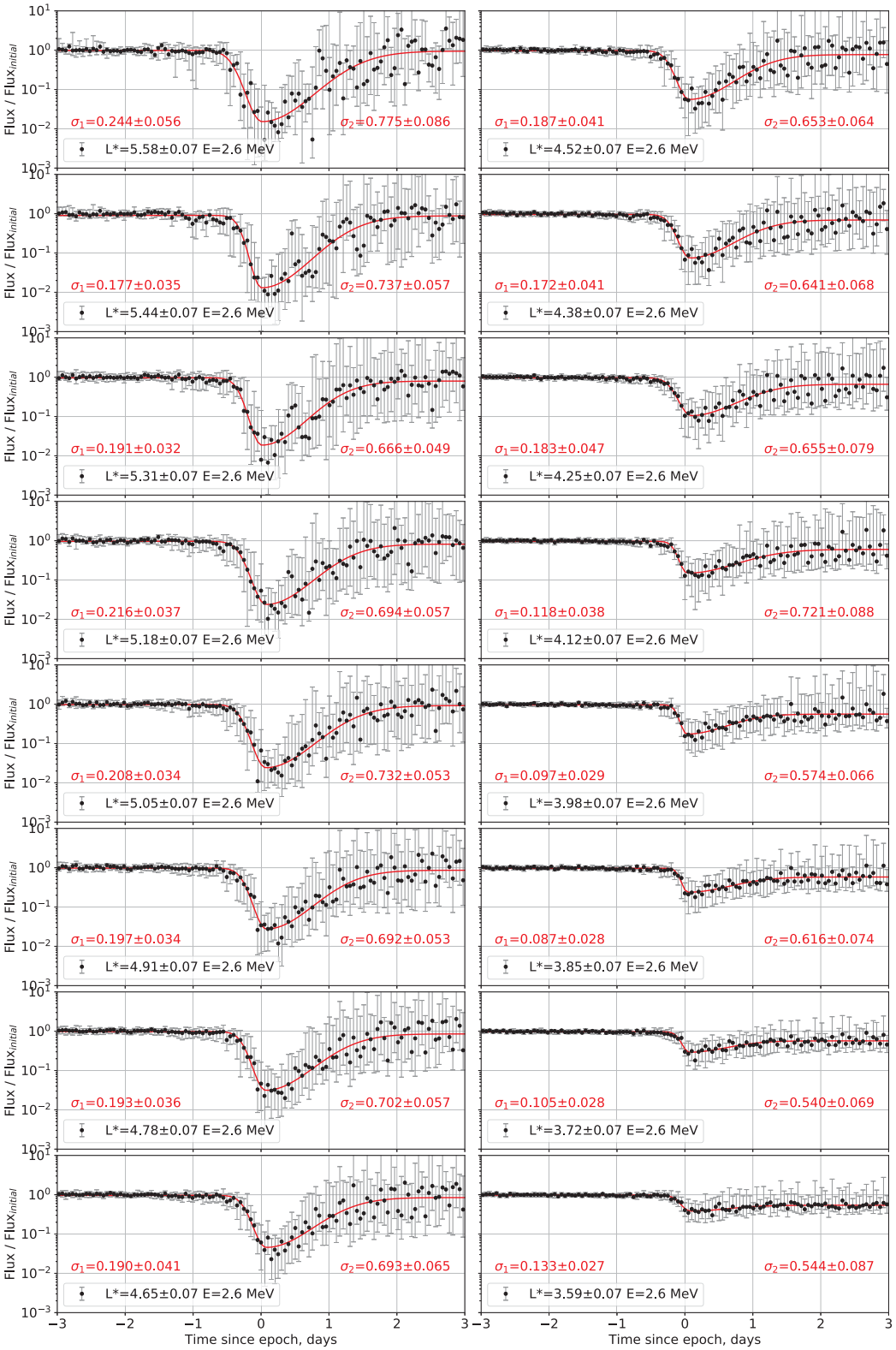

Figure B.3: The median normalized flux of 2.6 MeV electron population in different L* regions plotted with the fitted two-sided Gaussian function.

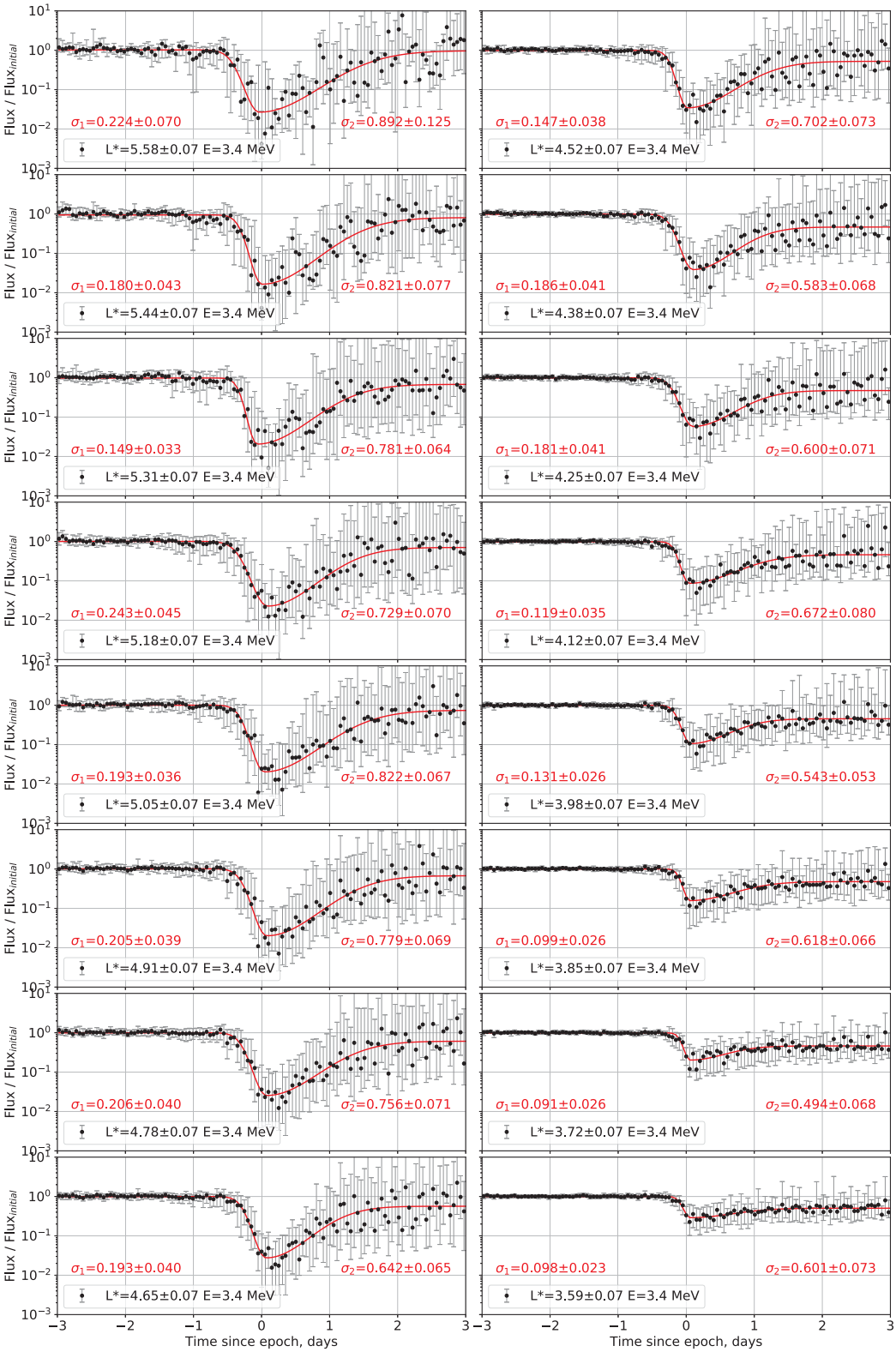

Figure B.4: The median normalized flux of 3.4 MeV electron population in different L* regions plotted with the fitted two-sided Gaussian function.

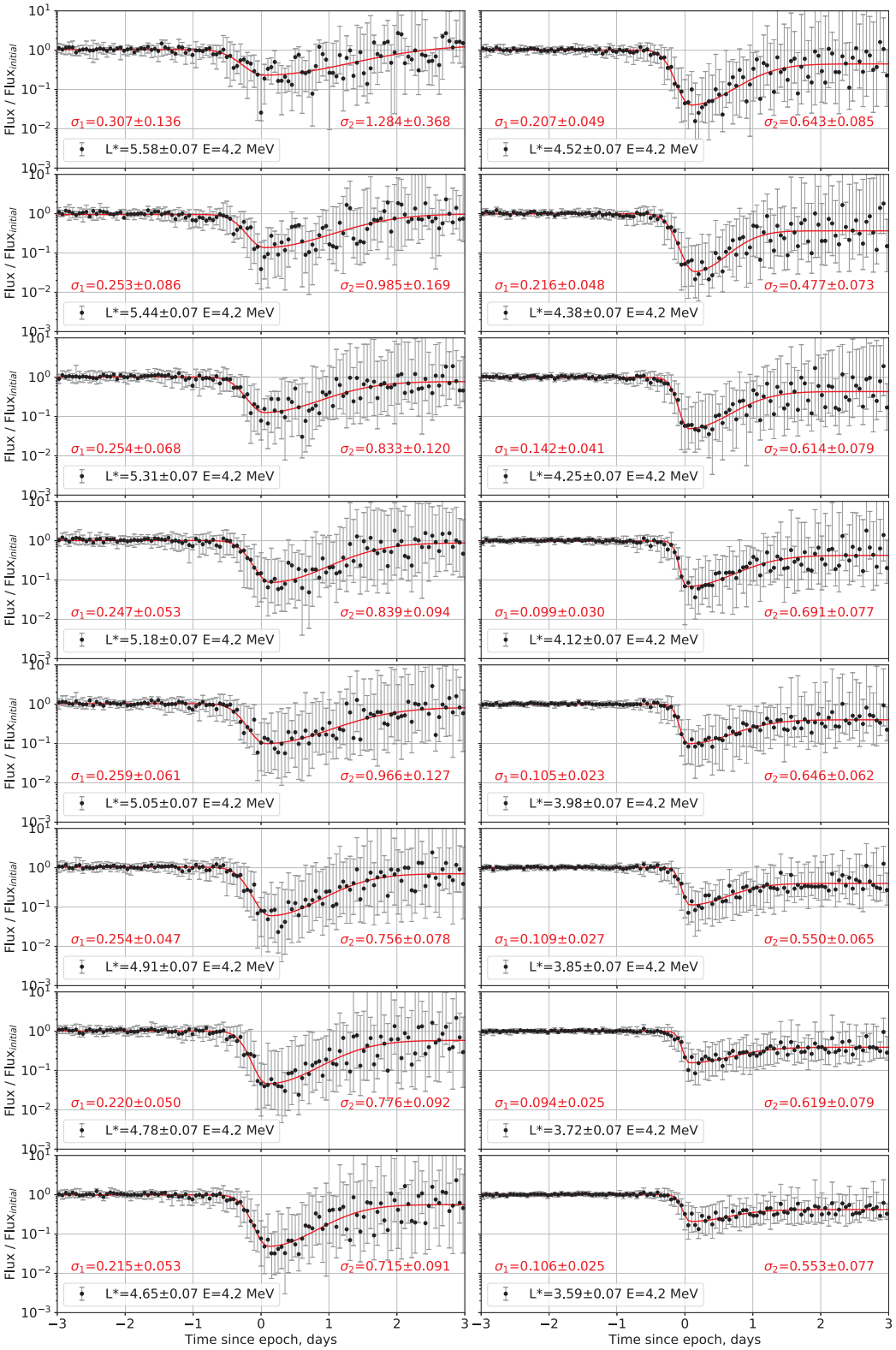

Figure B.5: The median normalized flux of 4.2 MeV electron population in different L* regions plotted with the fitted two-sided Gaussian function.

Appendix C

Fits of the Median Superposed Epoch Phase Space Density During Magnetopause Shadowing Events

In this Appendix, we show details of the magnetic storm epoch dependence of the median normalized phase space density for different L* and first adiabatic invariant, μ, values, obtained from the Van Allen Probes data, for the storms listed in the Appendix A. Figures C.1 through C.5 show superposed epoch dependencies for different first adiabatic invariants at constant L* and μ. Note that each of the figures presented here corresponds to a particular μ value ranging from 500 MeV/G to 2500 MeV/G. Meanwhile, the L* value decreases from 5.58 to 3.59 in the panels in each of the plots. We also show the loss and recovery σ_1 and σ_2 fit parameters (see Chapter 5 ext for details). Note that the error bars represent the upper and lower quartiles for each data point. Meanwhile, the data points without error bars has only a single entry and were not taken into account during fitting procedure.

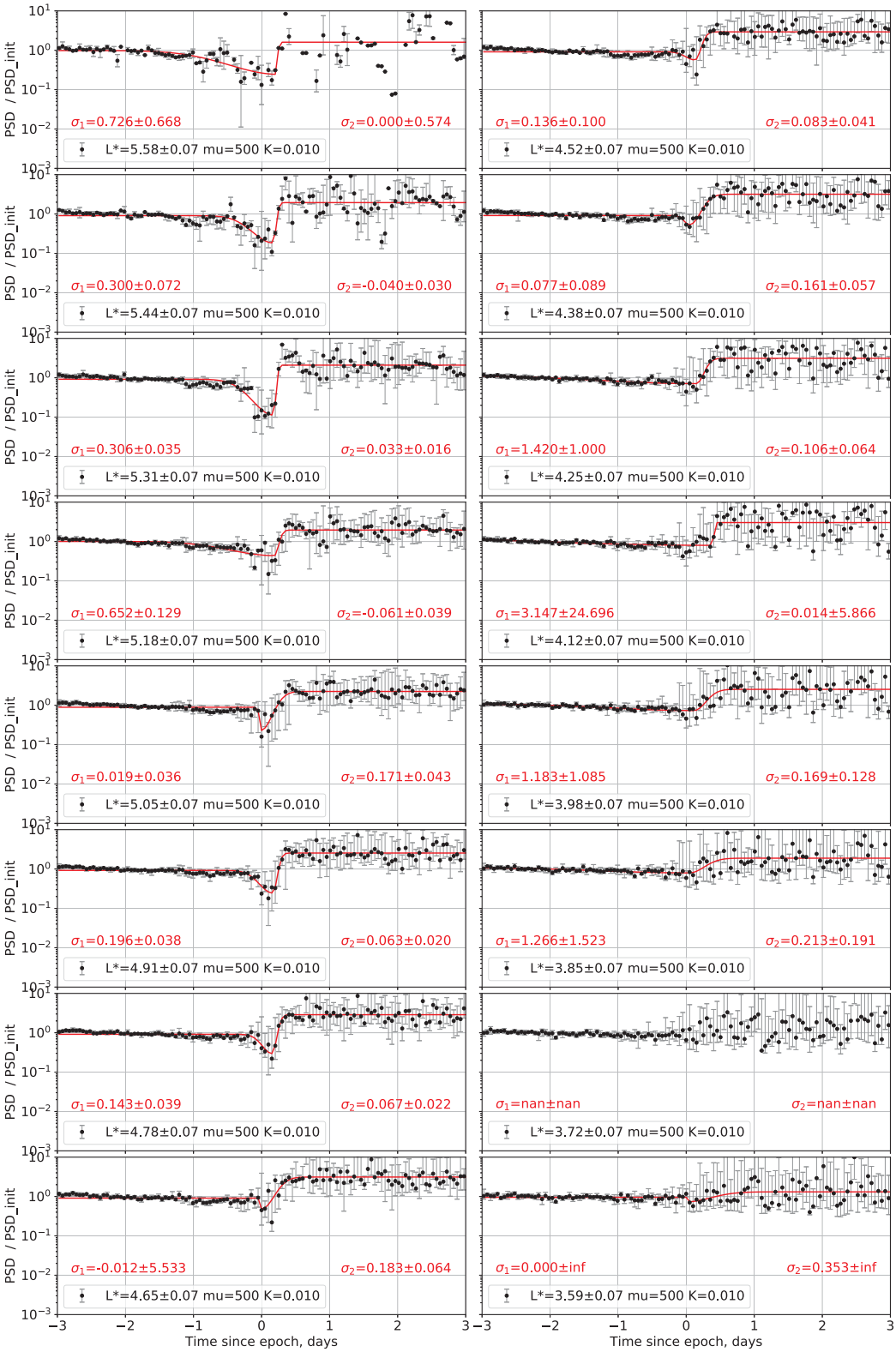

Figure C.1: The median normalized PSD for electrons with the first variant μ =500 MeV/G in different L* regions plotted with the fitted two-sided Gaussian function.

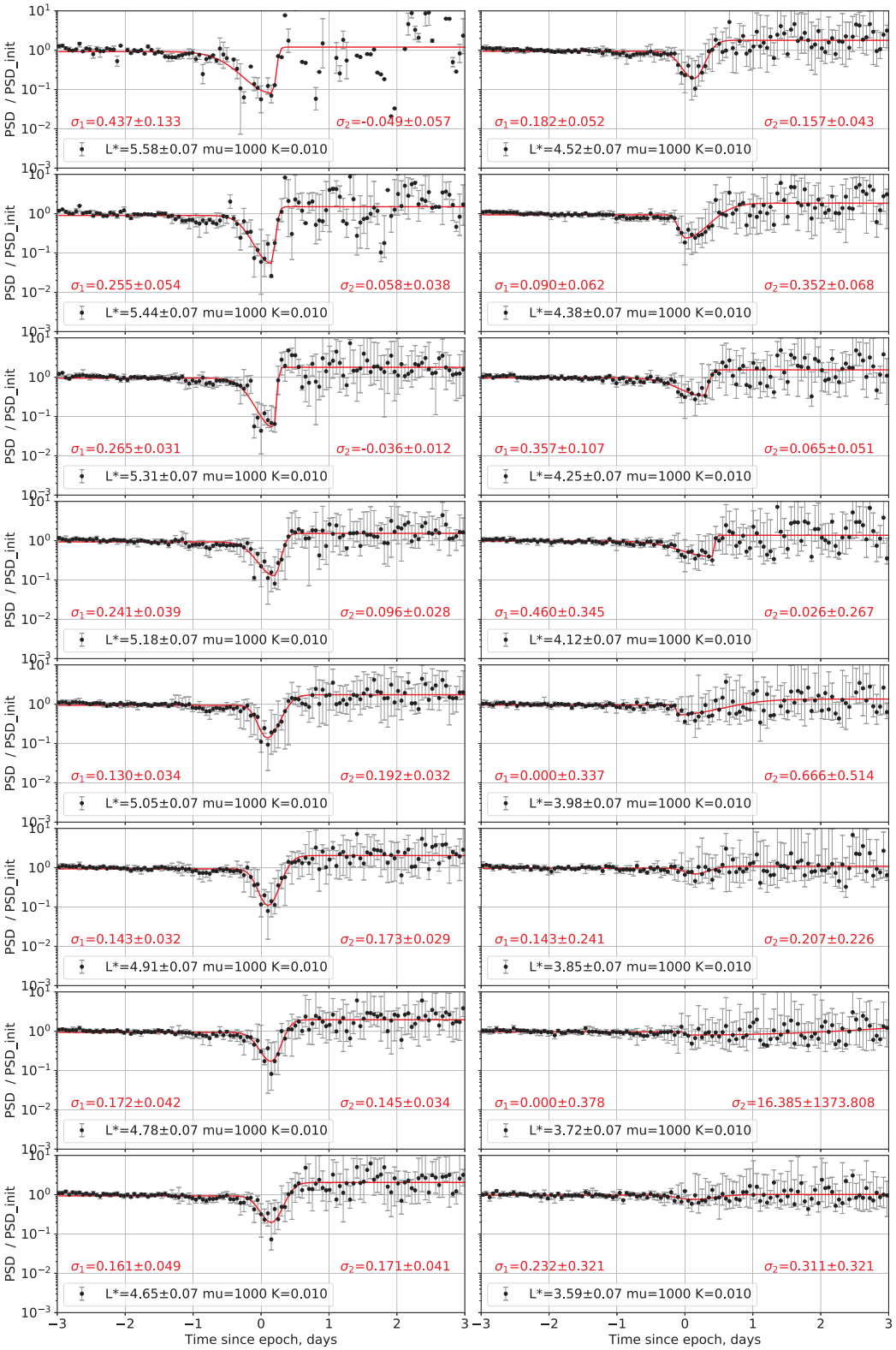

Figure C.2: The median normalized PSD for electrons with the first variant μ =1000 MeV/G in different L* regions plotted with the fitted two-sided Gaussian function.

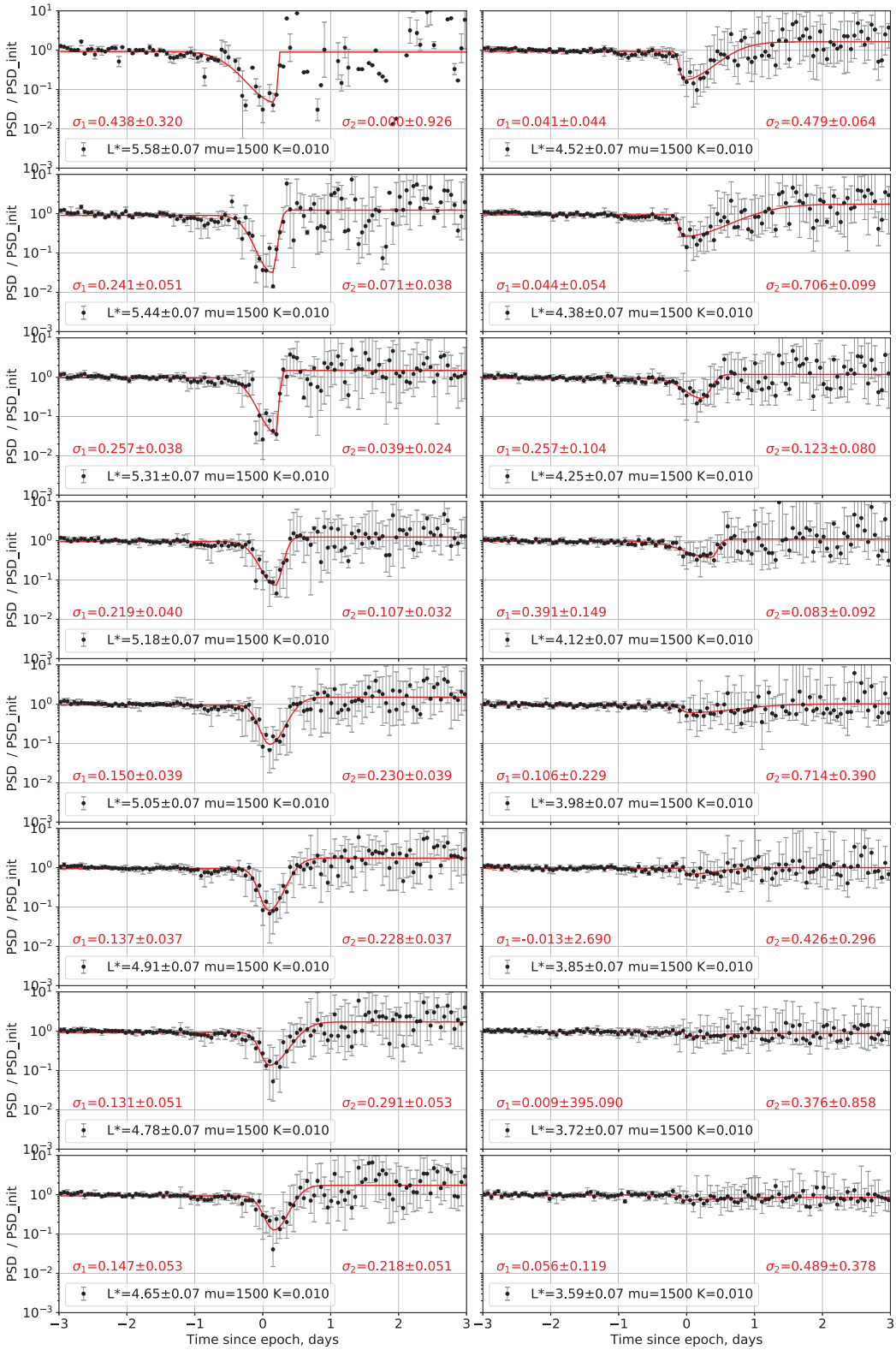

Figure C.3: The median normalized PSD for electrons with the first variant μ =1500 MeV/G in different L* regions plotted with the fitted two-sided Gaussian function.

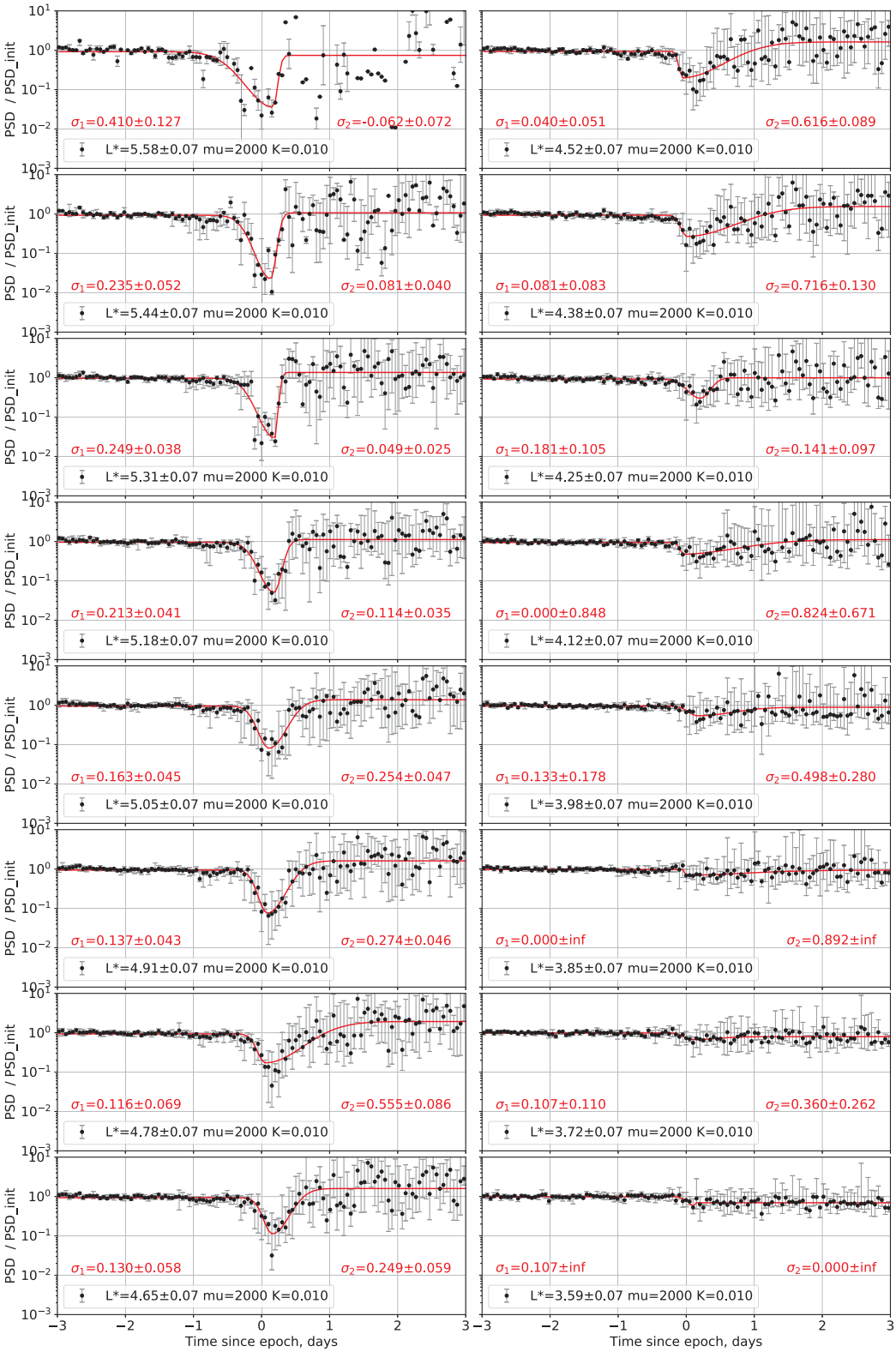

Figure C.4: The median normalized PSD for electrons with the first variant μ =2000 MeV/G in different L* regions plotted with the fitted two-sided Gaussian function.

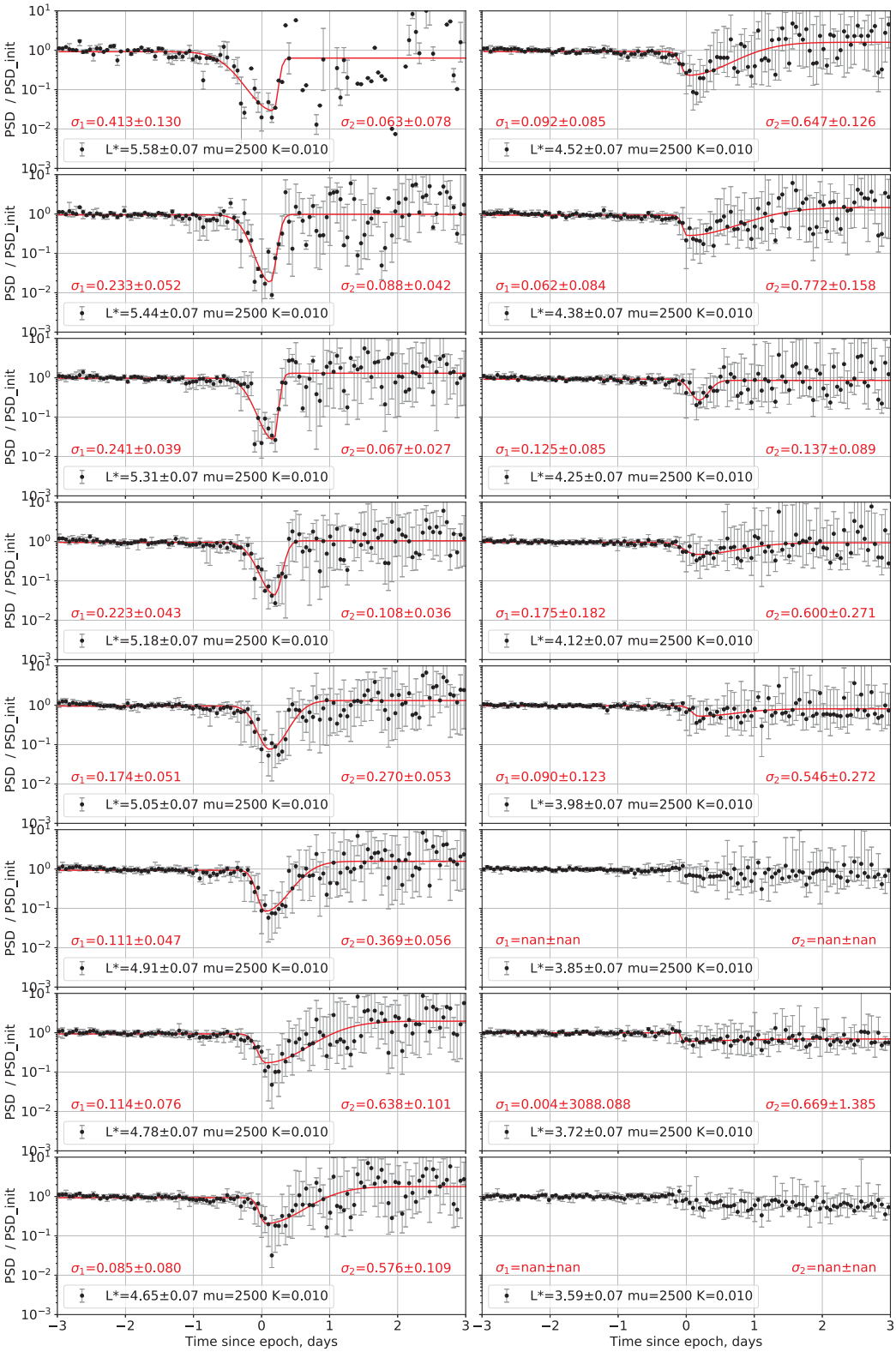

Figure C.5: The median normalized PSD for electrons with the first variant μ =2500 MeV/G in different L* regions plotted with the fitted two-sided Gaussian function.